Electrochemical Reductive Stability of Self-Assembled Monolayers on Transition Metal Electrodes

by

Robert Edward Bonsall

A dissertation submitted in partial fulfillment
of the requirements for the degree of
Doctor of Philosophy
(Chemistry)
in the University of Michigan
2022

Doctoral Committee:

Assistant Professor Charles McCrory, Chair
Professor Zhan Chen
Professor Stephen Maldonaldo
Professor Johannes Schwank

Robert Edward Bonsall

rebonsa@umich.edu

ORCID iD: 0000-0002-8145-8317

Dedication

This work is dedicated to anyone who works with challenging, messy data. My hats off to you, and keep pushing through.

Acknowledgements

Nothing would be possible without Mom, so first the first thank you goes to her. Second one goes to friends back home in PA and SF who have always been family to me, our summer skate trips up the coast, to Texas or anywhere, has kept me sane, I love you guys. I would like to thank my advisor, Charles McCrory, for giving me the opportunity to work in his lab, and for teaching me the fundamentals of electrochemistry and scientific presentation. I want to thank Grace Clinger for her hard work and collaboration in collecting the time dependent voltametric data presented in this thesis. Thank you goes to Lirong Shi, who is taking over my project, and spear-headed the cell assembly for the latest beamline experiments. Thank you to Professor Jim Penner-Hahn and Dr Aniruddha Deb, for facilitating and guiding the beamline experiments and the data analysis. Thank you goes to Ryan Davis and Sarah Edwards at SSRL for their expertise in grazing-angle XAS and designing the electrochemical beamline cell, and providing us with material lists and access to the CAD files. I want to thank Pilar Herrera-Fierro, for spending so many hours with me in training on the lapper at LNF, and for her humor and energy. Thank you to the tool operators at LNF, Matt Oonk on the evaporator, and Jorge Barreda who was very thorough and supernaturally patient with his training on the dicing saw. Thank you goes to McCrory lab members: Kwan Leung for teaching me how to construct a reference electrode and for her moral support and most importantly, getting me a job(!), Jeremy Kallick for teaching me synthetic chemistry techniques and general know-how in the lab, William Dean for collecting PM-IRRAS data of my samples. Also, Taylor, Sam, Yingshuo, and Weixuan, thanks for your

friendship and support over the years in the McCrory lab. It’s been quite a ride that I will never forget.

Table of Contents

List of Figures

Abstract

Alkanethiol based self-assembled monolayers (SAMs) on Au surfaces are an attractive platform for studying tethered reductive electrocatalysts, but the reductive potential stability window of SAMs prohibits their usefulness in studying CO_2 and NO_3^- electrocatalysts which activate at low potentials where the Au-S bond is cleaved via a one-electron reduction. Previous work suggests that SAMs formed on other metals such as Cu and Ni may be reductively stable for tethering low potential electrocatalysts, but the methods used to assess the stability window are indirect and qualitative. In this work, the use of ferrocene-capped (Fc) SAMs as a quantitative redox probe is explored in the classic Au-SAM system to inform the usefulness of a tethered redox probe for coverage measurements as a function of potential on other metals to establish their stability limits. The voltammograms of the Fc-SAMs after the application of reductive potentials used for quantitative analysis were found to be challenging due to their non-ideal baselines which effect peak area measurements. The bias of traditional baselining techniques was explored, and new methods using empirical baselines in conjunction with machine learning provided useful estimates of the SAM coverage after the application of destabilizing reductive potentials, which were compared with secondary measurements using ICP-MS. After establishing the bias from baselining, the effect of electrolyte composition and holding time at a given potential were explored to explain the differences observed in the stability window measure by traditional reductive desorption cyclic voltammetry, and the potential dependent coverage measurements using Fc-SAMs. Looking towards direct measurement of SAMs on other metals, the d-band model is proposed for predicting and

explaining the reductive stability on other metals. The first results from *operando* probing of the Au-S bond using x-ray absorbance spectroscopy are presented, paving the way forward for direct measurement of metal-SAM surface interactions as function of potential.

.

Chapter 1 Introduction: Self-Assembled Monolayers as a Platform for Tethering Molecular Electrocatalysts, The Problem of Reductive Stability, and Measurement

1.1 Self-Assembled Monolayers as a Platform for Tethering Molecular Electrocatalysts

Self-assembled monolayers (SAMs) are molecules that spontaneously attach and arrange themselves in a single layer on a surface when exposing the surface to molecules in the gas or liquid phase.[1] The premier model SAM system is composed of alkanethiols on Au surfaces. Alkanethiols SAMs have well-defined long-range order, and a tilt angle (~ 30°) relative to the surface normal, which make them attractive to electrochemists for investigating electron transfer kinetics of tethered molecular electrocatalysts.[2] Tethering molecular electrocatalysts to electrode surfaces simplifies the study of the catalytic intrinsic activity by eliminating the convoluting effects of catalyst diffusion into and out of the reaction layer near the electrode surface.[3] The "well-packed" quality of alkanethiol SAMs on Au block undesired surface side-reactions, while also tethering molecular electrocatalysts for *selective* product formation at the terminus of the SAM.[4,5] For studying rate dependent catalytic pathways, changing the length of the tether modulates the rate of electron transfer from the electrode surface to the tethered electrocatalyst.[5] The optical properties of SAMs on metal surfaces with low carbon backgrounds permit *operando* infra-red (IR) and Raman spectroscopic measurements of the surface during electrocatalysis, which are useful for directly identifying potential-dependent intermediates in electrocatalytic cycles.[6] To take advantage of all of these properties, first the SAM must be functionalized with

the electroactive catalyst, and this functionalization can affect the packing and stability of the SAM.[2]

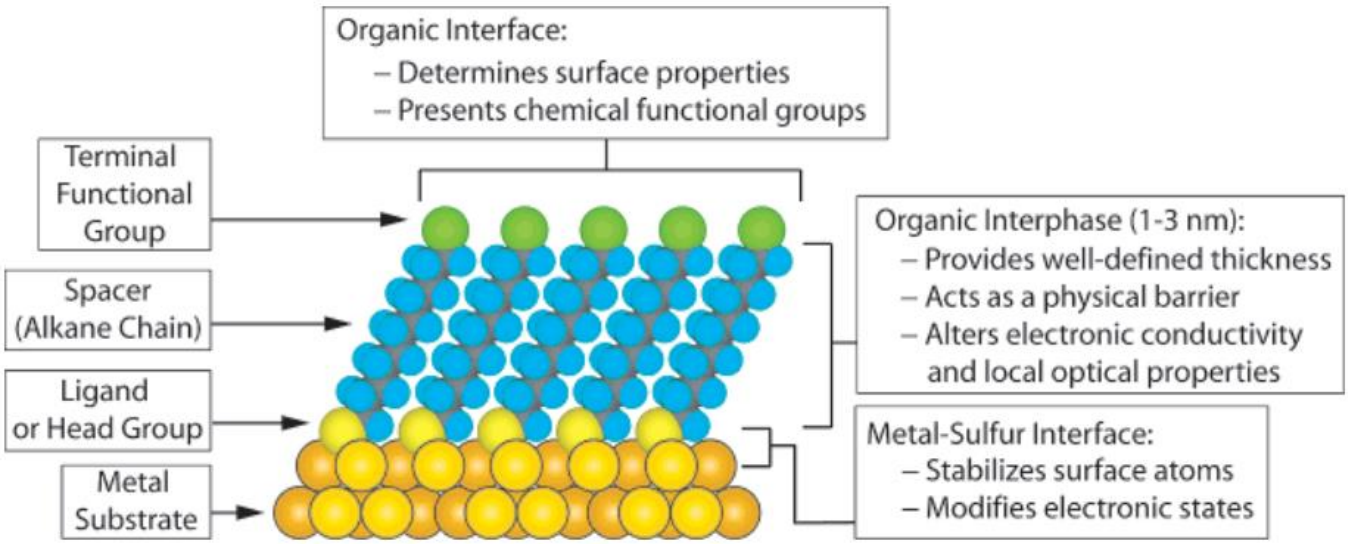

Figure 1-1 Picture of idealized SAM on Au. Reprinted (adapted) with permission from Chem. Rev. 2005, 105, 4, 1103–1170. American Chemical Society.

To understand the conditions which create SAMs with the desirable properties mentioned above, it is useful to consider the forces that drive the self-assembly process. Alkanethiol SAMs on Au assemble spontaneously when exposing a gold surface to millimolar concentrations of the thiol dissolved in ethanol.[1] A common hypothesis (equation 1.1) describes the formation of a covalent bond formed between the sulfur atom and the gold surface, although this description remains controversial and is explored in more detail in Chapter 4.[1,7,8]

$$(1.1) \quad \text{R-S-H} + \text{Au} \rightleftharpoons \text{R-S-Au} + \tfrac{1}{2}\,\text{H}_2$$

The thiol-surface interactions form within milliseconds creating low density surface coverage, but slowly reorganize over time (24 hours) to form the high-density "well-packed" monolayers with a coverage of $\sim 7.7\times10^{-10}$ moles cm^{-2}.[1] The reorganization to higher density surfaces is correlated to longer alkyl chains of the thiols and increased electrochemical stability, promoted by Van der Waals interactions between the hydrophobic chains of nearest-neighbors on the surface.[1] Figure 1-1 idealizes the physical structure of a pristine alkanethiol SAM on Au.

Functionalizing the terminus of the SAM is the preferred method for attaching molecular electrocatalysts to avoid disrupting the stabilizing Van der Waals interactions.[2] For the synthesis of functionalized SAMs there are two general strategies; (1) synthesizing the thiol with the functional group before deposition, and (2) attaching the functional group to the thiol via a surface reaction after the thiol has been deposited on the surface. In the first strategy, redox-active groups are attached covalently via carbon-carbon bonds, amide or ester coupling, and then deposited on the surface.[2] Due to steric hindrance of the redox-active groups, functionalized SAMs require longer deposition times for reorganization to minimize the number of defect sites.[2] Co-deposition with a diluent alkanethiol reduces defects by acting as a spacer between bulky

groups, although at the expense of coverage. The optimized diluent ratio is dependent on the relative adsorption kinetics of the functionalized thiol and the diluent thiol, which makes controlling the surface ratio difficult in some cases.[9] Alternatively, using the second strategy, SAMs can be functionalized post-deposition. Chidsey devised a post-deposition modification scheme for electroactive SAMs by depositing azide-terminated alkanethiols with a diluent alkanethiol in one step, and then reacting the terminal SAM azides with alkyne groups attached to molecules containing the desired redox-active moiety, using copper catalyzed Huisgen 1,3-dipolar cycloadditions ("click" chemistry) to form a triazole linkage between the terminus of the SAM and the redox moiety as shown in figure 1-2 with propynone ferrocene.[5,10] When using the post-deposition "clicked" method to functionalize SAMs, well-packed SAMs are formed *before* functionalization and the relative ratio of azido-thiol to the diluent-thiol on the surface can be mapped from the deposition solution and reproducibly controlled independent of the functional group which is added later. This strategy lowers the number of experimental parameters to be tuned in the optimization of the SAM structure and coverage.[11]

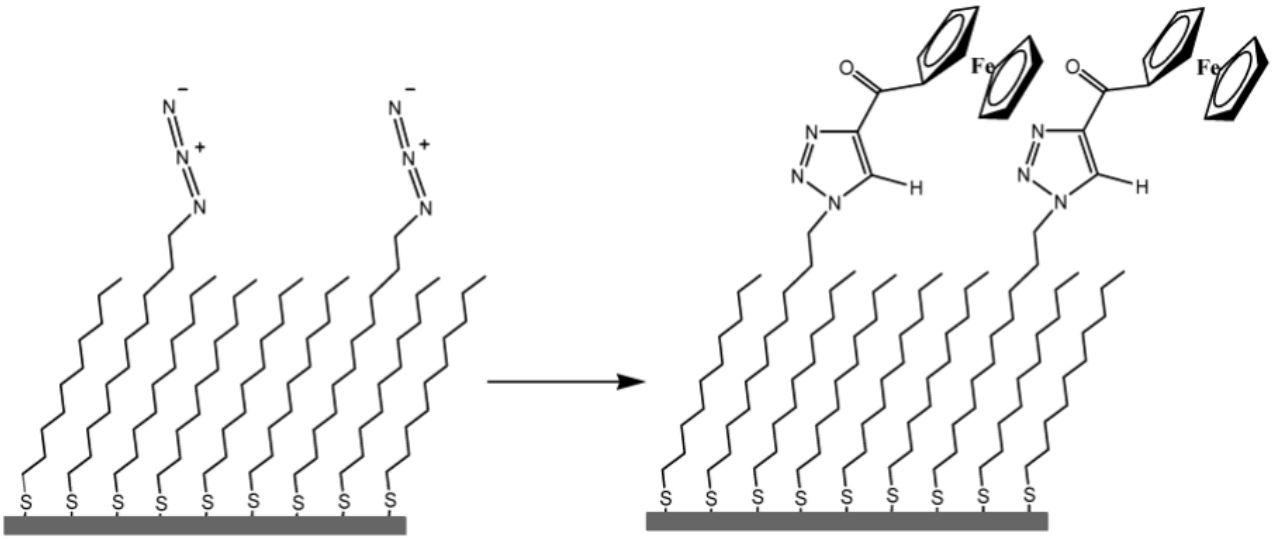

Figure 1-2 Example of post-deposition modification of a SAM with ferrocene propynone. Mixed SAMs composed of 1-azidoundecanethiol with a decanethiol diluent were transformed into ferrocene-terminated SAMs via Cu(I)-catalyzed "click" chemistry. Reprinted (adapted) with permission from Langmuir 2004, 20, 4, 1051–1053. American Chemical Society.

Using the “click” scheme above to immobilize molecular electrocatalysts would permit mechanistic studies of CO_2 and NO_3^- electrochemical reduction reactions.[12] For example, molecular Co- and Ni(cyclam) complexes are electrocatalytically active for CO_2 and NO_3^- reduction in neutral to high pH aqueous solutions at potentials of ~ -1.4 V vs AgCl, but a detailed investigation of the catalytic mechanism is lacking in the literature.[12-14] Using surface sensitive IR spectroscopy and immobilization would confirm proposed catalytic intermediates such as CO coordination to catalyst metal centers.[15] A generalized scheme for the immobilization of metal-cyclams using SAMs is shown in figure 1-3, with mono N-alkylation of cyclam with propargyl-bromide and the Cu(I)-catalyzed Azide-Alkyne Cycloaddition.[12,16]

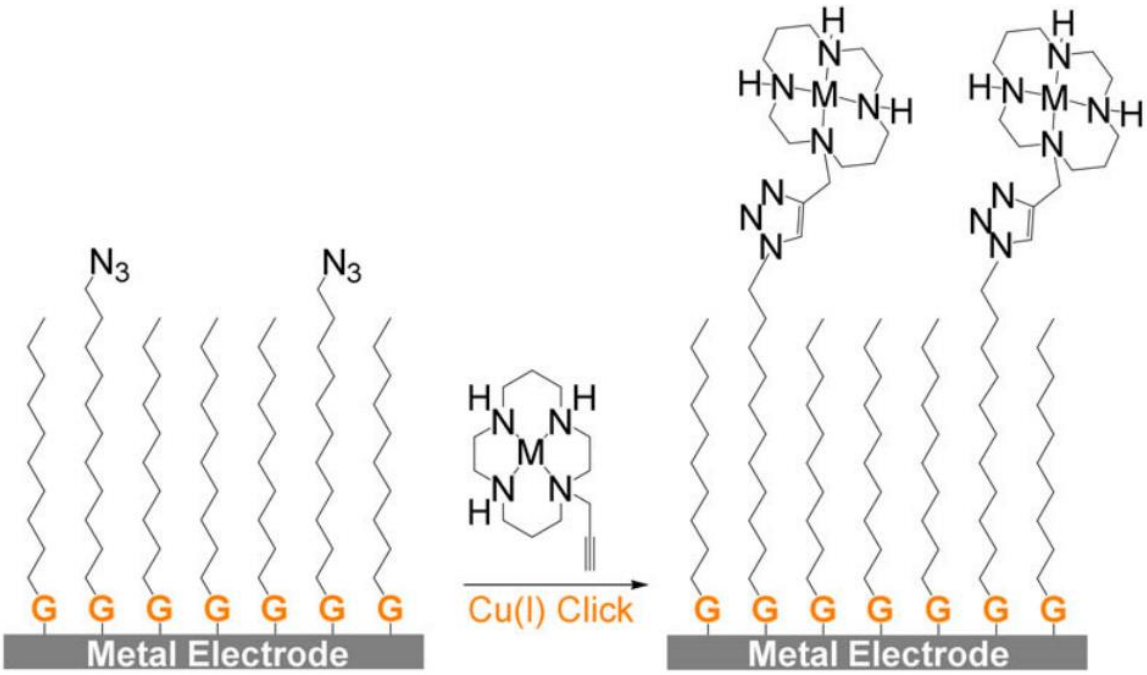

Figure 1-3 "Proposed attachment of ethynyl-terminated metal cyclams to self-assembled azide-terminated mixed monolayer on metal electrode surfaces." – Figure credit Charles McCrory.

While alkanethiol SAMs on Au can deliver a tunable experimental platform for studying immobilized molecular electrocatalysts, a major limitation for using them is the potential range at which the SAMs are reductively stable. Alkanethiol SAMs on Au are reductively cleaved from the surface at ~ -1 V vs AgCl, 400 mV positive of the onset potential of electrocatalysis when using the metal cyclams and most CO_2 reduction electrocatalysts. Reductively cleaving the thiol-tether from the surface would result in the loss of the desired structural properties of the SAM, and the catalyst would diffuse away from the electrode surface to the bulk electrolyte where it is electrocatalytically inactive. The problem of SAM reductive stability is described in more detail in the next section (1.2).

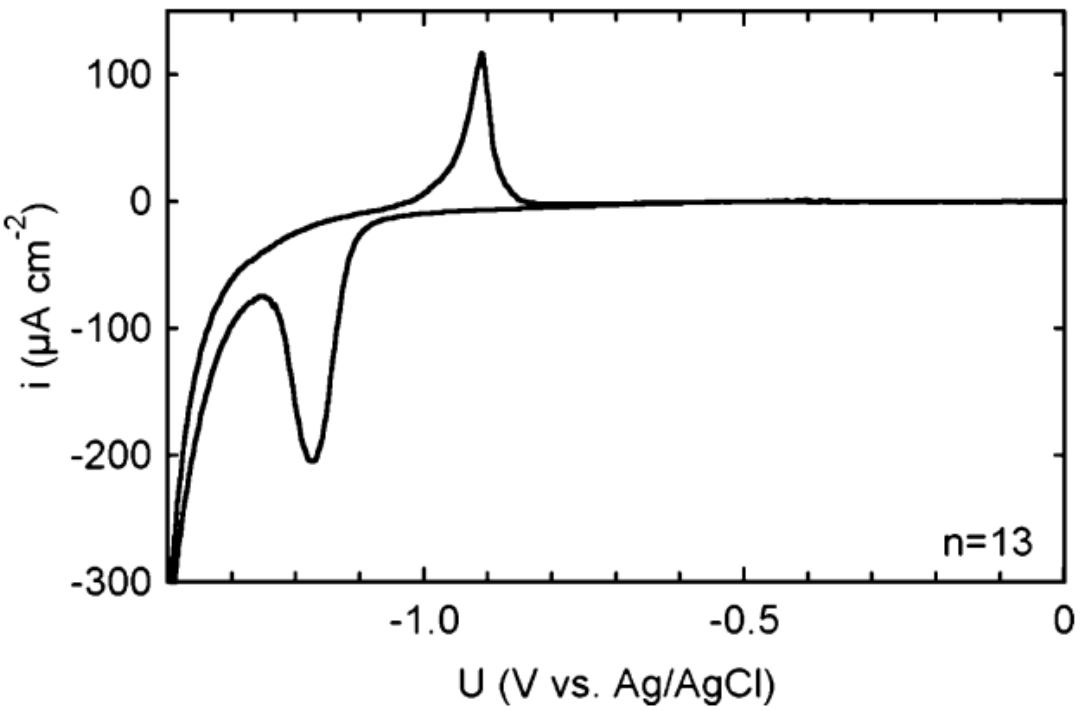

Figure 1-4 CV of the reductive desorption of a tetradecane-thiol SAM from a polycrystalline Au surface in KOH. Figure is from reference 19. Scan rate is 100 mV/s. Reprinted (adapted) with permission from Langmuir 2006, 22, 8, 3474–3476 American Chemical Society

1.2 The Problem of Reductive Stability

Alkanethiol SAMs on Au are not reductively stable at the potentials required to drive CO_2 and NO_3^- reduction electrocatalysts which operate at potentials negative of ~ -1.4 V vs AgCl precluding their use as a surface tethering strategy. Alkanethiol SAMs are postulated to reductively desorb from Au surfaces at ~ -1V vs AgCl via the one-electron mechanism shown in equation 1.2.[17,18]

$$(1.2) \quad \text{Au-S-R} + e^- \rightleftharpoons \text{Au} + {}^-\text{S-R}$$

Cyclic voltammetry is the primary means of observing reaction 1.2, shown in figure 1-4, where the potential is scanned from a potential where the SAM is electrochemically stable towards negative potentials until a cathodic peak (or peaks) in the current is observed from pumping an electron into the sulfur group of the SAM, cleaving the Au-S bond , and then the scan is reversed to scan towards positive potentials where an anodic peak for the oxidative reabsorption of the thiol can be observed, although observation of an anodic oxidation peak is not always observed due to a myriad of factors which are debated in the literature.[19] A number of structural and experimental factors shift the SAM desorption peak potential (E_P) , including the length of the SAM[20,21], the functionalization of the SAM[22,23], the ratio of diluent in mixed-SAM deposition[24], the deposition time[17], identity of the metal electrode[20], structure of the metal surface[25], electrolyte pH[26], electrolyte cation size[20], the polarity of the electrolyte[21], and the scan rate[17], to name a few. Of these factors, considerable weight is given to the structure and packing of the SAMs. In figure 1-5 from Porter, the desorption peak potential (E_P) shifts negatively 20 mV per n carbon unit (note that figure 1-5 plots the negative of E_P which makes the slope positive) with a linear dependence on the length of the alkyl chain length, which correlates with hydrophobic

force measurements.[27] From a thermodynamic free energy ($\Delta G = -nF\Delta E$)[28] point of view, a more negative E_P means the energy of the reducing electron in the electrode surface must be raised (more negative potential) in order to overcome the increase in the free energy for processes concomitant with reductive desorption, such as cation charge pairing, solvating hydrophobic alkanethiols with water, and the energy cost of disrupting the Van der Waals forces between nearest-neighbors.[18,29,30] Another important factor to note in figure 1-5 is the much larger shift in E_P of -200mV for SAMs on Ag compared to Au. The desorption potentials for the Ag data are limited to $n < 7$ by the onset of larger HER currents which obfuscate the desorption peak current. HER can be seen in figure 1-4 as a large increase in negative current at -1.3 V, which is the limit for observing SAM desorption peaks on Ag in figure 1-5. The potential shift towards more negative E_P from changing the metal from Ag to Au (-200 mV) is much greater than the shift from increasing the length of the alkyl chain per carbon unit (20 mV/n), which suggests a targeted strategy for increasing the reductive stability of SAMs should investigate the effect of the metal surface. One could argue that extending the alkyl chain length to $n>25$, based on the 20 mV/n slope of figure 1-5, could push the E_P beyond the threshold potential for activating a tethered metal-cyclam at ~ -1.5 V vs AgCl, but this would come at the cost of greatly attenuating the electron transfer rates. Longer alkane chains exponentially attenuate the electron transfer rates, making them unpractical for observing reasonable electrocatalytic turnovers.[31]

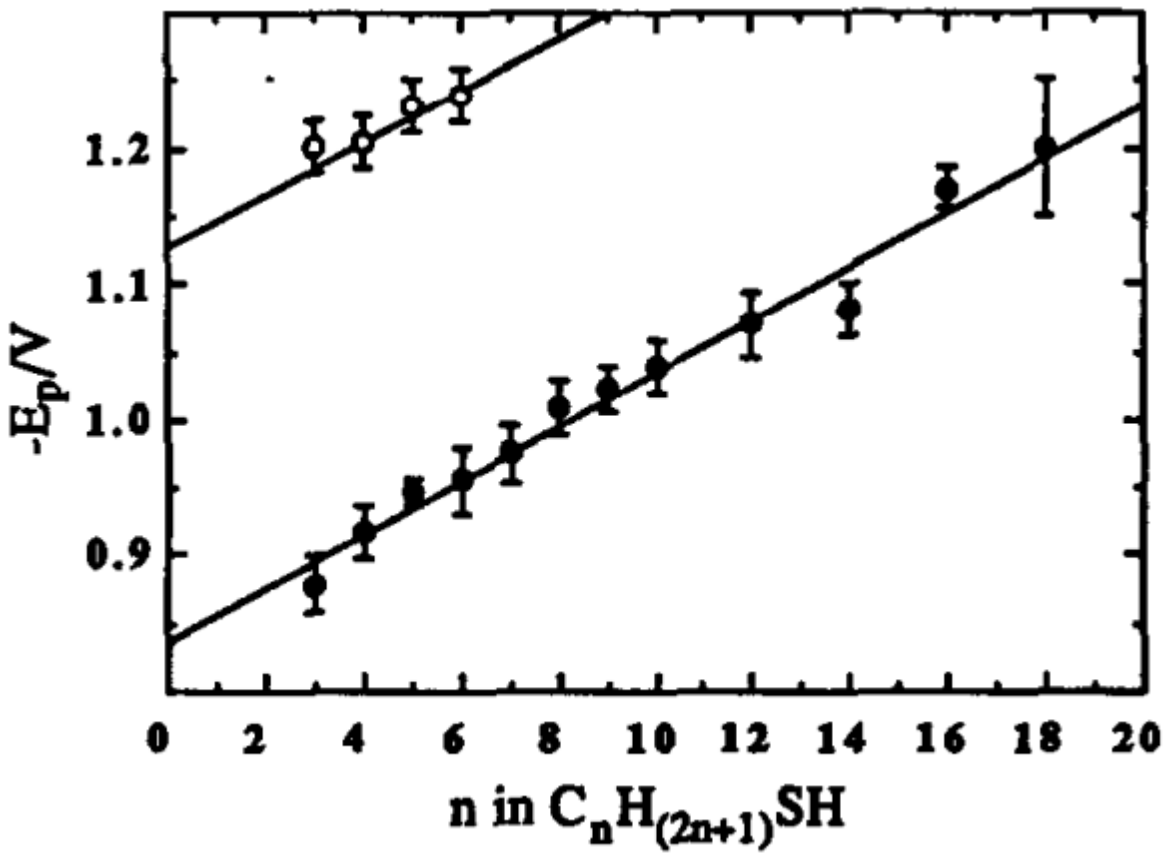

Figure 1-5 Alkanethiol SAM peak desorption potentials, E_P, vs n number of carbons in alkyl chain for Au (closed circles) and Ag (open circles). CVs taken at 100 mV/s in 0.5 M KOH. Potentials reported vs AgCl. From reference 20. Reprinted (adapted) with permission from J. Electroanal. Chem., 310 (1991) 335-359. Elsevier.

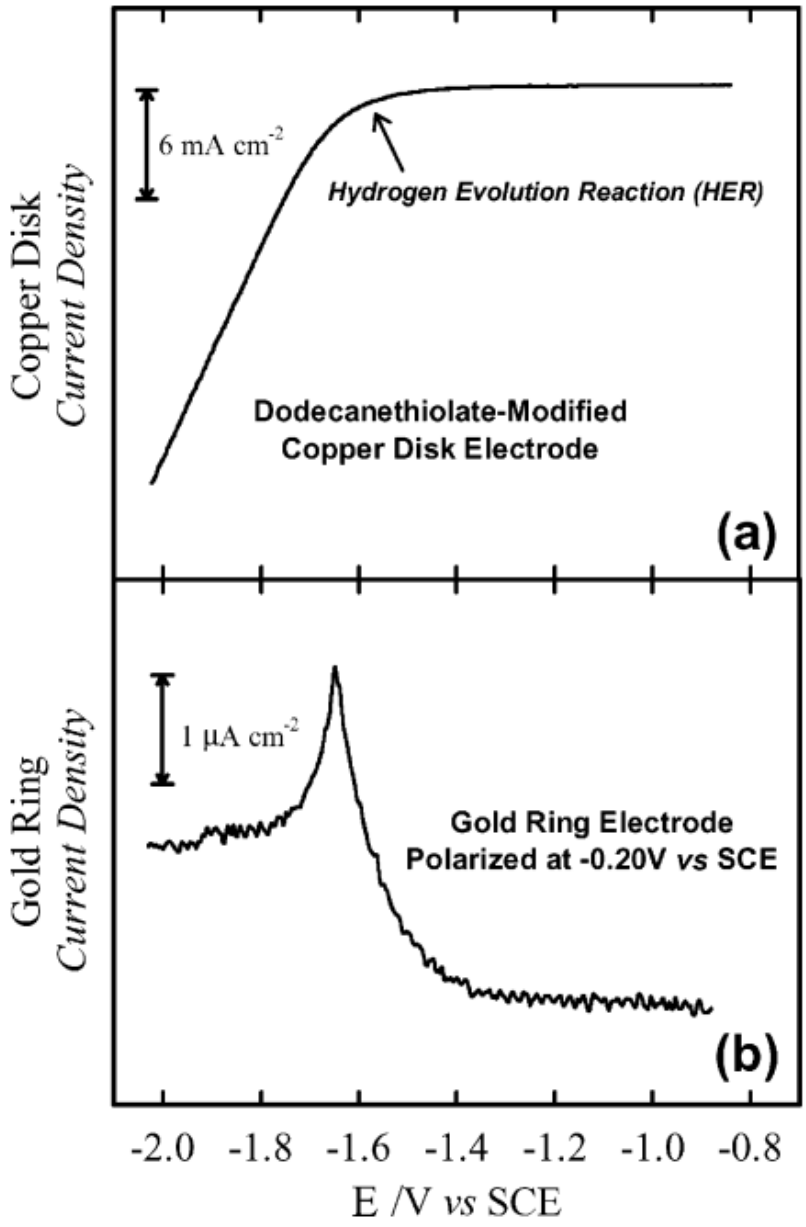

Figure 1-6 (a) CV of dodecanethiolate SAM on Cu disk electrode. (b) Anodic current collected at Au ring disk concentric with the Cu-SAM electrode. The scan rate was 0.05 V/s, and the electrolyte 0.1 M NaOH in 5% H_2O methanolic water. Reprinted (adapted) with permission from J. Phys. Chem. B 2003, 107, 13446-13454 American Chemical Society.

Overall, the Ag-SAM and Au-SAM desorption data imply two key takeaways for describing SAM reductive stability; (1) structure and packing influences reductive stability, but (2) the choice of the metal, or the metal-headgroup (sulfur) interactions, may have a much larger impact on the reductive stability of SAMs on metal surfaces. To investigate this idea further, the reductive stability CVs of SAMs deposited on Cu surfaces was explored in the work by Azzaroni, figure 1-6 (a), which shows the CV of a dodecanethiol SAM where no reductive desorption peak is observed before the onset of HER, suggesting the SAM is reductively stable up to at least -1.6 V vs SCE.[32] The absence of a desorption peak coupled with sulfur Auger electron spectroscopy suggested that the Cu-SAM was reductively stable until at least -1.7 V vs SCE (SCE is ~ +0.044 V relative to AgCl) coinciding with the onset of the large HER current. In 1-6 (b), the currents of a Au ring during the desorption experiment was set to oxidatively "catch" the desorbed thiolates released from the Cu surface during reductive desorption at -1.7 V, giving rise to an anodic adsorption peak, as the ring was held at a constant positive potential (-0.2 V vs SCE) where thiolates can oxidatively re-adsorb on Au. The ordering of SAM reductive stability on Au and Ag reported by Porter in aqueous electrolyte (figure 1-5) was replicated in the study by Azzaroni using the Au ring method in figure 1-6, but with methanolic electrolyte.[32] Figure 1-7 shows the same general trend, Ag-SAMs are more reductively stable than Au-SAMs by ~ 200 mV, but with new data that suggests that Cu-SAMs are more reductively stable than Au-SAMs by ~ 700 mV, putting the stability of the SAMs within range of the activation potential of the metal cyclam CO_2 and NO_3^- reduction electrocatalysts.

While the literature data presented above is encouraging for the prospects of developing more reductively stable SAMs on metal surfaces for tethering CO_2 and NO_3^- reduction electrocatalysts, the measurements are indirect. The Au ring peaks indicate an oxidative current

which can be correlated with desorption peaks on Au and Ag, they do not directly measure changes in the SAM surface coverage. Finding a way to measure the SAM surface coverage quantitatively would help confirm the results presented in figure 1-6 and 1-7 and this is addressed in the next section 1.3, and in Chapters 2 and 3. Furthermore, the much larger question of why SAM reductive stability is tied to the identity of the metal surface remains. Are there any guiding principles which could predict trends in stability? This question is explored further in Chapter 4.

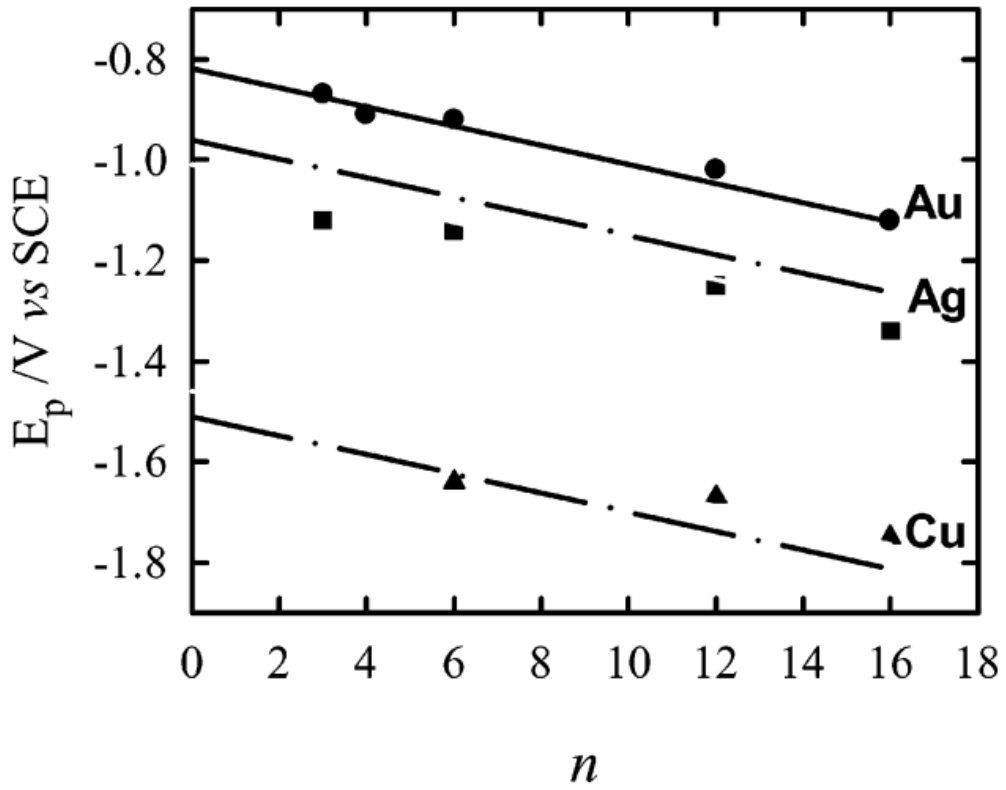

Figure 1-7 Estimated desorption potential vs n carbon units in the alkyl chains of alkanethiol SAMs on Au, Ag and Cu disk electrodes in alkaline methanolic electrolyte. Reprinted (adapted) with permission from J. Phys. Chem. B 2003, 107, 13446-13454 American Chemical Society

1.3 The Problem of Measurement

The measurement of SAM reductive stability on Au, Ag and Cu in figure 1-7 tells a compelling story about comparing the effect sizes of alkyl-chain lengths and the apparent effect of the metal identity on the reductive stability of SAMs. The slopes of the E_P vs n are roughly equivalent on the different metals which suggests that SAMs have similar Van der Waals interactions or hydrophobic penalties for reductive desorption, but a much larger shift in E_P comes from the identity of the metal controlling for the alkyl chain length. A hypothesis to explanation as to why the metal trend is observed is expanded upon in Chapter 4, but first a closer examination of the evolution in the understanding of SAM reductive desorption is in order.

1.3.1 Early Measurements

Porter in 1991 first proposed measuring SAM coverage using the peak from the desorption CVs. Using equation 1.3 and the charge found by integrating the desorption peak, the coverage estimates were greater than estimates from helium diffraction and scanning tunneling microscopy by 10% to 50% of the commonly accepted value of 7.7×10^{-10} moles cm^{-2} for Au<111> surfaces.[20,33]

$$\Gamma = Q/AnF \quad (1.3)$$

In 1.3, Γ is the area normalized coverage (mol cm^{-2}), Q is the charge passed in coulombs, A is the surface area of the electrode, n is the integer number electrons passed per mole, and F is Faraday's constant for converting coulombs to moles. The fundamental relationship to coverage

and current (i) is shown in equation 1.4, with a differential of surface coverage with respect to time.

$$(1.4) \quad i/nFA = d\Gamma/dt$$

Explicit modeling of a two dimensional current-potential relationship of SAM desorption CVs is virtually non-existent in the SAM desorption CV literature.[33] To give the reader a sense of the potential-current relationship, equation 1.5 is invoked from Bard and Faulkner for "Only Adsorbed O Electroactive—Irreversible Reaction" cyclic voltammetry.[28]

$$(1.5) \quad i = FAk_f\Gamma_O \exp\left[\left(\frac{RT}{\alpha F}\right)\left(\frac{k_f}{v}\right)\right],$$

$$k_f = k^0 \exp\left[-\alpha\frac{nF}{FT}\left(E - E^{0'}\right)\right] \exp\left[\alpha\frac{nF}{RT}vt\right]$$

Here, E is the potential of the of the electrode, $E^{0'}$ is the equilibrium potential, α is the transfer coefficient, R the gas constant, T for temperature, n is the integer number of electrons passed per mole, k^0 is the intrinsic rate constant and v is the scan rate (V/s). $E^{0'}$ is the potential which governs where reductive desorption is thermodynamically permitted, and inside the k_f term are the kinetic parameters which broaden the peak and distort its shape from symmetry. The desorption peak potential (E_P) was confirmed to be scan rate dependent, shifting negative with faster scan rates as modeled in equation 1.6. [17,28,33]

$$(1.6) \quad E_P = E^{0\prime} + \frac{RT}{n\alpha F}\ln\left(\frac{RT}{n\alpha F}\frac{k^0}{v}\right)$$

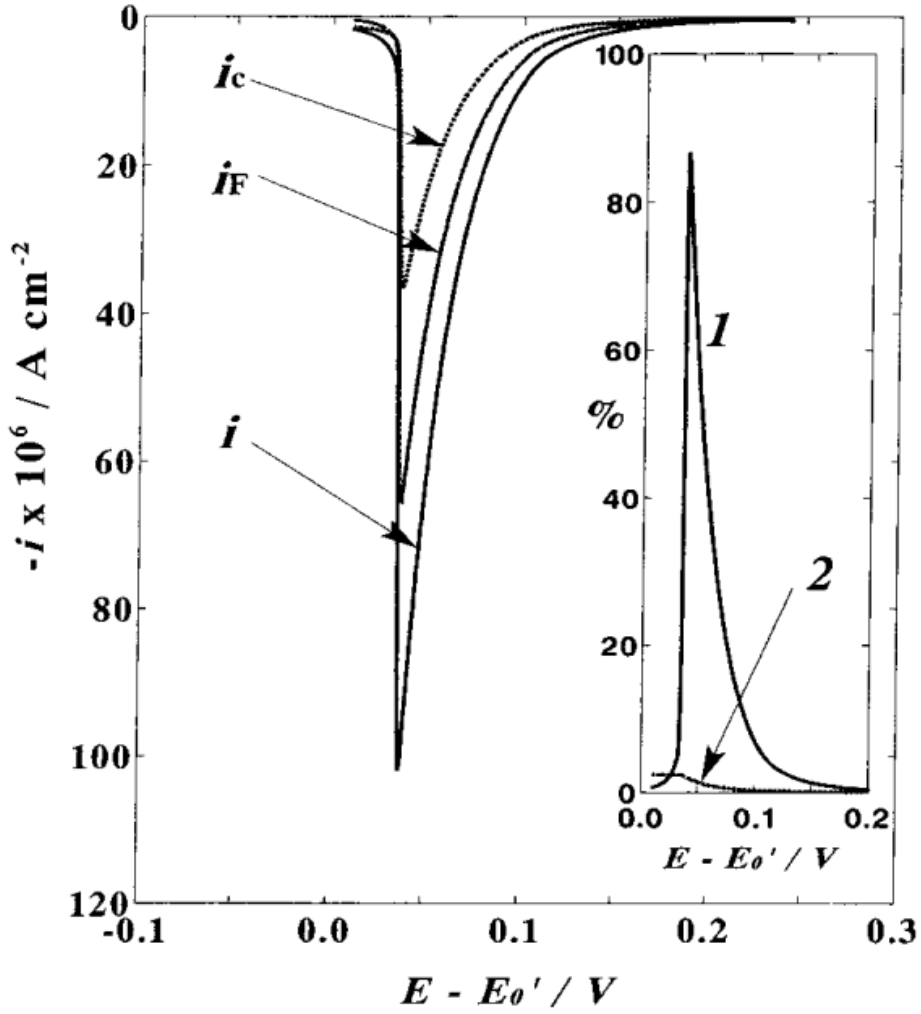

Figure 1-8 Kakiuchi's 2002 current potential model for SAM electrochemical desorption including non-faradaic charging currents (i_c) from the exchange of thiol for water at the surface, and the Faradaic charge (i_F) for the one-electron reduction of the thiol. Reprinted (adapted) with permission from Langmuir 2002, 18, 13, 5231–5238 American Chemical Society

A non-Faradaic charging current was included in Kakiuchi's 2002 model of SAM reductive desorption (figure 1-8) from the exchange of thiol for water molecules, which contribute an estimated 30% of the charge under the peak, as an explanation for the discrepancies between coverage values derived from voltammetry versus the microscopy techniques. In 2007, Laredo et al made similar arguments from a unique experiment estimating coverages from the Langmuir-Blodgett technique, and came to the conclusion that coverage measurement from reductive desorption CVs is systematically flawed from not accounting for the change in the double-layer and the SAM electrolyte exchange process.[34] These experiments were early hints that the reductive desorption process for alkyl-thiols on gold is a complex phenomenon, while others made more simplifying assumptions to prove that it's a one-electron process.

An often-cited proof that SAM reduction is a one-electron process is the 2004 work of Sumi and Uosaki, where the experimental conditions favored a quasi-reversible Nernstian process for SAM reductive desorption and oxidative re-adsorption.[17] In this experiment, decanethiol was dissolved in ethanolic 0.1 M potassium hydroxide at various concentrations from 10 μM to 1 mM. A gold working electrode was exposed to the ethanolic-thiol electrolyte for reductive desorption / oxidative adsorption CVs taken in the thiol solution, which is different than most other desorption measurements where the thiol is only present on the electrode surface and not in the bulk electrolyte solution. By having the thiol present in the electrolyte, a Nernstian expression (equation 1.7) using the equilibrium in equation 1.2 was used to explain the shift in E_P as a function of thiol concentration.

$$(1.7) \quad E_{1/2} = E^{0\prime} + \frac{RT}{nF} \ln \left(\frac{a_{C10-S-Au}}{a_{Au} a_{C10-S^-}}\right)$$

In equation 1.7, $E_{1/2}$ is the average of the reductive and oxidative peak potentials, $a_{C10\text{-}S\text{-}Au}$ is the activity for the SAM, a_{Au} is the activity for bare Au sites, and $a_{C10\text{-}S^-}$ is the activity for the thiolate

dissolved in the electrolyte. Assuming that n=1, and the activity of the surface thiol and bare Au are constant, a linear relationship of E_P with respect to the thiol bulk concentration (activity) is revealed in equation 1.8.

$$(1.8) \quad E_{1/2} = E^{0\prime} - 0.059 \log(a_{C10-S^-}) - constant$$

Figure 1-9 shows the results of plotting E_P vs log of the thiol concentration, which shows a linear relationship with a slope of 0.057 V/decade, in agreement with equation 1.8 and n=1 for the number of electrons passed per thiol. White's group used similar assumptions for measurements of thiols of different lengths on Ag and Au to estimate the ΔG of adsorption in methanolic and aqueous hydroxide solution as function of alkyl-chain length although double-peaks were noticeable in the CVs.[21,35]

Measurements of the SAM desorption with the thiol present in the bulk electrolyte paints a picture of a simple reversible process. More modern measurements using surface selective IR spectroscopy, fluorescence and microscopy techniques has revealed that SAM reductive desorption is a complex process and the fate and transport of the molecules after the initial reduction is heavily dependent on the SAM structure.

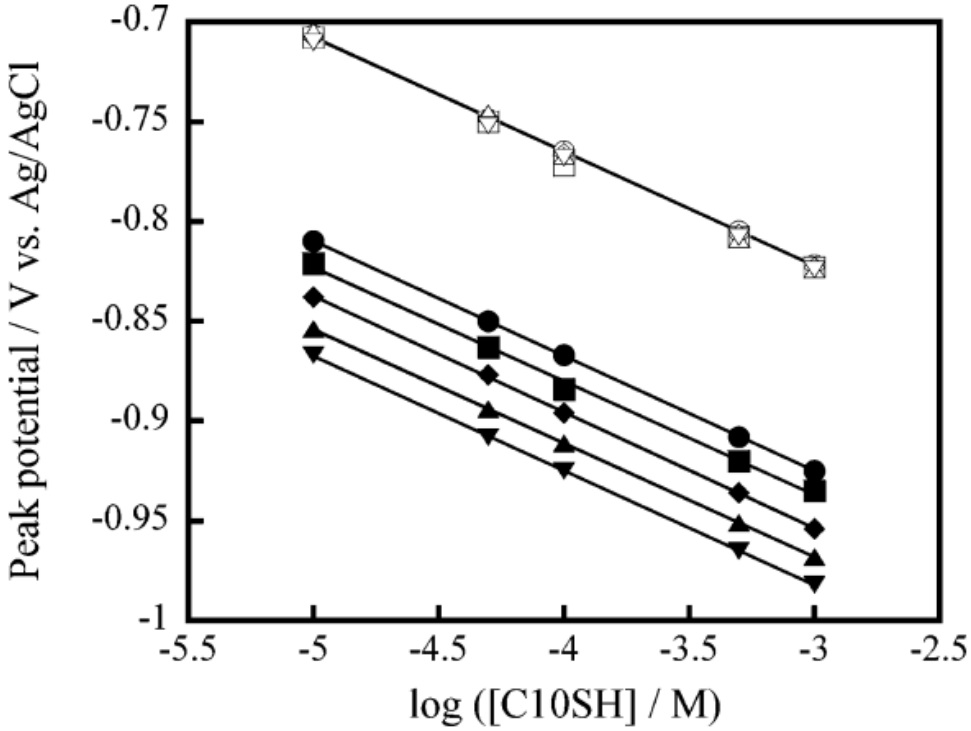

Figure 3. Anodic (filled) and cathodic (unfilled) peak potentials as a function of C10SH concentration in 0.1 M KOH ethanol solution. Sweep rates: ●, ○, 0.01 V s^{-1}; ■, □, 0.02 V s^{-1}; ◆, ◇, 0.05 V s^{-1}; ▲, △, 0.1 V s^{-1}; and ▼, ▽, 0.2 V s^{-1}.

Figure 1-9 f Reprinted (adapted) with permission from J. Phys. Chem. B 2004, 108, 20, 6422–6428 American Chemical Society

1.3.2 Spectroscopy and Microscopy of SAM Reductive Desorption and the Fate of the Cleaved Thiolates

Different groups using surface selective vibrational spectroscopy of the various C-H stretching modes of the alkyl backbone of alkanethiol SAMs on Au have concluded that not all thiols desorb from the surface at E_P. Pensa used polarization modulation infrared reflection absorption spectroscopy (PM-IRRAS), a surface selective IR technique, and electrochemical scanning tunneling microscopy (EC-STM), to probe the structure at the interface during reductive desorption of dodecanethiol (C12) and octadecanethiol (C18) Au-SAMs.[36] For C12-SAMs at reductive potentials, the formation of micellar aggregates and lying-down phases were observed indicating that the SAM was trapped at the interface in a disordered state between the electrolyte and the surface. For the C18 SAM, even though a reductive peak in the CV was observed, the ordering and tilt angle of the SAM was preserved through repeated scanning to reductive potentials suggesting no loss of the thiol to the bulk solution. Similar measurements using in-situ sum frequency generation (SFG), which is a more sensitive technique for probing ordered vibrational modes at the surface, arrived at similar conclusions for C18, but for decanethiol (C10), they concluded that most of the SAM completely desorbed and diffused into the bulk electrolyte after 4 reductive desorption CV cycles. In another study by Searson et al, fluorophore-labeled hexanethiol (C6) SAMs on Au also completely desorbed and diffused away from the surface at -1.3 V when monitored using fluorescence vs time, and the normalized time decay showed an excellent fit to a diffusion model using Fick's law of diffusion.[37] In the same study, fluorophore labelled undecanethiol (C11) partially desorbed from the surface and showed more complex time-dependent behavior that did not fit as well to the diffusion model. The use of time as a variable at a specified constant applied potential is often overlooked in measurements

of reductive desorption, although there is considerable evidence that it may be an important parameter.

1.3.3 Time Dependence

Most of the spectroscopic studies mentioned above rely on repeated CV cycling and monitor changes in the SAM structure over the cycles.[36,38,39] For a typical CV scan rate, the time spent at reductive potentials is a few seconds before scanning back to potentials where the thiolate can oxidatively re-attach to the surface. One study noted that the observation of a strong oxidative peak is somewhat dependent on the preparation of the Au surface, but evidence of an oxidative re-adsorption peak at ~ -1 V was supported by *operando* spectroscopic sum harmonic generation (SHG) during the voltammetry.[40] If the SAM diffusion away from the surface after electrochemical cleavage is slow enough that they can be oxidatively reattached upon the anodic sweep of the desorption CV, why haven't more studies looked specifically at time dependence on the diffusion away from the surface?

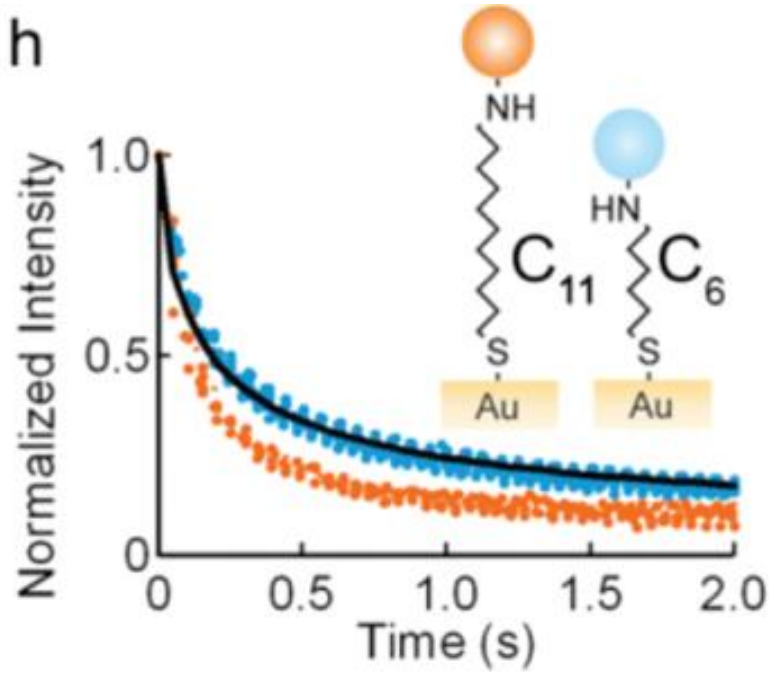

Figure 1-10 Searson et al fluorescence decay of fluorophore labelled SAM vs time at -1.3 V. Reprinted (adapted) with permission from Langmuir 2010, 26, 3, 1420–1423. American Chemical Society.

As mentioned above, Searson showed that holding the potential constant at -1.3 V vs AgCl, a fluorophore labeled C6-thiol showed desorption kinetics that was modeled with diffusion, while a C11-thiol showed more complex behavior .[37] Searson also had presented a similar diffusion model (equation 1.9) in earlier work that relied solely on the observation of a oxidative re-adsorption peak in a linear sweep voltammogram after holding the potential constant at -1.4 V vs AgCl.[19] In equation 1.9, Γ(t) is the time dependent coverage adjacent to the surface with the oxidative peak area and Γ^0 is the initial coverage, D is the diffusion coefficient of the thiol molecule, C_S is the bulk solubility and t is time in seconds.

$$\Gamma(t) = \Gamma^0 - \frac{2\sqrt{D}}{\sqrt{\pi}} C_s \sqrt{t} \quad (1.9)$$

In Searson's work, the ability to measure diffusion away from the surface with the oxidative peak was heavily dependent on the length of the thiol, with no peak observed for C9-SAM, a time-dependent peak for C11-SAM, and a time-independent peak for C13 or greater SAMs suggesting that they don't readily diffuse away from the surface. From the C11 time dependent data and equation 1.9, Searson's model was able to predict a bulk solubility (mol/L) consistent with previous measurements made in 1958.[19,30]

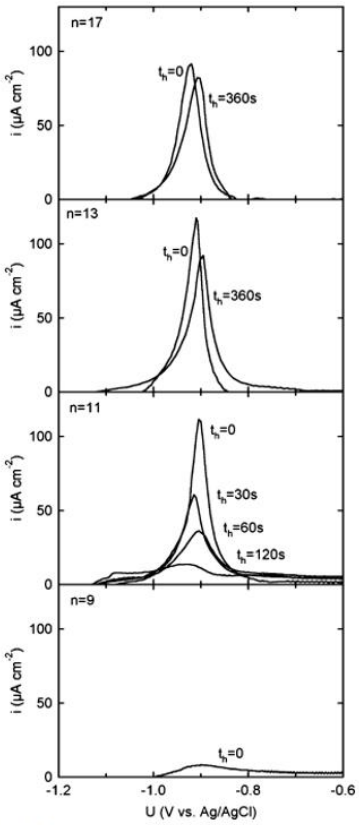

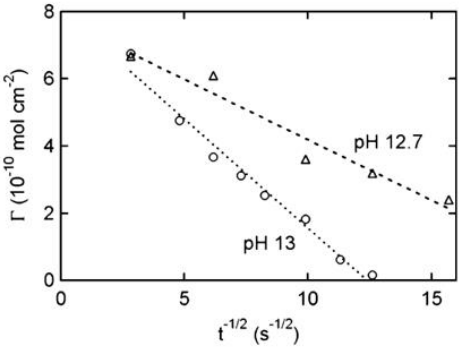

Figure 4. Surface concentration versus $t^{1/2}$ for dodecanethiol in pH 13 and pH 12.7 KOH.

Figure 1-11 Figure from Searson paper showing time dependence of SAM oxidative readsorption peaks on the right. Left shows C12 time dependent coverage data linearized with the square root of time. Reprinted (adapted) with permission from Langmuir 2006, 22, 8, 3474–3476 American Chemical Society.

Data points for time dependence of a C14-SAM desorption is located in a 2007 paper by Lennox which can be used to test Searson's model independent of their data.[41] Lennox measured the change in coverage of a C14-SAM vs time at -1.4 V by back-labeling the desorbed sites with ferrocene-dodecanethiol but did not use the Season model in their paper. The following analysis is my own. Under the assumption that the increase in measured ferrocene coverage corresponds to a one-to-one loss of C14-thiol from the surface, Searson's model can be tested using the data points. Figure 1-12, right, shows the time dependent data extracted from the Lennox paper, table 1, subtracted from the accepted value for SAM coverage (7.7×10^{-10} mol cm^{-2}) vs the square root of time at -1.4 V. Using equation 1.9 and assuming the diffusion coefficient was 1×10^{-6} cm^2 s^{-1} (see Searson paper), the bulk solubility was solved from the slope of the linear fit of the data. The resulting log of the bulk solubility from the Lennox paper lies on the line of log bulk solubilities for alkanethiols reported by Reid in 1958.[30] This analysis suggests that Searson's model is able to predict bulk solubilities from the time dependent measurement of coverage decay at reductive potentials where the SAM is cleaved from the surface using a diffusion-based model after electrochemical cleavage of the Au-S bond. The consequences of time dependence on the interpretation of desorption data are explored in chapter 3 of this thesis, which suggests that measurements made after shorter time periods at desorption potentials are measuring SAM coverages that are not stable over time, which would distort the interpretation of electrocatalytic activity if the coverage of the tethering SAM is changing over time.

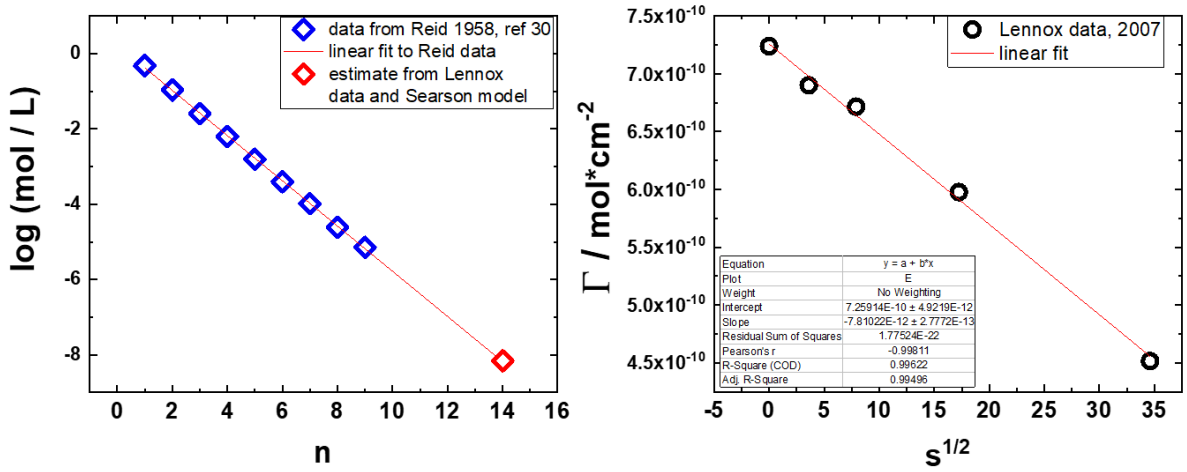

*Figure 1-12 Right: Alkanethiol coverage versus time from Lennox paper. C14-SAM coverage estimates as a function of the square root of time by subtracting ferrocene peak coverage from 7.7 * 10^{-10} mol cm^{-2}. The resulting slope was converted to a bulk solubility estimate for C14-thiol, which the log of the bulk solubility was plotted with log bulk solubilities of alkyl thiols reported by Reid in 1958 (left).*

1.4 Conclusions and Over View of Works in this Thesis

The electrochemical reductive stability of alkanethiol SAMs from metal electrodes can be summed up by two important trends; dependence on the SAM structure and dependence on the metal substrate identity. While Au-SAMs exhibit desirable characteristics for studying tethered electrocatalysts, their reductive potential stability limits (-1 V vs AgCl) prohibit their use in serious study of CO_2 and NO_3^- reduction electrocatalysts which operate at -1.5 V vs AgCl in alkaline aqueous electrolytes. The SAMs on other transition metals such as Cu appear to be more reductively stable than Au, but alternative methods (ring disk voltammetry) are required for estimating the reductive potential limits because of the absence of E_P in the voltammetry. The methods for studying the SAM reductive desorption have evolved over the decades to include spectroscopic and microscopy techniques that show the phenomenon is more complex than originally conceived, with the desorption into the bulk solution not observed for longer chained alkyl thiols. Other works have proposed a diffusion model after the reductive cleavage of the Au-S bond, which implies time dependence will affect the interpretation of desorption data. In order to understand how to create more reductively stable SAMs on other metals, more direct quantitative measurement of SAM stability as a function of applied potential is necessary to measure the coverage dependent SAM stability on other metals which do not present a desorption peak in the CVs, and time as a variable should be included in the assessment of stability at a given potential due to the time scale of diffusion of low bulk solubilities of the alkanethiols in aqueous electrolytes.

In Chapter 2, I directly confront challenges highlighted in section 1.3 about finding robust methodology to quantitatively measure SAM stability as a function of applied potential.

The approach uses quantitative analysis of ferrocene-SAM (Fc-SAM) coverage as a function of applied potential. The Fc-SAM CV peaks yield easy, quantitative measurements of coverage when the Fc-SAM is in the pristine state before any reductive potentials are applied, but after applying desorption potentials, the CV baseline becomes non-linear and challenging to distinguish from the Fc peaks. To overcome the baseline issue, a combination of empirical CV baselines collected after applying reductive potentials to blank decanethiol-SAMs were used in combination with machine learning regression algorithms and peak-fitting libraries in Python to achieve accurate surface coverage measurements from Fc-SAM CV peak measurements after applying reductive potentials. The accuracy of the machine learning approach was benchmarked against secondary measurements of Fc coverage using ICP-MS and found to be in good agreement. Future works in electrochemical SAMs should build upon this work and incorporate the plethora of data found in electrochemical measurements along with the data science and machine learning tools that are quickly becoming routine in other fields.

In Chapter 3, I directly address the often-ignored issue of whether there is a time dependence to SAM desorption due to slow mass transfer from the surface into the bulk, and how time dependence correlates to the solubility of the thiol molecules in the electrolyte. Here the Fc-SAM coverages were measured over different time intervals at a constant applied reduction potential. Identical control experiments were conducted with increasing methanolic content in the electrolyte to explore the solubility hypothesis. A clear time dependence in the Fc-SAM coverage is observed for at least the first 15 minutes in all of the electrolytes, with the biggest changes observed in the higher concentration of methanolic electrolytes directly relating back to the time dependent model presented in 1.3.3 which incorporates solubility and Fickian diffusion, after the cleavage of the Au-S bond, as a driver for the time dependence for SAM

desorption. In light of this work, future experiments should consider how the rate of mass transfer away from electrochemical surfaces can influence their interpretation of their surface measurements with respect to stability.

In Chapter 4, the foundations of exciting new work in directly measuring the electrochemical cleavage of the Au-S bond for the first time is presented using grazing incidence X-ray Absorbance Fine Structure and a specially designed electrochemical cell. The information acquired in this experiment presents an unprecedented window into what is happening at the interface of the electrode surface. Direct observation of the disappearance of the S signals during reducing potentials is the first step in confirming the hypothesis of Au-S bond cleavage, which has been postulated, but never verified, for over the 30 plus years of SAM electrochemical desorption literature. The work presented here paves the way for future measurements of SAM interactions on other metals besides Au, which is the most important step in understanding how to create reductively stable SAM systems for tethering reductive electrocatalysts.

1.5 References

(1) Love, J. C.; Estroff, L. A.; Kriebel, J. K.; Nuzzo, R. G.; Whitesides, G. M. "Self-assembled monolayers of thiolates on metals as a form of nanotechnology," *Chem. Rev.* **2005**, *105*, 1103-1170.
(2) Eckermann, A. L.; Feld, D. J.; Shaw, J. A.; Meade, T. J. "Electrochemistry of redox-active self-assembled monolayers," *Coord. Chem. Rev.* **2010**, *254*, 1769-1802.
(3) Savéant, J.-M. "Molecular Catalysis of Electrochemical Reactions. Mechanistic Aspects," *Chem. Rev.* **2008**, *108*, 2348-2378.
(4) Bard, A. J. "Inner-Sphere Heterogeneous Electrode Reactions. Electrocatalysis and Photocatalysis: The Challenge," *J. Am. Chem. Soc.* **2010**, *132*, 7559-7567.
(5) Collman, J. P.; Devaraj, N. K.; Decréau, R. A.; Yang, Y.; Yan, Y.-L.; Ebina, W.; Eberspacher, T. A.; Chidsey, C. E. "A cytochrome c oxidase model catalyzes oxygen to water reduction under rate-limiting electron flux," *Science* **2007**, *315*, 1565-1568.
(6) Sengupta, K.; Chatterjee, S.; Samanta, S.; Dey, A. "Direct observation of intermediates formed during steady-state electrocatalytic O₂ reduction by iron porphyrins," *Proc. Natl. Acad. Sci. U.S.A.* **2013**, *110*, 8431.
(7) Reimers, J. R.; Ford, M. J.; Halder, A.; Ulstrup, J.; Hush, N. S. "Gold surfaces and nanoparticles are protected by Au(0)–thiyl species and are destroyed when Au(I)–thiolates form," *Proc. Natl. Acad. Sci. U.S.A.* **2016**.
(8) Vericat, C.; Vela, M. E.; Benitez, G.; Carro, P.; Salvarezza, R. C. "Self-assembled monolayers of thiols and dithiols on gold: new challenges for a well-known system," *Chem. Soc. Rev.* **2010**, *39*, 1805-1834.
(9) Chidsey, C. E. D.; Bertozzi, C. R.; Putvinski, T. M.; Mujsce, A. M. "Coadsorption of ferrocene-terminated and unsubstituted alkanethiols on gold: electroactive self-assembled monolayers," *J. Am. Chem. Soc.* **1990**, *112*, 4301-4306.
(10) Collman, J. P.; Devaraj, N. K.; Chidsey, C. E. "“Clicking” functionality onto electrode surfaces," *Langmuir* **2004**, *20*, 1051-1053.
(11) Collman, J. P.; Devaraj, N. K.; Eberspacher, T. P. A.; Chidsey, C. E. D. "Mixed Azide-Terminated Monolayers: A Platform for Modifying Electrode Surfaces," *Langmuir* **2006**, *22*, 2457-2464.
(12) McCrory, C. C. L.; Penner-Hahn, J. E.; National Science Foundation: University of Michigan Ann Arbor, 2019; Vol. $598,994.
(13) Froehlich, J. D.; Kubiak, C. P. "Homogeneous CO2 Reduction by Ni(cyclam) at a Glassy Carbon Electrode," *Inorg. Chem.* **2012**, *51*, 3932-3934.
(14) Ma, L.; Zhang, B.-Y.; Li, H.-L.; Chambers, J. Q. "Kinetics of nitrate reduction by cobalt-cyclam incorporated Nafion® redox polymer," *J. Electroanal. Chem.* **1993**, *362*, 201-205.
(15) Machan, C. W.; Sampson, M. D.; Chabolla, S. A.; Dang, T.; Kubiak, C. P. "Developing a mechanistic understanding of molecular electrocatalysts for CO2 reduction using infrared spectroelectrochemistry," *Organometallics* **2014**, *33*, 4550-4559.

(16) Filali, A.; Yaouanc, J.-J.; Handel, H. "Stoichiometric Mono N-Functionalization of Tetraazamacrocycles via Phosphoryl-Protected Intermediates," *Angewandte Chemie International Edition in English* **1991**, *30*, 560-561.
(17) Sumi, T.; Uosaki, K. "Electrochemical Oxidative Formation and Reductive Desorption of a Self-Assembled Monolayer of Decanethiol on a Au(111) Surface in KOH Ethanol Solution," *The Journal of Physical Chemistry B* **2004**, *108*, 6422-6428.
(18) Salvarezza, R. C.; Carro, P. "The electrochemical stability of thiols on gold surfaces," *J. Electroanal. Chem.* **2018**, *819*, 234-239.
(19) Pesika, N. S.; Stebe, K. J.; Searson, P. C. "Kinetics of Desorption of Alkanethiolates on Gold," *Langmuir* **2006**, *22*, 3474-3476.
(20) Widrig, C. A.; Chung, C.; Porter, M. D. "The electrochemical desorption of n-alkanethiol monolayers from polycrystalline Au and Ag electrodes," *Journal of electroanalytical chemistry and interfacial electrochemistry* **1991**, *310*, 335-359.
(21) Hatchett, D. W.; Uibel, R. H.; Stevenson, K. J.; Harris, J. M.; White, H. S. "Electrochemical measurement of the free energy of adsorption of n-alkanethiolates at Ag (111)," *J. Am. Chem. Soc.* **1998**, *120*, 1062-1069.
(22) Luo, M.; Frechette, J. "Electrochemical Stability of Low-Density Carboxylic Acid Terminated Monolayers," *The Journal of Physical Chemistry C* **2010**, *114*, 20167-20172.
(23) Buck, M. "Structure, Electrochemistry and Applications of Self-Assembled Monolayers of Thiols," *Chemically Modified Electrodes* **2009**, *11*, 197-255.
(24) Kim, Y.-K.; Koo, J. P.; Huh, C.-J.; Ha, J. S.; Pi, U. H.; Choi, S.-Y.; Kim, J. "Adsorption behavior of binary mixed alkanethiol molecules on Au: Scanning tunneling microscope and linear-scan voltammetry investigation," *Appl. Surf. Sci.* **2006**, *252*, 4951-4956.
(25) Doneux, T.; Steichen, M.; De Rache, A.; Buess-Herman, C. "Influence of the crystallographic orientation on the reductive desorption of self-assembled monolayers on gold electrodes," *J. Electroanal. Chem.* **2010**, *649*, 164-170.
(26) Yang, D.-F.; Wilde, C.; Morin, M. "Electrochemical desorption and adsorption of nonyl mercaptan at gold single crystal electrode surfaces," *Langmuir* **1996**, *12*, 6570-6577.
(27) Yeon, H.; Wang, C.; Van Lehn, R. C.; Abbott, N. L. "Influence of Order within Nonpolar Monolayers on Hydrophobic Interactions," *Langmuir* **2017**, *33*, 4628-4637.
(28) Bard, A. J.; Faulkner, L. R.; Leddy, J.; Zoski, C. G. *Electrochemical methods: fundamentals and applications*; wiley New York, 1980; Vol. 2.
(29) Shaver, A.; Curtis, S. D.; Arroyo-Currás, N. "Alkanethiol Monolayer End Groups Affect the Long-Term Operational Stability and Signaling of Electrochemical, Aptamer-Based Sensors in Biological Fluids," *ACS Applied Materials & Interfaces* **2020**, *12*, 11214-11223.
(30) Reid, E. E. *Organic chemistry of bivalent sulfur*; Chemical Publishing Company, 1958; Vol. 1.
(31) Devaraj, N. K.; Decreau, R. A.; Ebina, W.; Collman, J. P.; Chidsey, C. E. "Rate of interfacial electron transfer through the 1, 2, 3-triazole linkage," *The Journal of Physical Chemistry B* **2006**, *110*, 15955-15962.
(32) Azzaroni, O.; Vela, M. E.; Fonticelli, M.; Benítez, G.; Carro, P.; Blum, B.; Salvarezza, R. C. "Electrodesorption Potentials of Self-Assembled Alkanethiolate Monolayers on Copper Electrodes. An Experimental and Theoretical Study," *The Journal of Physical Chemistry B* **2003**, *107*, 13446-13454.

(33) Kakiuchi, T.; Usui, H.; Hobara, D.; Yamamoto, M. "Voltammetric Properties of the Reductive Desorption of Alkanethiol Self-Assembled Monolayers from a Metal Surface," *Langmuir* **2002**, *18*, 5231-5238.
(34) Laredo, T.; Leitch, J.; Chen, M.; Burgess, I. J.; Dutcher, J. R.; Lipkowski, J. "Measurement of the Charge Number Per Adsorbed Molecule and Packing Densities of Self-Assembled Long-Chain Monolayers of Thiols," *Langmuir* **2007**, *23*, 6205-6211.
(35) Hatchett, D. W.; White, H. S. "Electrochemistry of Sulfur Adlayers on the Low-Index Faces of Silver," *The Journal of Physical Chemistry* **1996**, *100*, 9854-9859.
(36) Pensa, E.; Vericat, C.; Grumelli, D.; Salvarezza, R. C.; Park, S. H.; Longo, G. S.; Szleifer, I.; De Leo, L. P. M. "New insight into the electrochemical desorption of alkanethiol SAMs on gold," *PCCP* **2012**, *14*, 12355-12367.
(37) Ghaly, T.; Wildt, B. E.; Searson, P. C. "Electrochemical release of fluorescently labeled thiols from patterned gold surfaces," *Langmuir* **2010**, *26*, 1420-1423.
(38) Cai, X.; Baldelli, S. "Surface Barrier Properties of Self-Assembled Monolayers as Deduced by Sum Frequency Generation Spectroscopy and Electrochemistry," *The Journal of Physical Chemistry C* **2011**, *115*, 19178-19189.
(39) Jacob, J. D. C.; Lee, T. R.; Baldelli, S. "In Situ Vibrational Study of the Reductive Desorption of Alkanethiol Monolayers on Gold by Sum Frequency Generation Spectroscopy," *The Journal of Physical Chemistry C* **2014**, *118*, 29126-29134.
(40) Thom, I.; Buck, M. "Electrochemical stability of self-assembled monolayers of biphenyl based thiols studied by cyclic voltammetry and second harmonic generation," *Surf. Sci.* **2005**, *581*, 33-46.
(41) Lee, L. Y. S.; Lennox, R. B. "Electrochemical Desorption of n-Alkylthiol SAMs on Polycrystalline Gold: Studies Using A Ferrocenylalkylthiol Probe," *Langmuir* **2007**, *23*, 292-296.

Chapter 2 Estimating Bias from Background Correcting Cyclic Voltammograms of Non-Ideal Ferrocene-Self Assembled Monolayers After Reductive Desorption: Comparing Traditional Interpolation Approaches to Machine Learning with Empirical Baselines, and Other Peak Fitting Methods

2.1 Introduction

Baseline correction of cyclic voltammetry (CVs) peaks for the quantitative analysis of redox-active self-assembled monolayers (SAMs) on Au surfaces is challenging when the system is non-ideal. In an ideal electrochemical SAM system, the baseline is flat or constantly sloped from double-layer charging which is easy to approximate using linear interpolation, but in non-ideal systems where the baseline appears to be non-linear or peak shaped, baseline correction becomes a source of bias in the peak analysis.[1] Non-ideality in the electrochemistry of SAMs is typically found in complex systems such as SAM based biosensors, or in SAMs with defects that permit electrolyte interactions with the Au surface.[2] Understanding the physical processes that give rise to the complex charging responses in CVs has been the subject of recent reviews because of their implications in electrochemical energy storage at interfaces, and the distortion they cause in electrochemical SAM-based biosensor signals.[3-5] A variety of models were proposed to explain capacitive and pseudo-capacitive waveforms caused by the intercalation of ions, or specific interactions with electrode surfaces, but there are no models outside of double-layer charging that can be applied universally.[3] The lack of explicit models when faced with undocumented or unprecedented scenarios for baseline correction is a source of uncertainty in

the peak area analysis.[6,7] In this work, the problem of non-ideal electrochemical background correction is confronted in the measurement of ferrocene-capped (Fc) alkanethiol SAM coverages after the application of reductive desorption potentials which introduce complexity in the baselines of the CVs.

After decades of research, mixed Fc-SAMs, where a Fc-capped alkanethiol and a diluent unfunctionalized alkanethiol are co-deposited on a gold surface, have become the de-facto standard for exhibiting ideal peak waveforms in CVs for a surface-attached redox group.[8] The peak response closely matches the curve shape predicted by electrochemical theory.[9] A modern method to produce ideal Fc-SAMs uses co-deposition of azide-terminated undecanethiol along with a diluent decanethiol to space-out the functionalized azido-thiols on the surface, followed by the Cu(I) click reaction with ethynyl-ferrocene to form a triazole linkage between the SAM and the redox-active Fc group.[10] The clicked Fc-SAMs are renowned for the ideal CV peak response compared to their earlier predecessors, and the baselines of the CVs are ideal because of the well-packed qualities of the SAMs, which block interactions with the underlying Au surface. As will be shown below, applying reductive desorption potentials to the ideal Fc-SAM system changes the CV baselines from ideal to non-ideal. The observation of non-ideal background currents in disordered Fc-SAMs with features that overlap with the Fc peak, will be shown to strongly correlate with features observed experimentally on bare Au surfaces. These background features can also be reproduced on unfunctionalized alkanethiol SAMs after the application of reductive potentials.

In this work, the goal is to examine the bias in the Fc peak area measurement created by employing background correction techniques to non-ideal CV baselines. First, the bias from choosing an interpolation range in using linear interpolation to baseline correct non-ideal CVs

will be exposed. Second, new baseline correction techniques are explored which employ the empirical baselines from CVs of reductively disordered "blank" SAMs without the Fc redox group, in conjunction with a machine learning algorithm to construct a weighted average of the empirical baselines. The machine learning algorithm can be employed as an interpolation technique, or in conjunction with peak fitting algorithms to fit all of the data simultaneously, which can eliminate bias from having to choose an interpolation range. All of the models are compared to a secondary measurement of Fc-SAM coverage after reductive desorption using inductively coupled plasma mass spectrometry (ICP-MS) to benchmark the bias produced from each approach. The following will show that reductively disordered and partially-desorbed Fc-SAM coverages can be accurately estimated despite non-ideal electrochemical baselines in the voltammetry by combining empirical baselines with the use of machine learning and peak fitting techniques, and that in non-ideal voltammetry, linear interpolation exposes the peak area analysis to bias when the analyst must arbitrarily choose the interpolation range.

The key takeaway is that the bias introduced from a simple and popular data treatment, linear interpolation for baseline correction, is an under-reported sources of bias in analytical treatment of electrochemical peaks, and there is a dearth of systematic and broadly-accepted methodologies to approach non-ideal baselines in electrochemistry. New approaches are introduced and validated in this work in the hopes to open up broader discussion and consensus on systematic approaches to non-ideal baseline correction.

2.2 Experimental Methods

2.2.1 Materials

Chemicals were used as received. Water was purified to 18.2MΩ cm resistivity with a Thermo Scientific GenPure UV-TOC/UF x CAD-plus water purification system. 11-bromo-1-

undecanol was purchased from Accela. Methanesulfonyl chloride (99.5%), copper (II) sulfate pentahydrate (99+%), and potassium thioacetate (98%) were purchased from Acros Organics. Ferrocenecarboxylic acid was purchased from Aldrich. Perchloric acid (ACS, 60-62%), L-(+)-ascorbic acid (ACS, 99+%), tripropargylamine (97%), benzyl azide (94%), copper (II) acetate (anhydrous powder), and decanethiol (96%) were purchased from Alfa Aesar. Ethynylferrocene was acquired from Chem Scene. Ethanol (200 proof, anhydrous) was purchased from Decon Laboratories. Ethyl Ether was purchased from Fisher. Hydrochloric acid (GR ACS) was purchased from Millipore. Sodium phosphate monobasic and dibasic (Bioultra ≥ 99.0%) were purchased from Sigma. Potassium Hydroxide (ACS reagent, >85% pellets), methanol (HPLC grade, ≥ 99.9%), N,N-dimethylformamide (anhydrous, 99.8%), triethylamine (≥99%), tetrahydrofuran (anhydrous, ≥99.9%), sodium bicarbonate (ACS reagent >99.7%), tert-butanol (ACS reagent, ≥99.0%), and dimethyl sulfoxide (ACS reagent ≥ 99.9%) were purchased from Sigma-Aldrich. Potassium chloride (99%) and sodium azide were purchased from Thermo Scientific. Si wafers were purchased from University Wafers.

Trace metal chemicals for ICP-MS experiments: Nitric acid (TraceMetal Grade, 67-70% HNO_3) and hydrochloric acid (TraceMetal Grade, 34-37% HCl) were purchased from Fisher Chemical. Perchloric acid (Aristar Plus for trace metal analysis) was purchased from VWR Chemicals. Dimethyl sulfoxide (≥99.99995% metals basis) was from Sigma-Aldrich. Copper(II) sulfate (Puratronic) was purchased from Alfa Aesar. Trace metal potassium hydroxide (Fluka) was purchased from Honeywell. The iron ICP-MS standard (1000 ppm Fe in 3 % HNO_3) was acquired from RICCA.

2.2.2 Synthesis of 1-Azidoundecane-11-thiol

1-Azidoundecane-11-thiol was synthesized following the procedure by Collman et al.[10] The following is a brief summary of the reaction steps:

1) *1-azidoundecan-11-ol* was synthesized by adding slight molar excess of sodium azide to bromo-undecanol in DMF, and refluxing under nitrogen for 24 hours followed by liquid-liquid extraction with diethyl ether and isolated by evaporating the ether, and then dried with $MgSO_4$ to yield a lightly yellow colored oil. (Note: Sodium azide is toxic and explosive. Use caution in handling the materials. *It was determined that the reaction proceeds more safely without reflux at room temperature, for the same 24-hour reaction time.*) ^{1}HNMR ($CDCl_3$, 400 MH_z): 3.63, (q, 2H); 3.25 (t, 2H); 1.57 (m, 4H); 1.22-1.4 (m, 14H).

2) *1-azidoundecan-11-methylsulfonate* was synthesize by adding triethylamine dissolved in THF, dropwise from a sep-funnel, into a reaction flask containing 1-azidoundecanol and a slight molar excess of methane sulfonyl-chloride in THF, followed by stirring for 2 to 4 hours. The reaction was quenched with ice-cold water and the organic phase was separated with diethyl ether extractions, followed by sequential washes of hydrochloric acid, water, sodium bicarbonate, and water. The product was dried with $MgSO_4$ and isolated with a rotovap to remove the ether, leaving behind a yellow oil. ^{1}HNMR ($CDCl_3$, 400 MH_z): 4.21, (t, 2H); 3.24 (t, 2H); 2.99 (s, 3H); 1.74 (m, 2H); 1.59 (m, 2H); 1.22-1.42 (m, 14H).

3) *1-azidoundecan-11-thioacetate* was synthesized by dissolving 1-azidoundecan-11-methylsulfonate in methanol with slight molar excess (~1.15 mol equiv.) of potassium thioacetate in methanol. The solution was degassed on a Schlenk-line using freeze-pump-thaw. After degassing, the reaction mixture was refluxed under nitrogen for 3 to 5 hours and then cooled to room temp under a nitrogen atmosphere. Ice cold water was added and the reactant was extracted with diethyl ether, washed 3 times with water, and dried with $MgSO_4$. The product was

isolated using a rotovap to remove the ether leaving behind the product as a yellow oil. ^{1}HNMR ($CDCl_3$, 400 MH_z) 3.24 (t, 2H); 2.85 (t, 2H); 2.31 (s, 3H); 1.5-1.61 (m, 4H); 1.22-1.4 (m, 14H).

4) *1-azidoundecanethiol* was synthesized by dissolving 1-azidoundecanethioacetate in methanol, and thoroughly degassing the flask using three or more freeze-pump-thaw cycles. (Note: Incomplete degassing will yield disulfide side product in the product detected by characteristic disulfide-adjacent methylene peaks (^{1}HNMR), a triplet at 2.66 ppm in $CDCl_4$.) Concentrated hydrochloric acid was added to the reaction flask while maintaining nitrogen atmosphere, and then refluxed under nitrogen for five hours. After cooling to room temp, ice cold water was added and the product was extracted with diethyl ether, washed three times with water, dried with $MgSO_4$ and isolated by evaporating the ether. ^{1}HNMR ($CDCl_3$, 400 MH_z): 3.24 (t, 2H); 2.51 (q, 2H); 1.59 (m, 4H); 1.22-1.41 (m, 14H).

2.2.3 Synthesis of tris[(1-benzyl-1H-1,2,3-triazol-4-yl)methyl]amine (TBTA)

TBTA was synthesized using the "modified TBTA synthesis" found in "Cu(II)-Catalyzed Oxidative Formation of 5,5′-Bistriazoles" by Brassard et al.[11] To briefly summarize, benzyl-azide was dissolved in t-butyl-alcohol with tripropargylamine and copper acetate. (Note: a slightly warm water bath will keep the t-butyl alcohol from freezing until the reaction starts.) Nitrogen was pumped into the flask to displace the oxygen and a rubber septum kept the flask closed off to the atmosphere during the overnight reaction stirring at room temperature. Diethyl ether was added the next day to precipitate the product which was collected via vacuum filtration.

2.2.4 Gold Electrodes

Gold electrodes were prepared by physical vapor deposition of a 20-25 nm titanium adhesion layer followed by 200-250 nm of gold onto silicon wafers using an Angstrom Engineering Evovac Evaporator in the clean room at the Lurie Nanofabrication Facility.

2.2.5 Preparation of Mixed Ferrocene-capped Self-Assembled Monolayers on Au Electrodes

One millimolar stock solutions of 1-azidoundecane-11-thiol and decanethiol in neat ethanol were prepared as separate solutions. For a desired mole-fraction of azido-thiol in the deposition solution (χ), the stock solutions were added to a beaker with proportionate volumes of the stock thiol solutions to achieve the desired χ, then stirred for five minutes using a stir bar/magnetic stir plate to thoroughly mix the solution in a chemical fume hood. Freshly evaporated Au coated silicon wafers were hand-cut into ~ 1 cm x 2 cm coupons using a glass cutter and placed into a 20 mL scintillation vials. The mixed thiol solution was added to the scintillation vials with the Au coupons, and capped tightly, wrapped in aluminum foil, and stored in the dark for four days.

The reaction of ethynylferrocene with azide-terminated SAMs was adapted from work of Collman et al.[12] After four days of thiol deposition, the "Cu(I) Click" solution was prepared first by dissolving Cu (II) sulfate pentahydrate (7.5 mg) into 25 mL of purified water. Next TBTA (21 mg), and ethynylferrocene (21 mg) were dissolved in 75 mL of dimethylsulfoxide (DMSO). The water solution containing Cu(II) and DMSO solutions with TBTA and ethynylferrocene, were combined in a beaker and stirred using a stir bar and magnetic stir plate, in a chemical fume hood, until the heat of solvation dissipated and the resulting solution returned to room temperature. While the DMSO/water solution was cooling, the Au coupons with the deposited thiols were removed from the vials, thoroughly rinsed with copious amounts of ethanol and purified water, and returned to clean scintillation vials. 70 mg of ascorbic acid was added to the

DMSO/water solution and stirred for 5 minutes before adding the solution to the vials containing the Au-SAMs. The vials were capped and stored in the dark overnight to allow the Cu click reaction to proceed, after which the Au-SAMs were removed from the DMSO/water solutions, and thoroughly rinsed with ethanol, dichloromethane and water, and then stored in clean dry scintillation vials in the dark until needed.

For Fc-SAMs used in the ICP-MS experiments, the same procedure as above was used, with the exception of the size of the electrodes, and the use of trace-metal grade chemicals, which were cut to approximately 20 cm^2 pieces from the full wafers which were stored in appropriately sized jars. All of the glassware for the deposition, click reaction, and stock solutions, and the electrochemical cell with O-rings, were pre-cleaned with concentrated aqua regia for several minutes to oxidize and dissolve trace metal contaminants before rinsing thoroughly with purified water. The cleaning procedure was repeated 2 times between experiments. Caution is advised when working with aqua regia as it is a strong energetic oxidant which can severely injure or cause death if handled improperly.

2.2.6 Electrochemical Methods

Electrochemical measurements were made using either a Bio-Logic SP200 or SP300 potentiostat. For standard electrochemical measurements, the electrochemical cell (figure 2-1) for analyzing the Au-Fc-SAMs is a Teflon cone with a hollow body, open at the top (~ 2-inch inner diameter) to accommodate a Teflon lid with holes for the graphite counter-electrode, and a AgCl reference electrode hanging into the electrolyte solution in the body of the cell. The bottom of the cone cell narrows to a tip, with an opening pressed against a Viton O-ring sitting on top of the Au-Fc-SAM sample for analysis. The inner diameter of the O-ring, 0.153 cm^2, defines the geometric surface area of the electrode. Electrical contact with the working Au electrodes is

made using copper tape tapped to the Au sample sticking out from under the O-ring outside of the cone cell. The reference electrode was a custom made AgCl / saturated KCl cell, with the AgCl coated Ag electrode housed in a glass body with a porous glass frit capping one end.

2.2.7 Scripting

Python version 3.3.7 was used as the base software language for all of the background correction methods presented in this text. The standard python libraries of NumPy, pandas and matplotlib were used for formatting arrays, database construction and visualization in Jupyter notebooks on a Windows machine. The LASSO fitting algorithm was employed by calling scikit-learn's machine learning library function (linear_model.Lasso) and non-linear least squares for peak-fitting was accomplished using the LMFIT program also in written in Python.

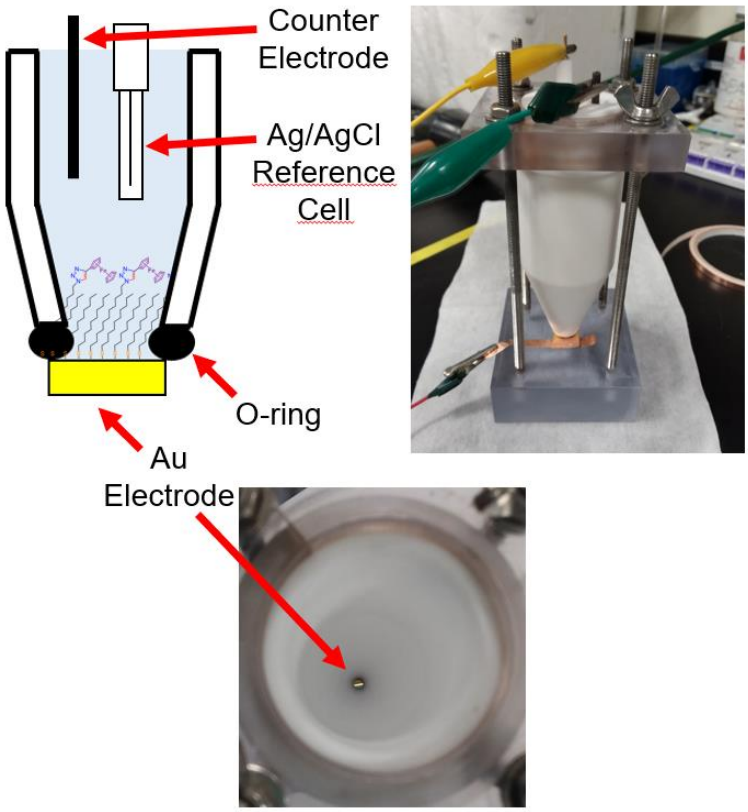

Figure 2-1 Picture of Teflon electrochemical cell used for SAM electrochemical experiments. Exposed surface area of the Au electrode is 0.153 cm^2 defined by the inner diameter of a Viton O-ring compressed by the Teflon cone cell.

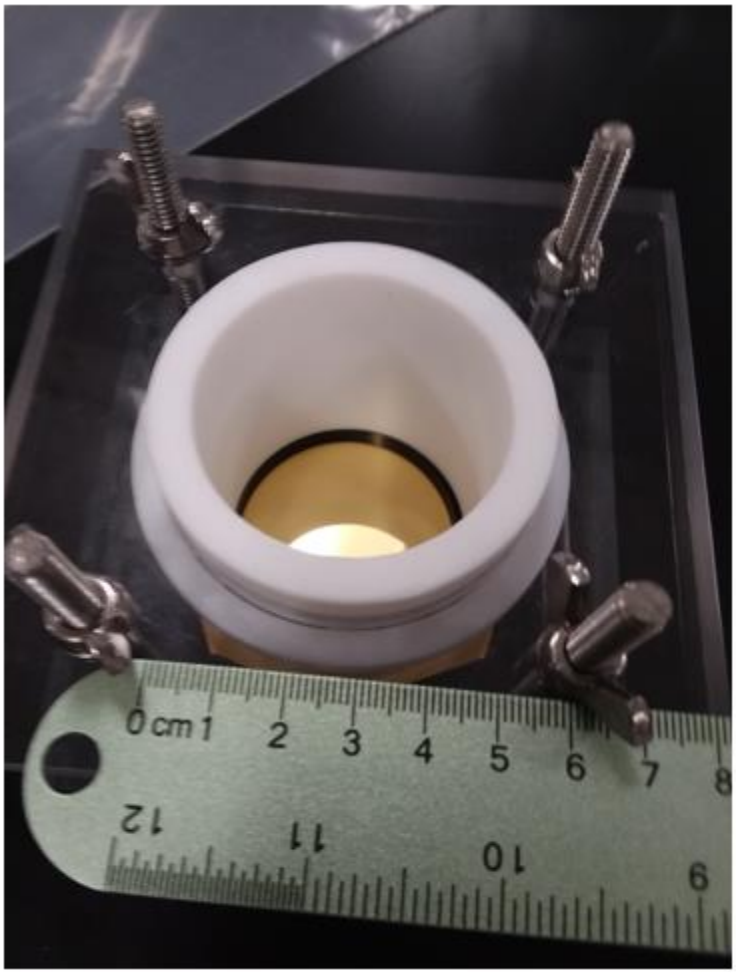

Figure 2-2 Large electrochemical cell for ICP-MS experiments. Inner diameter is 19.945 cm^2.

All electrolytes were sparged with nitrogen gas before the experiment for at least one-half an hour, and during the experiment, the solution was blanketed with nitrogen gas through one of the lid holes.

For electrochemical experiments involving ICP-MS, a larger Teflon electrochemical cell (figure 2-2) was constructed as a simple tube with an inner-diameter of ~ 5 cm, which sat on top of a Viton O-ring on the electrode surface which defined the geometric surface area of the electrode to be 19.945 cm^2. Pt wire was used as the counter-electrode, and a lab-made AgCl reference was used with a double-frit to attenuate AgCl contamination.

2.2.8 ICP-MS of Fc-SAMs and Blank SAMs

Secondary surface coverage measurement of Fc-SAMs remaining on the surface after the application of reductive desorption potentials were measured by chemically stripping the Fe in the Fc-SAMs using concentrated nitric acid and the analyzing the Fe concentration using inductively coupled plasma mass spectrometry (ICP-MS) with a PerkinElmer Nexion 2000. Due to the high presence of background Fe in most materials, all chemicals for depositing the SAMs were replaced with trace-metal grade variants when commercially available, and all glassware, graduated cylinders and electrochemical cells were cleaned with concentrated trace metal aqua regia or concentrated nitric acid rinses and soaks, before any measurements or depositions were made. Despite scrupulous cleaning of materials, background Fe could still be detected in blank samples made from “un-clicked” azido-undecanethiol SAMs etched from Au surfaces after the applied desorption potentials. To account for background Fe in every set of SAM deposition solutions, and from every electrolyte solution prepared, and every applied electrochemical

potential, an equal number of “blank” SAMs were prepared from the exact same deposition solutions used to make the Fc-SAMs, but using a click solution without ethynylferrocene. For every experimental condition (every applied potential), or new electrolyte solution that was prepared, an equal number of “blank” measurements were made for ICP-MS analysis. The Fc-SAM coverages were determined by subtracting the averaged blank Fe concentrations from the concentrations of Fe measured from etching Fc-SAM samples.

The procedure for measuring Fe in the Fc-SAMs and blank SAMs samples is as follows: Measure the Fc-SAM (or blank SAM) coverage electrochemically with CV in trace metal 0.5 M perchloric acid. Remove the electrolyte and rinse thoroughly with pure water 3x, and dump out any remaining water from the cell. Using a precleaned glass pipette, 0.5 mL of concentrated trace metal nitric acid (< 1 ppb Fe) was extracted from a precleaned graduated cylinder, and deposited onto the Au surface in the cell to etch the remaining Fc-SAM and chemically digest the Fe in the Fc for 2 minutes. During the 2-minute etch, the cell was tilted back in forth to ensure that all of the electrode surface was contacted with the concentrated nitric acid which beads up on the surface initially. At the end of 2 minutes, 0.5 mL water was pipetted into the cell to increase the volume of the etchant and completely cover the electrode surface for another 2 minutes. Using a separate precleaned pipette, the etchant was removed from the Au surface and deposited into a pre-weighed centrifuge tube. The etching procedure was repeated once more with another 0.5 mL of nitric acid and water, and the etchant was deposited into the same centrifuge tube from the first round of etching. After removing the final etch, 1 mL of water was added to soak the surface for 30 seconds, after which it was removed and added to the centrifuge tube containing the etchant, and this was repeated once more to insure quantitative transfer of all the residual nitric acid and dissolved Fe from the electrode surface to the centrifuge tube. The centrifuge tube was

then capped and massed and the pre-measured mass of the dry tube was subtracted from the total to determine the mass of the liquid contained in the tube.

Fe standards prepared for ICP-MS calibration curves were prepared from 1000 ppm commercial stock (Ricca) with concentrations of 5, 10, 25, 50, 75, 100, 200 and 500 ppb Fe in 10 mL volumes. The average Fe concentration in ppb ($\bar{x}_{blank}$) measured from at least 3 blank SAMs for a given experimental condition, was subtracted from each of the Fe concentrations (in ppb) from the Fc-SAM samples (X_{Fc}) and then the sample concentration was converted to moles per cm^2 ($\Gamma_{ICP\text{-}MS}$) using the following equation along with the solution mass and the surface area:

$$\Gamma_{ICP-MS} = \frac{(X_{Fc} - \bar{X}_{blank}) * 10^{-9}\, g\ Fe}{g_{solution}} * \frac{solution\ mass\ (g)}{55.845\ \frac{g}{mol\ Fe} * 19.945\ cm^2}$$

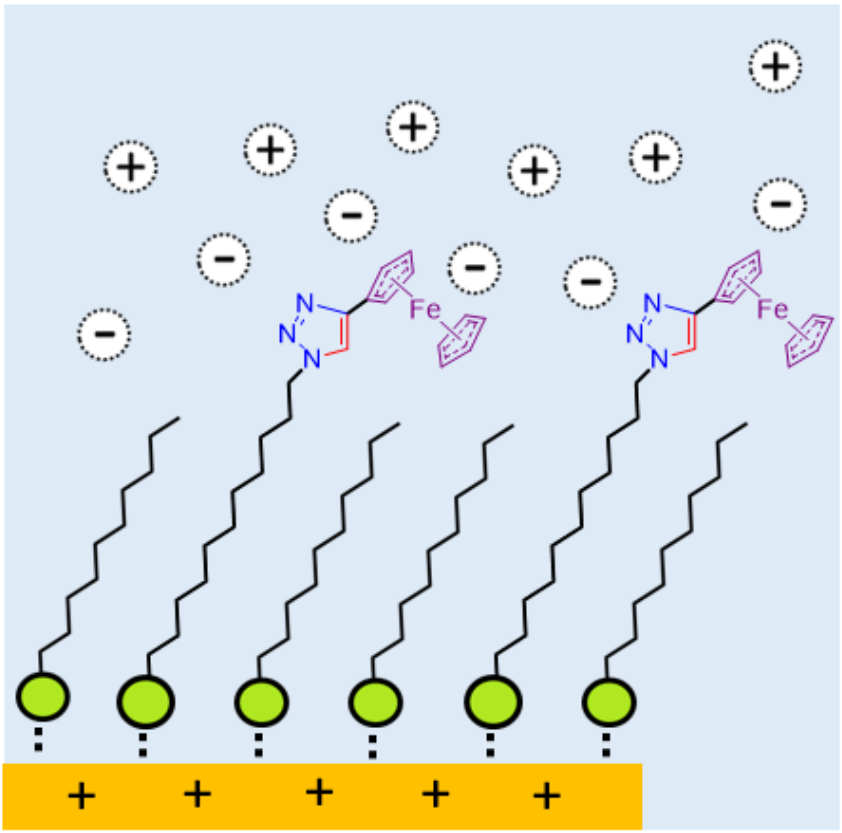

Figure 2-3 Illustrative schematic of ferrocene tethered SAM from the click reaction.

2.3 Results and Discussion

2.3.1 Cyclic Voltammetry and Chronoamperometry of Fc-SAMs

Figure 2-3 shows an illustrative schematic of the Fc-SAM mixed monolayers on a Au surface. For this work, χ is used to denote the mole fraction of azido-undecanethiol to total thiol in the deposition solution which is mixed with the decanethiol as the diluent thiol. χ = 0.75, 0.5 and 0.25 deposition solutions were prepared to form the SAMs on Au with different azide-terminated thiol coverages, and reacted with ethynylferrocene using the click reaction to form Fc-SAMs of different coverages. Estimated Fc coverages from cyclic voltammetry yielded 0.04, 0.17 and 0.31 nmol cm^{-2} for χ = 0.25, 0.5 and 0.75 respectively. Figure 2.4 shows the representative CV peaks of a pristine χ = 0.75 Fc-SAM measured in 0.5 M perchloric acid from the reversible electrochemical reduction and oxidation of the tethered Fc, depicted in equation 2.1.[13]

(2.1) $\text{Au-S-R-Fc}^{+} + e^{-} \rightleftharpoons \text{Au-S-R-Fc}$

The initial aim of this research was to correlate the loss of the Fc peak area in CV measurements after the application of potentials negative of the reductive desorption peak (E_P) commonly observed for alkanethiol SAMs when scanning the potential negative of -1 V vs AgCl in aqueous alkaline electrolytes, which is postulated to occur via the one electron reductive cleavage of the Au-S bond as in reaction 2.2.[14]

(2.2) $\text{R-S-Au} + e^{-} \rightleftarrows \text{R-S}^{-} + \text{Au}(0)$

To establish a threshold potential where the onset of the loss of Fc peak should occur, a reductive desorption CV in 0.1 M potassium hydroxide was conducted at a scan rate of 100 mV/s, starting at 0 V and scanning to -1.4 V before reversing the scan back to 0 V. Figure 2.1, right, shows the desorption CV of the $\chi = 0.75$ Fc-SAM with a desorption peak potential at ~ -1.1 V, a typical potential observed for alkyl-thiols with carbon backbones longer than 10 units, followed by the onset of large cathodic currents from the hydrogen evolution reaction.

To investigate the usefulness of Fc peaks as a probe to monitor the potential dependent stability of alkanethiol SAMs on metal surfaces as an alternative to relying on the desorption CV peaks, a set of experiments were conducted using chronoamperometry (CA), where the Fc-SAM electrode is held at a constant desorption potential for 2-minutes in 0.1 M potassium hydroxide, and the Fc peaks are measured in a separate step after the potential perturbation to measure the loss of the Fc peaks from the Au surface to the bulk electrolyte. The advantage of using a redox probe in measuring reductive desorption is the direct quantification of the SAM coverage to avoid relying on CV desorption peaks, which are not observable on all transition metal SAMs.[15,16]

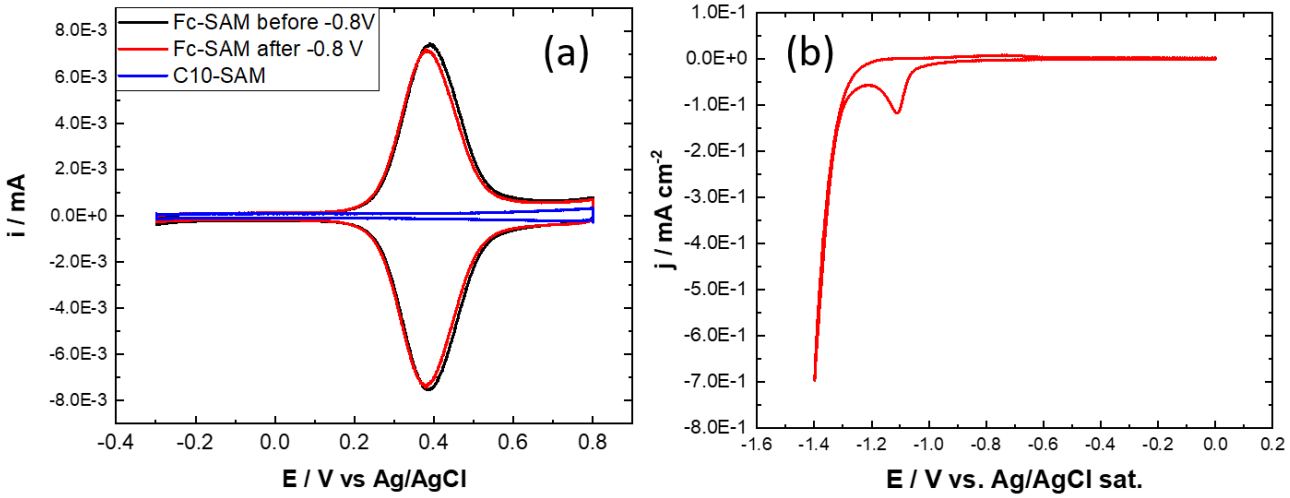

Figure 2-4 (a) CVs of χ=0.75 Fc-SAMs, and C10-SAMs, in 0.5 M perchloric acid in small cone cell. The scan rate was 0.3 V/s. The Fc-SAM CV was taken before and after exposing the Fc-SAM to -0.8 V in 0.1 M potassium hydroxide. (b) Reductive desorption CV of Fc-SAM in 0.1 M potassium hydroxide with a scan rate of 0.1 V/s.

The experiments were conducted as follows: first the pristine Fc peaks are measured in perchloric acid. (Fc peaks cannot be measured in alkaline electrolytes because the hydroxide ion attacks the oxidized Fc species, ferrocenium.[17] The reduced form ferrocene *is* stable in hydroxide solutions at negative potentials which makes Fc a stable probe for SAM desorption. Ferrocenium is stable to perchlorate anions which is why it can be measured in perchloric acid solutions.[18] The perchloric acid was removed from the cell, the cell rinsed 3x with pure water, and 0.1 M potassium hydroxide was added to the cell for the 2-minute constant applied desorption potential. After the 2-minute CA, the hydroxide solution was dumped from the cell, rinsed 3x before adding in perchloric acid once more, to measure the remaining Fc peaks. This experiment was repeated on independent samples with potentials ranging from -0.5 V to -1.5 V, spanning the range of the potentials over the desorption peak from the reductive desorption CV with the peak observed at -1.1 V.

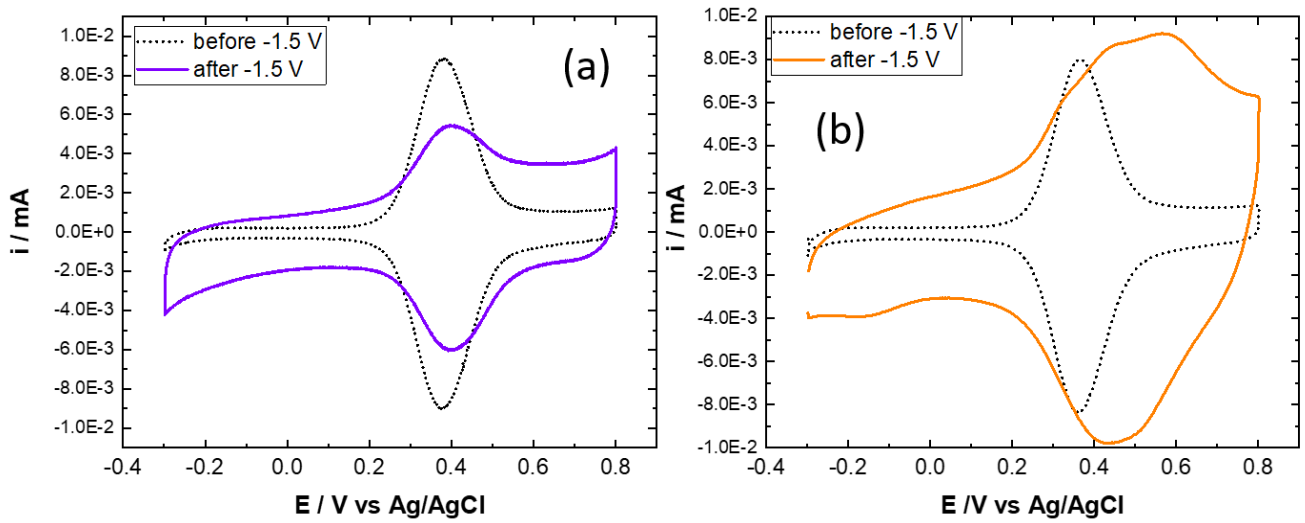

Figure 2-5. CVs from two different Fc-SAM samples (in perchloric acid, 0.3 V/s) before (a) and after (b) applying -1.5 V in hydroxide solution for 2 minutes.

At potentials positive of -1.0 V, no significant changes in the Fc peak or baseline in the CVs were observed from the application of the 2-minute CA in hydroxide. Figure 2-4 (a) shows Fc-SAM peaks before and after the application of -0.8V with no significant change in the peak area or the baseline. For Fc peaks measured after the application of potential more negative -1V where loss of the Fc-SAM was expected, a perplexing phenomenon was observed where some of the Fc peak areas did not decrease but actually appeared to increase. Figure 2-5 shows the result of two identical experiments of measuring Fc-SAM peaks before and after the application of -1.5 V. Figure 2-5 (a) shows a clear decrease in the Fc peak relative to the baseline as expected in the desorption experiment. Figure 2-5 (b) shows peaks much wider peak than before desorption, and a with no clear baseline on the positive limit of the peak. To further investigate the cause of the unusual electrochemical backgrounds, CVs in perchloric acid of bare Au and decanethiol SAM before after the application of reductive potentials were investigated.

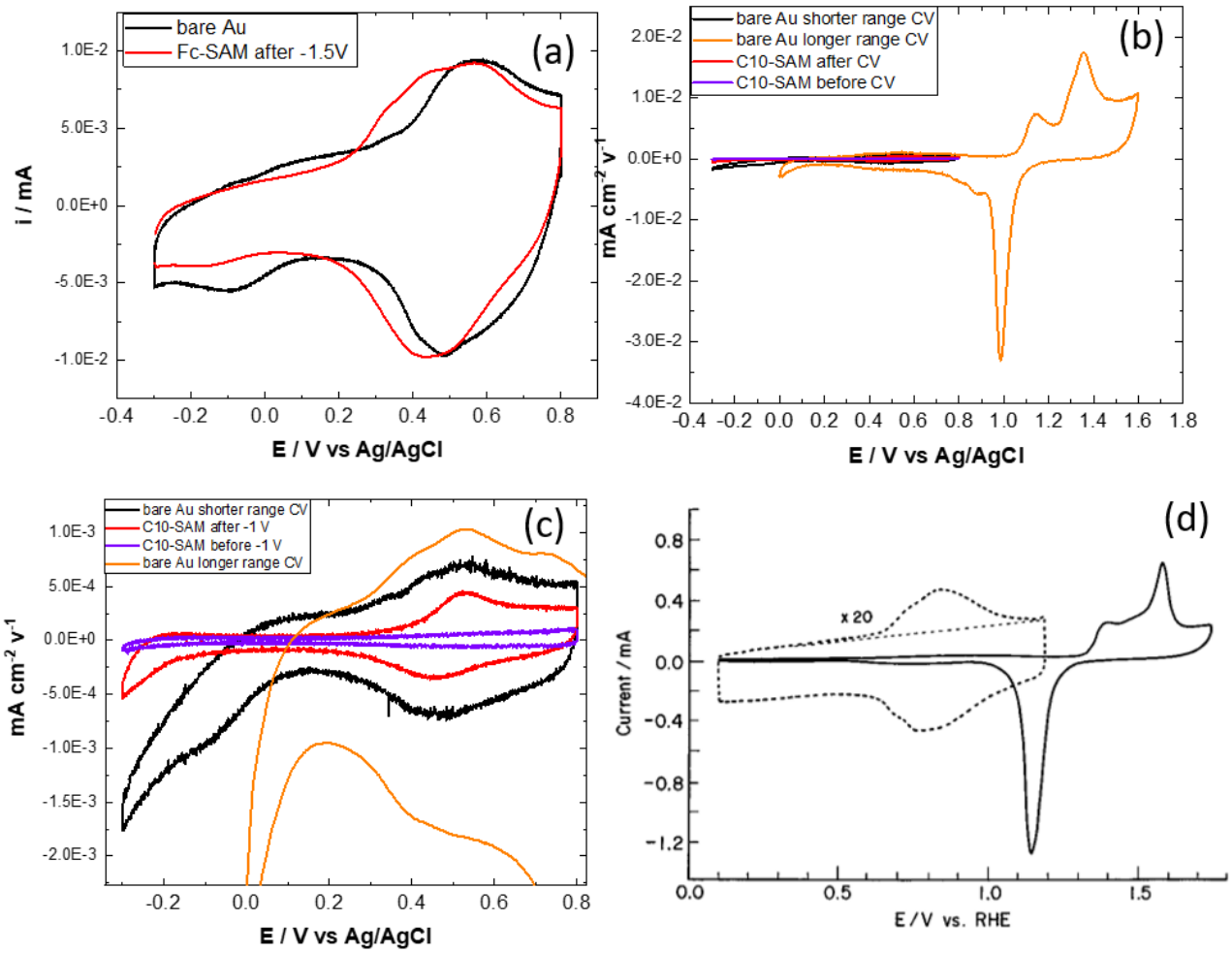

Figure 2-6 (a) CV of Fc-SAM after -1.5 V and bare Au in perchloric acid (0.3V/s scan rate). (b) CVs normalized by surface area and scan rate for bare Au (0.1 V/s) and decanethiol SAMs (0.3 V/s) before and after reductive desorption potentials in hydroxide. (c) Enlarged portion of scans from top right (b) to see peak features associated with bare Au in perchloric acid. (d) Bare Au CV in perchloric acid from literature. Bottom right is reprinted (adapted) with permission from J. Phys. Chem. 1996, 100, 25, 10664–10672. Copyright 1996 American Chemical Society.

2.3.2 CVs of Bare Au Surfaces and Reductively Desorbed Decanethiol SAMs

A CV of bare Au measured in perchloric acid is compared to a Fc-SAM surface after -1.5 V in figure 2-6 (a), which shows a distinct similarity in the broad reversible peak-like feature at potentials spanning 0.4 V to 0.8 V. To ensure the reader that this feature is indeed on a typical gold surface, figure 2-6 (b) shows another CV of bare Au but continuing the sweep positive enough (V > +1 V vs AgCl) to show the famous Au three-electron oxidation peaks, which are much larger in comparison to the peak feature observed from 0.4V to 0.8V in figure 2-6 (a) due to the greater charge passed per Au surface atom during the oxidation process. Although the peaks in figure 2-6 (a) are smaller than the Au oxidation peaks, nonetheless they are important because of their similar scale to Fc-SAM peaks and the overlap in the potential range of the Fc peak. Figure 2-6 (c) shows the same data in figure 2-6 (b), but magnified in the range where Fc-SAM peaks are observed to get a closer look at the baseline. Included in 2-6 (c) is a CV of a decanethiol SAM in perchloric acid after the application of -1 V in hydroxide solutions, which also has a peak feature in the same range as the bare Au peaks showing that these features are present on reductively perturbed decanethiol SAMs as well. Figure 2-6 (d) shows an example of the peaks on bare Au from the literature with similar observations.[19] These observations of peak shapes on bare Au and decanethiol monolayers after the application of reductive potentials insinuate that the broad features observed on reductively disordered Fc-SAMs have the same origin and represent a challenge for quantitative analysis in the regions where the Fc peak overlaps with the background peaks. What is the cause of the peak features on bare Au and the reductively disordered decanethiol SAMs?

The peak-shaped current response of bare Au in electrolytes has been attributed to the potential-dependent specific adsorption of the electrolyte anion (or cation), with charge transfer between the Au surface and the adsorbed ion. This phenomena is controversial and complex, with peak shifts in potential that correlates to the crystallinity of the surface plane, the anion identity, the electrolyte concentration, and chloride contamination.[20-28] Potential dependent perchlorate adsorption has been detected on Au surfaces in the same potential range presented here using surface selective vibrational spectroscopy.[28] In-situ surface selective spectroscopic measurement of potential dependent perchlorate vibrational modes has been used to model the CV peaks on bare Au with limited success due to the poor understanding of the physical process. [28] The takeaway from this information is that the cause of these features is known and measurable, but the current response is distinctly difficult to model due to limitations in the complexity of electrochemical metal surfaces.

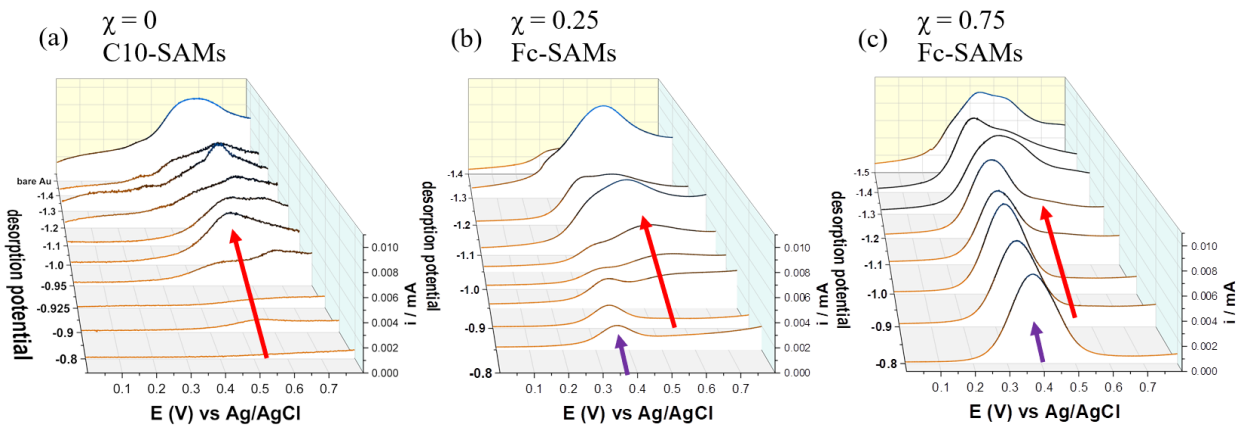

Figure 2-7 (a) CVs of C10-SAMs and (b), (c) Fc-SAMs taken in 0.5 M perchloric acid, 0.3 V/s, after the application of the desorption potentials (axis on left of waterfall plot) applied during chronoamperometry in 0.1 M potassium hydroxide. (a) C10-SAMs. (b) χ=0.25 Fc-SAMs. (c) χ=0.75 Fc-SAMs

To make the connection more concrete between reductively disordered alkanethiol SAMs and Fc-SAMs, figure 2-7 (a) compares a series of anodic CV sweeps of unfunctionalized decanethiol SAMs in perchloric acid after the application of 2-minute reduction potentials in hydroxide, to identical CV measurements of the Fc peaks of $\chi = 0.25$ and 0.75 Fc-SAMs CV after the same reductive potentials in hydroxide, which are shown in figure 2-7 (b) and (c) respectively. In figure 2-7 (a), CVs after applying potentials positive of -0.9 V, the decanethiol SAMs (C10-SAMs) look ideal with a flat double-layer charging baseline. As the applied potential is made more negative than -0.9 V corresponding to CV scans toward the back of the plot in 2-7 (a), the baselines become distorted and non-linear, much like the CV backgrounds on bare Au. For $\chi = 0.25$ Fc-SAMs in figure 2-7 (b), similar features are observed after the application of potentials more negative than -0.9 V which produced background peak features in the baseline that overtake the magnitude of the original Fc peaks. For $\chi = 0.75$ Fc-SAMs, which begin with higher Fc coverages than $\chi = 0.25$ Fc-SAMs, the Fc peak remains distinctly visible even after the application of more negative potentials, but the baseline blends with the Fc peak making it difficult to discern background feature from the Fc peak. The most pertinent question after examining this data is how does a non-ideal baseline affect the accuracy and precision of the Fc peak area analysis considering that baseline subtraction is an important step in measuring electrochemical peak areas?

2.3.3 Non-ideal CV Baselines Effect on Quantitative Analysis, the Bias from Choosing the Interpolation Range Using Linear Interpolation Baseline Correction, and Backfilling Partially Desorbed Fc-SAMs with Decanethiol

The most common form of CV baseline correction for quantitative peak area analysis is linear interpolation, where a straight line drawn underneath the peak is constructed to approximate data points outside of the foot of each side of the peak, and then subtracted from the total current signal. For pristine Fc-SAMs this can be justified by examining figure 2-4 (a) which shows an unfunctionalized decanethiol SAM baseline in a CV plotted with the Fc-SAM CV which shows that in the absence of the Fc peak, the baseline is flat. The flat current of a decanethiol SAM in a CV is linearly dependent on the scan rate, often modeled as the capacitive charging of an RC circuit depicted in figure 2-8 (a), as a dielectric material filling the space between the capacitor plates.[1,14] In the case of SAMs, the carbon backbone of the SAM acts as a dielectric between the charged Au electrode and the charge in the electric double-layer on the electrolyte side of the SAM. The dielectric constant, *k* in equation 2.4, is assigned to the carbon unit of the alkyl backbone with thickness *d*, which modulates the CV charging current and the total charge passed as capacitance, C_{DL} (farads or charge per volt) which scales with surface area. The constant ε is the permittivity constant. C_{DL} of alkanethiol SAMs decreases with increasing length of alkane backbone *d* in the idealized model. The length of the SAM can be detected by the decrease in the double-layer current, i_{DL} in equation 2.3 and in figure 2.4 (a) with increasing *n* carbon units in the SAM backbone or decreasing scan rate in a CV. The double-layer current, i_{DL}, relates to the capacitance, C_{DL} and the scan rate, *v*, in equation 2.3 along with the solution resistance R_{sol}.

(2.3) $$i_{DL} = vC_{DL}[1 - \exp\left(\frac{-t}{R_{Sol}C_{DL}}\right)]$$

(2.4) $$C_{DL} = \frac{k\varepsilon A}{d}$$, (ideal parallel plate capacitor equation)

Reductive desorption of alkanethiol SAMs disrupt the packing of the alkyl-backbones and exposes the surface to interactions with the electrolyte which increases the capacitive response in a CV.[29] The capacitive response has been used to model pinhole defects in SAMs, and as a detection method for estimating the reductive desorption potential on Pd.[29]

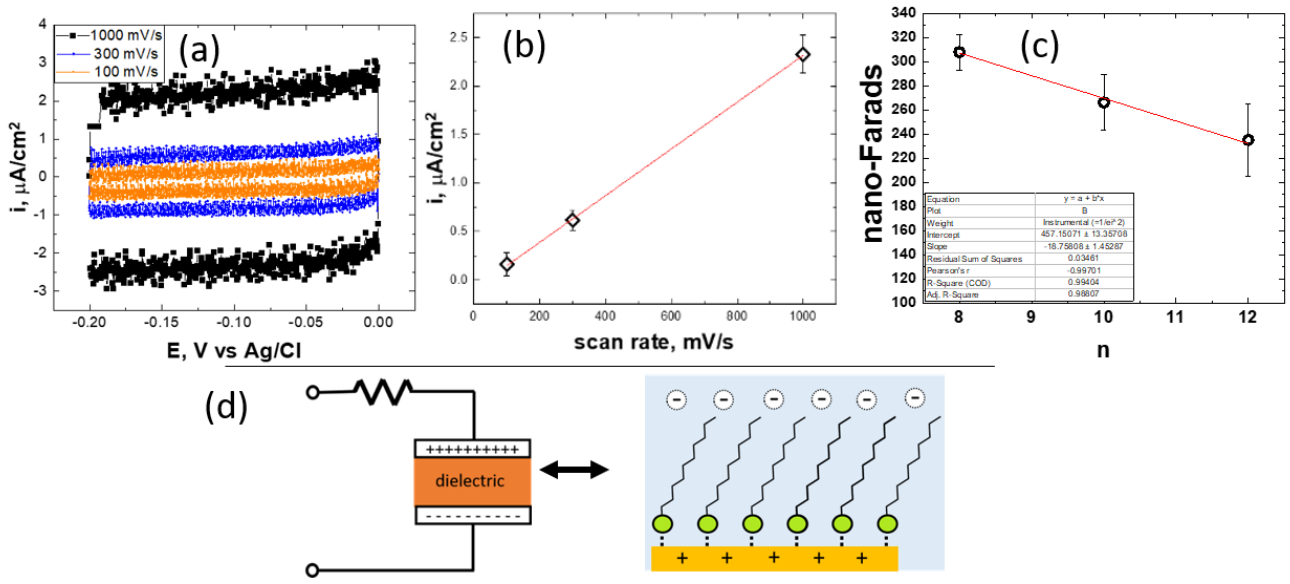

Figure 2-8 (a) CV scans at different scan rate of a C10-SAM in 0.5 M perchloric acid. (b) Linear relationship between average currents from the C10-SAM CV scans vs the scan rate plotted with a linear best fit to extract the capacitance from the slope. (c) Capacitance vs n carbon units in alkanethiol SAM backbone showing linear dependence on SAM thickness consistent with parallel plate capacitor model with a dielectric. (d) RC circuit parallel plate capacitor next to a SAM schematic to visualize the SAM as a parallel plate capacitor dielectric material sandwiched between the charge on the Au surface and the electrolyte counter-charge.

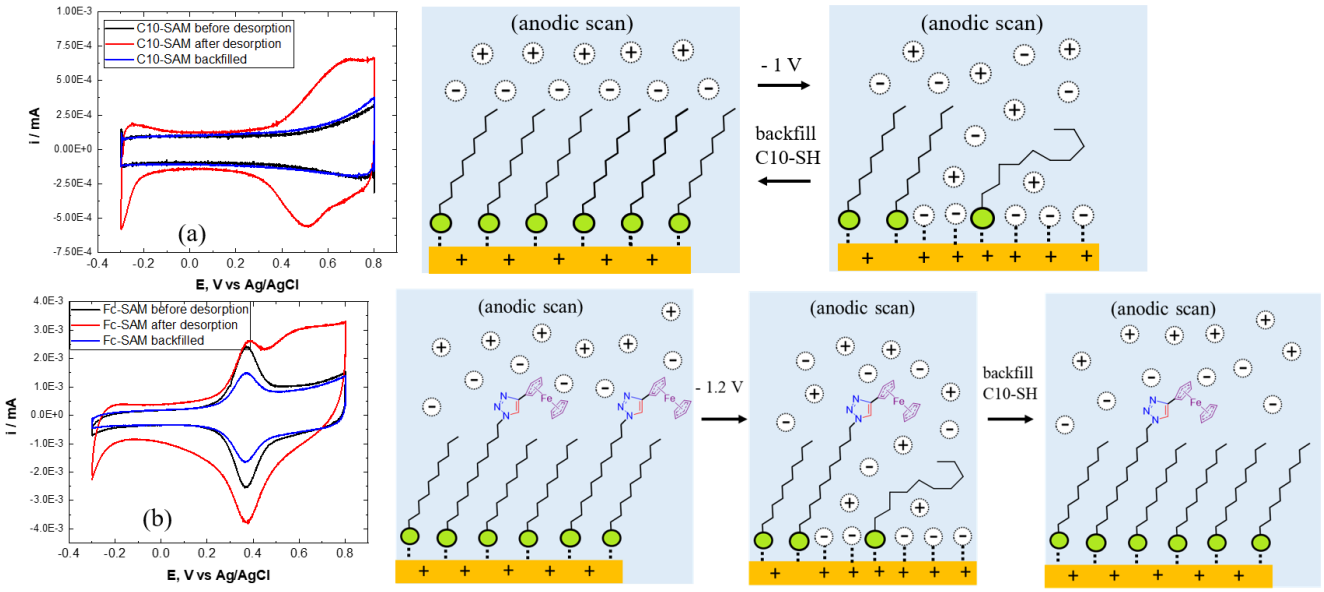

Figure 2-9 CVs showing the effect of backfilling reductively disordered SAMs on the CV response. Each CV shows a scan of the pristine SAM in perchloric acid before (black) and after (red) partial desorption in hydroxide which creates defects in the SAM and non-ideal baselines. A final CV was taken after backfilling with 10 mM decanethiol for 5 minutes, restoring the baselines of the CV (blue).

The defects introduced from the reductive desorption of SAMs can be reversed in a backfilling method where the SAM surface is reintroduced to a thiol deposition solution. Figure 2-9 depicts the backfilling process graphically along with CV measurements after reductively desorption of a C10-SAM and Fc-SAM, and after backfilling which "heals" the defects and restores the ideal CV baseline. The backfilling process was applied by removing perchloric acid from the cell after the CV of the disordered SAM was taken, rinsing with water, and adding enough 10 mM decanethiol (in ethanol) to cover the Au surface for 5-minutes, after which the thiol solution was removed from cell, rinsed thoroughly with ethanol and then water, and then adding perchloric acid again for more CVs measurements. The backfilling procedure is useful because it restores the ideal baseline, making the peak easy to analyze once again, although at the cost of losing some of the Fc-thiols which are exchanged with decanethiol during the backfilling process. The exchange is a well-known process and has been used to remove loosely-bound physisorbed thiols to create better packed SAMs or to isolate and redistribute redox-active thiols in mixed SAM systems.[30] The goal of this work was not to measure Fc-SAM coverages after an exchange process but to measure the remaining Fc-thiols after a reductive perturbation. This means that the backfilling can help bound the peak area analysis, but it does not solve the problem of non-ideal background correction by itself. Thus, the problem focus is routed back towards the treatment of the data using linear interpolation for background correction. How robust is linear interpolation for background correction for non-ideal baselines in CVs?

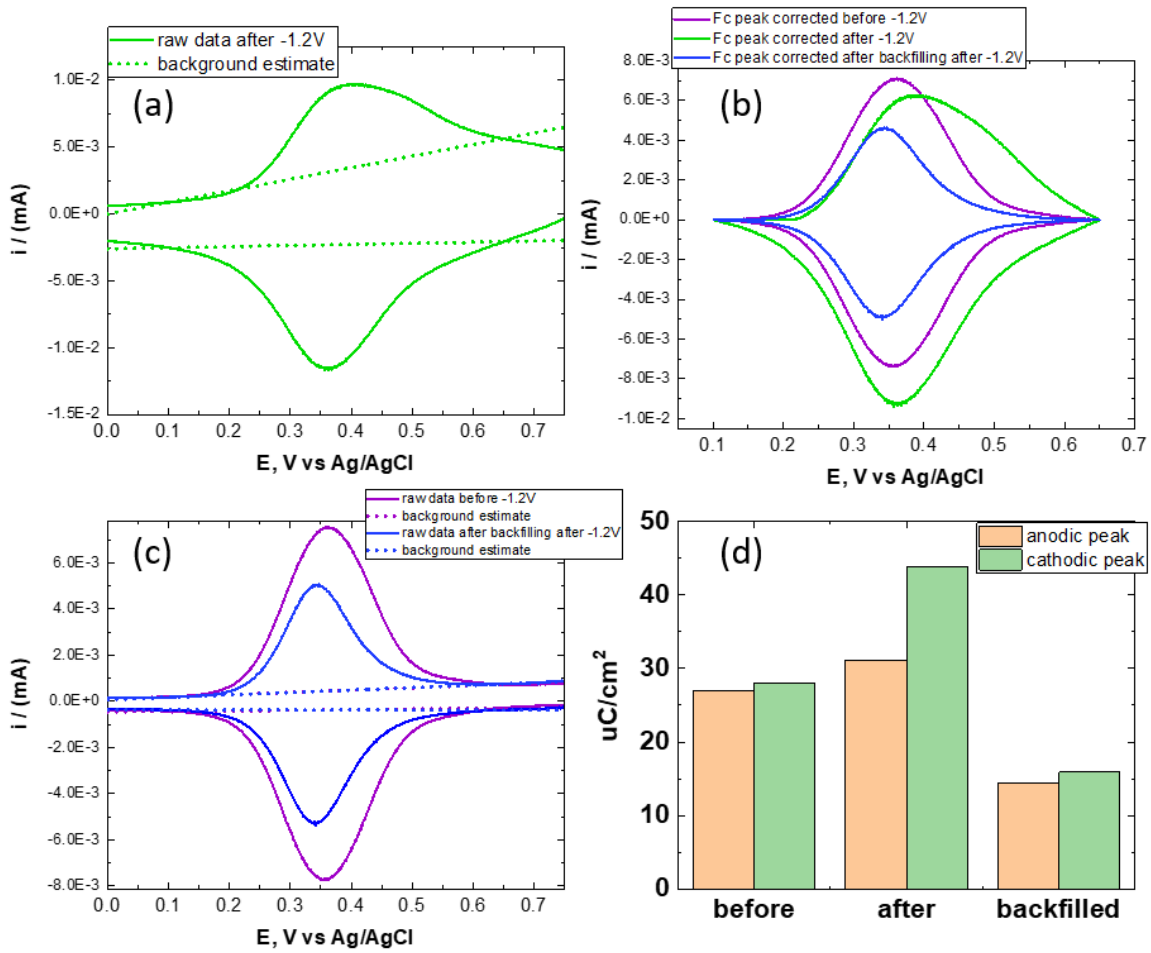

Figure 2-10 (a) Fc-SAM CV in perchloric acid after applying -1.2 V in potassium hydroxide for 2 minutes. (b) Background corrected CVs of Fc-peaks of Fc-SAM before, and after -1.2V, and backfilled, using linear interpolation with an interpolation range of 0.1 V to 0.65 V. (c) Raw CVs of the same Fc-SAM as in top left, but before the reductive perturbation, and after, but backfilled with decanethiol. (d) Peak areas extracted from the CV after background correction using linear interpolation.

Using linear interpolation to estimate the CV baseline of a reductively disordered Fc-SAM sometimes measures a Fc peak area larger than the peak area measured before the reductive perturbation. As no new source of Fc-thiols are present in any of the electrolytes used for CV measurement, and the electrode surface area was held fixed by the compressed O-ring in the Teflon cone cell, the extra charge must be from the increase in the background charges which was demonstrated to occur (figure 2-9) with SAMs after reductive desorption. Figure 2-10 © shows a pristine Fc-SAM CV in perchloric acid before the application of -1.2 V in hydroxide solution. The baseline in the 'before' scan (blue dotted line) was constructed using linear interpolation from data points at 0.1 V and 0.65 V to ensure that the foot of the Fc peak was excluded from the baseline, which approximates the real data points reasonably well outside of the assumed peak limits. Using the same interpolation limits (0.1 V and 0.65 V) on the same Fc-SAM after -1.2 V (figure 2-10 (a)) generates a baseline with a new intercept and slope because the current magnitude has risen at all points from the increase in the charging current, and it should be noted that the current at the more positive potential limits of the peak have grown larger than at currents at the potentials negative with respect to the peak. The line from linear interpolation after -1.2 V diverges from the curve at the extreme ends of the CV because there is no straight line that capture the different slopes on opposite sides of the peak. Furthermore, the difference in measurement between the anodic peak area and cathodic peak area is more extreme in the 'after' measurement, suggesting that the data is distorted by the additional charging currents. The cathodic charge has risen to nearly 180% of the initial measured charge before desorption. The reductive disordering process may have created new Fc domains, and therefore a broadening or splitting of the Fc peak would be expected, but this should not create additional

charges that are nearly double the initial charge. This information suggests that linear interpolation does not separate new background surface charges from the Fc peak response in the CVs after desorption. More generally, using primitive background corrections in complex peak area measurements will undoubtedly introduce inaccuracies and bias to quantitative analysis.

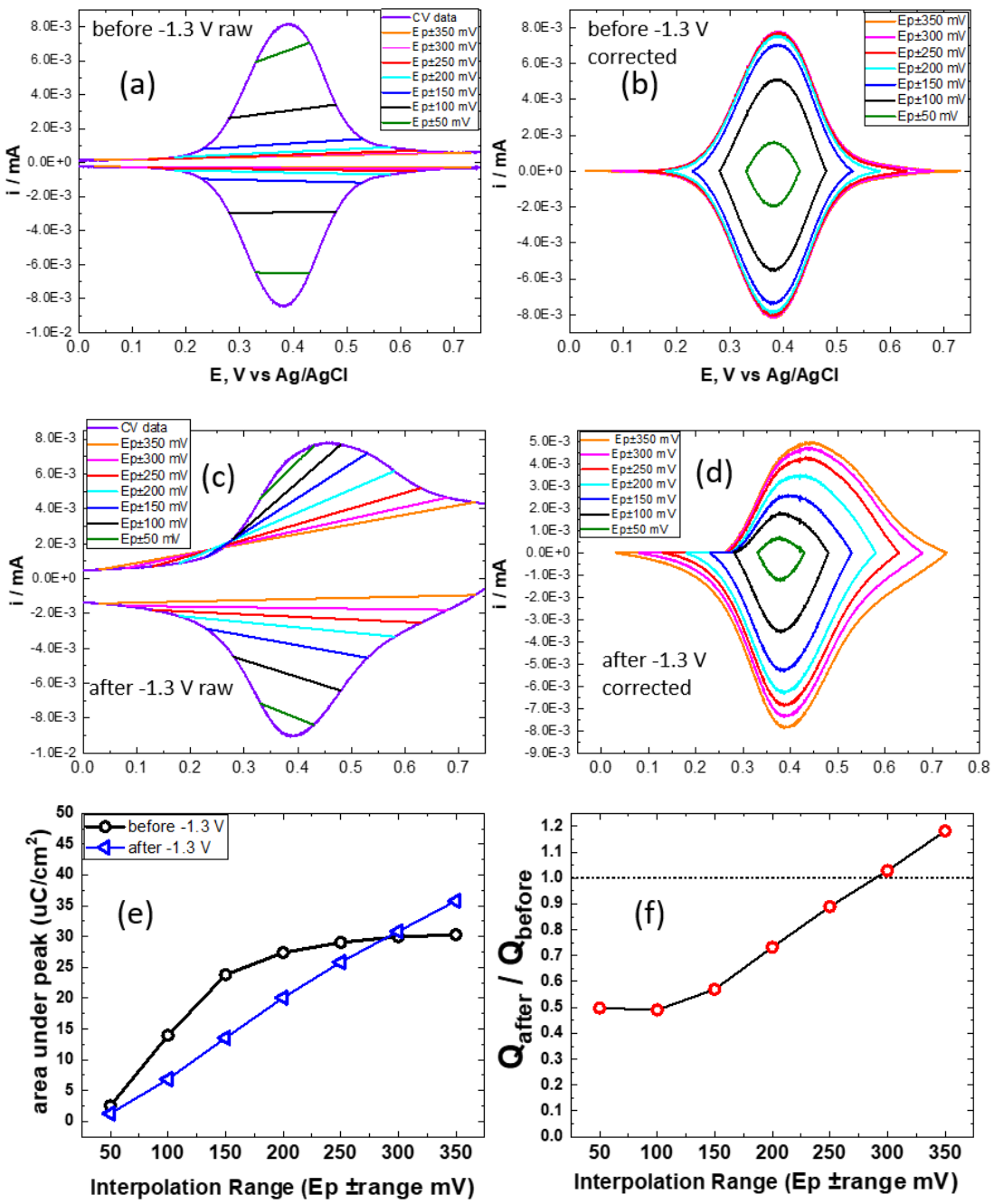

Figure 2-11 The effect of the choice of the range for linear interpolation on the measurement of the Fc peak area before and after reductive desorption. (a) Raw CV of pristine Fc-SAM before the application of -1.3V and the baselines (colored straight lines) resulting from different interpolation ranges indicated in legend. (b) Baseline corrected before peaks resulting from different interpolation ranges. (c) Raw CV of same Fc-SAM after -1.3 V and the baselines resulting from different interpolation ranges. (d) The resulting background corrected Fc peak of Fc-SAM after -1.3 V resulting from different interpolation ranges. (e) CV peak areas in (b) and (d) resulting from the different baselines from changing the interpolation range. (f) Resulting ratio of Fc peak charges after/before applying -1.3 V to examine the effect of linear interpolation range on the normalized peak area measurement.

The question of how linear interpolation biases the peak area measurement is demonstrated by considering how the *choice* of the interpolation range would affect the measurement of the peak area in CVs of Fc-SAMs with non-ideal baselines. The interpolation range will be defined as the assumed limits of the Fc peak in a CV used to construct the linear baseline approximation, described relative to the Fc peak maxima ($E_P \sim 0.38$ V). For example, the interpolation range used to construct the baselines in figure 2-10 are the data points at 0.1 V and 0.65 V, or more succinctly $E_P \mp 280$ mV, where E_P is the Fc peak maxima at 0.38 V. Figure 2-11 shows graphically the effect of using different interpolation ranges to construct baselines on a Fc-SAM after the application of -1.3 V. The interpolation ranges chosen span from $E_P \mp 350$ mV to $E_P \mp 50$ mV, which are color-coded in the legends of figure 2-11. The resulting peak shapes in figure 2-11 (d) and the peak areas in figure 2-11 (e) show clearly that the choice of the interpolation range changes the peak area measurement drastically when non-ideal baselines are present in the data. The shape of the Fc peak after each of the baseline corrections is shown in figure 2-11 (b) and (d) for the Fc-SAM before and after -1.3 V to corroborate the peak area measurements. The before peaks appear less susceptible to bias over the ranges where the linear interpolation does not cut into the peak which means that for ideal Fc-SAMs, the interpolation range is a trivial issue. However, the relative measurement of the ratio of peak areas charges normalized by the before coverage (Q_{AFTER}/Q_{BEFORE}) are shown in figure 2-11(f), which shows that the ratio is not immune to the choice of linear interpolation, again highlighting the bias in the interpolation range decision of the analyst analyzing the data.

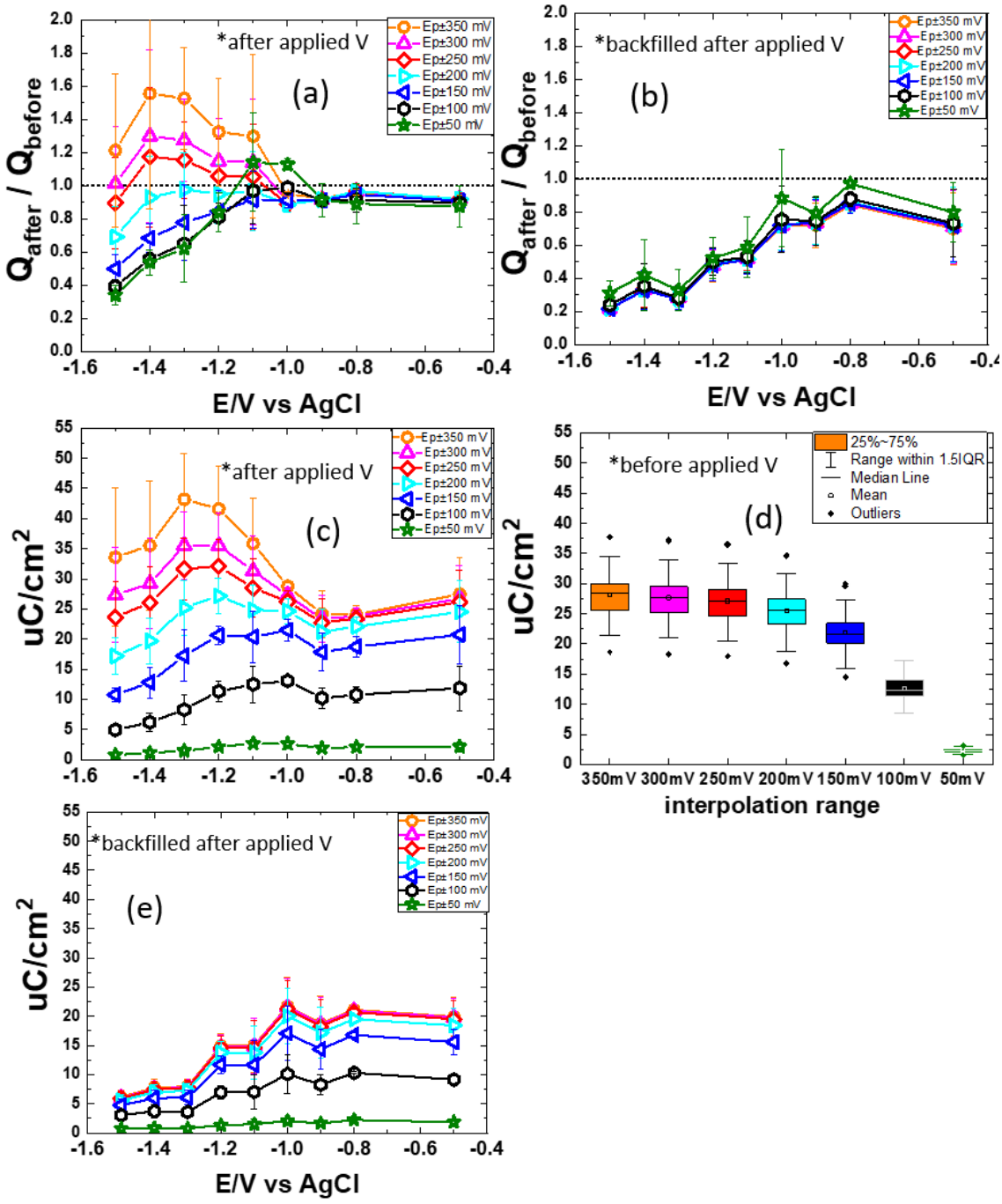

Figure 2-12 The effect of the choice of interpolation range and how it biases the Fc peak values and normalized coverages resulting from non-ideal baselines from disordering at reductive potentials. (a) Normalized Fc peak areas (normalized by peak area before reductive potential applied) as function of applied potential (2 minutes in 0.1 M potassium hydroxide) using different interpolation ranges to background correct Fc-SAM CVs in perchloric acid. (b) Normalized Fc peak areas after backfilling with decanethiol to restore ideal baseline vs interpolation range. (c) Fc peak area values after applied potentials in hydroxide (same samples as top left but not normalized) with different interpolation ranges. (d) Fc peak areas of pristine Fc-SAMs (before any applied voltage) vs choice of interpolation range. (e) Backfilled Fc peak areas.

If the peak areas are more sensitive to the choice of the interpolation range with non-ideal backgrounds from reductive desorption, then this sensitivity can be exploited to show the potentials where the Fc-SAMs are unstable. Figure 2-12 shows the results of Fc peak areas from triplicate measurements after the application of potentials where the SAMs are reductively unstable (applied V < -1V vs AgCl). Figure 2-12 shows that the bias from the choice of interpolation range causes the range of peak areas to explode at potentials < -1V for both the normalized Fc peak areas Q_{AFTER}/Q_{BEFORE} in figure 2-12 (a) and the raw Fc peak areas in figure 2-12 (c). In contrast, Fc-SAMs with ideal baselines like the Fc-SAM before applying reductive potentials, and the backfilled Fc-SAMs, the ratio of Q_{AFTER}/Q_{BEFORE} is relatively independent of the applied potential as shown in figure 2-12 (b) and the raw peak areas have less variance in the before and backfilled peaks in 2-12 (d) and (e) compared to the raw peak areas of the after measurements made before backfilling. The key takeaway is that there is strong bias in the choice of the interpolation range, but there is useful information imbedded in the spread of peak area values as a function of applied potential using linear interpolation, because the spread correlates non-ideal baselines produced from applied potentials consistent with the well-established notion of SAM reductive instability at potentials < -1V. Although this information is useful, the question of whether this data can be used for quantitative measurements remains pertinent. In light of the uncertainty presented here, a new set of Fc-SAM reductive desorption experiments were conducted using ICP-MS as a secondary analysis technique to compare new baselining techniques that incorporate LASSO regression and empirical

backgrounds generated from reductively disordered "blank" unclick azido-undecanethiol SAMs.

2.3.4 Comparing ICP-MS Coverage Measurements of Fc-SAM after Reductive Desorption to Electrochemical Coverage Results Using Novel Machine Learning Baseline Techniques and Linear Interpolation

To investigate the bias caused by baselining the CV measurements, a set of Fc-SAMs were measured using CVs after reductive potentials using the same conditions as above, and then chemically stripped from the Au surface using 1 mL of concentrated nitric acid, followed by 2 x 1 mL water rinses to ensure quantitative transfer of Fe into a centrifuge tube, and the subsequent Fe concentration was measured using ICP-MS for constructing an independent estimate of the remaining Fc-SAM. To reach a sensible level of sensitivity for ICP-MS, Au-wafer electrodes were prepared with a large enough diameter to fit a 19.945 cm^2 Viton O-ring to define the geometric surface area of the electrode in a compression-type tube cell. By maximizing the surface area and minimizing the final volume (~ 4 mL), the measured Fe ppb range fell within 20 to 60 ppb range. The Fe concentrations measured from Fc-SAMs were background corrected by preparing identical 'blank' SAMs from the same thiol deposition solutions and click solutions, except the ethynylferrocene was omitted from the 'blank' click solutions. The glassware, pipettes, graduated cylinders, O-rings, and the Teflon electrochemical cell were pre-cleaned in concentrated aqua regia before and between each sample. For each applied potential, triplicate or more 'blank' SAMs were measured and etched for Fe backgrounding, and a large enough batch of trace-metal electrolyte was prepared so all of the blanks and Fc-SAMs at a given potential were all exposed to the same batch of electrolyte.

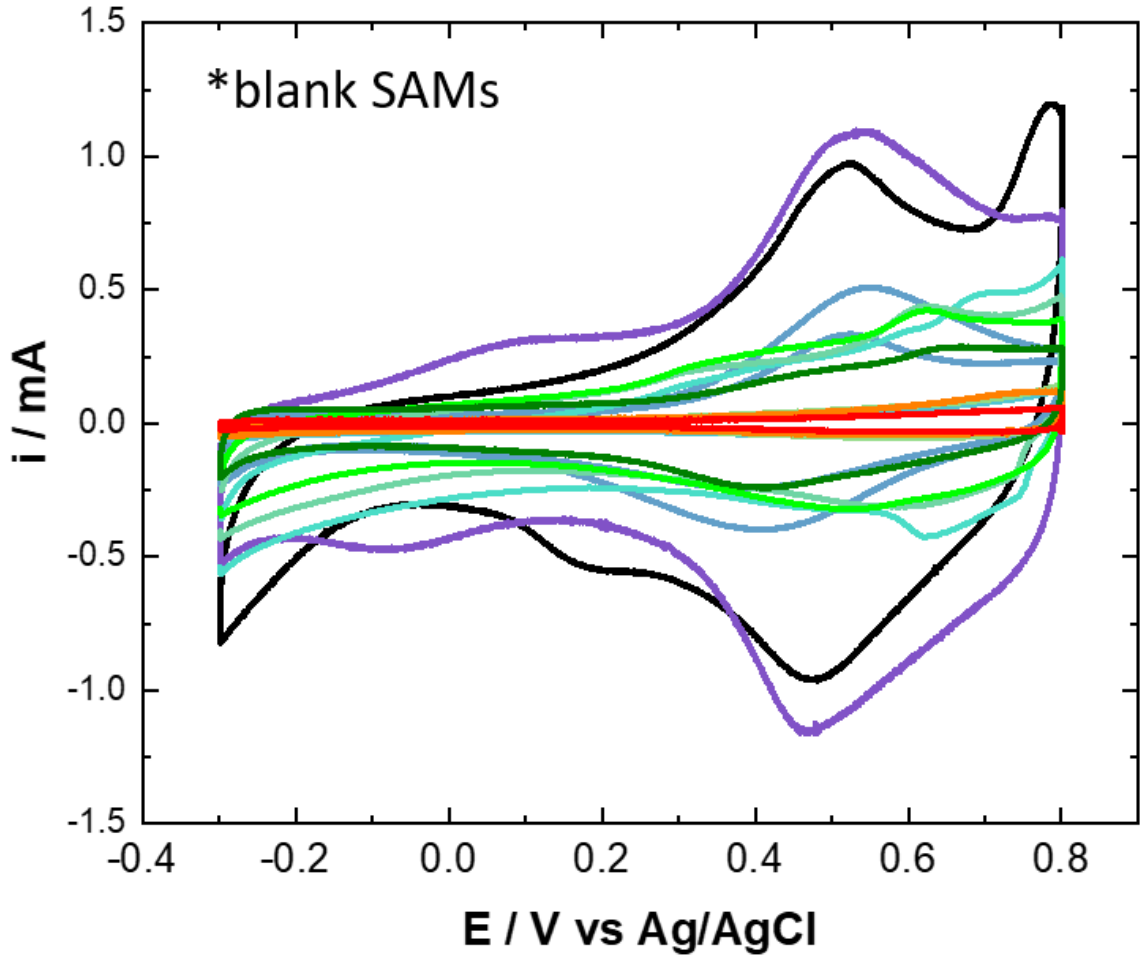

Figure 2-13 CV of unclicked azido-undecanethiol SAMs after the application of reductive potentials in trace metal 0.1 M potassium hydroxide, measured in trace metal perchloric acid (0.5 M). 0.3 V/s scan rate. 19.945 cm^2surface area. These scans were used as the basis set for fitting baselines using LASSO regression.

The average coverage of the Fc-SAMs prepared on the large area (19.945 cm^2) electrodes is 1.9 ∓ 0.6 $x10^{-10}$ mol cm^{-2} using cyclic voltammetry and linear interpolation before the application of reductive potentials. For blank SAMs, peak-shaped features at potentials positive of the Fc peak (~ 0.5 V to ~ 0.65 V) were observed in the Fc peak CV in the trace-metal perchloric acid after applying potentials < -1 V similar to the features observed on the smaller scale electrodes. Figure 2-13 shows a subset of CVs in perchloric acid of blank SAMs after the application of reductive potentials along with pristine SAMs for comparison. Figure 2-14 left, shows a close-up of a reductively disordered Fc-SAM after the application of -1.5 V on a large-scale electrode for ICP-MS measurement, which has similar background features as the blanks, in addition to the Fc-peak at ~0.38 V. Included in the figure are two sets of baseline approximations using linear interpolation with different interpolation ranges of E_P ∓ 0.35 V and E_P ∓ 0.20 V. Again, the 'baselines' are not equal on either side of the remaining Fc-peak, and changing the interpolation range decides whether the new features adjacent to the Fc peak are included in the peak area measurement or no. Figure 2-14 right, shows the result of the ICP-MS measurement compared to the results from linear interpolation baseline correction using different interpolation ranges. A clear trend emerges with an increasing difference between the ICP-MS measurement and CV measurement with decreasing potentials when using linear interpolation baseline correction with larger interpolation ranges.

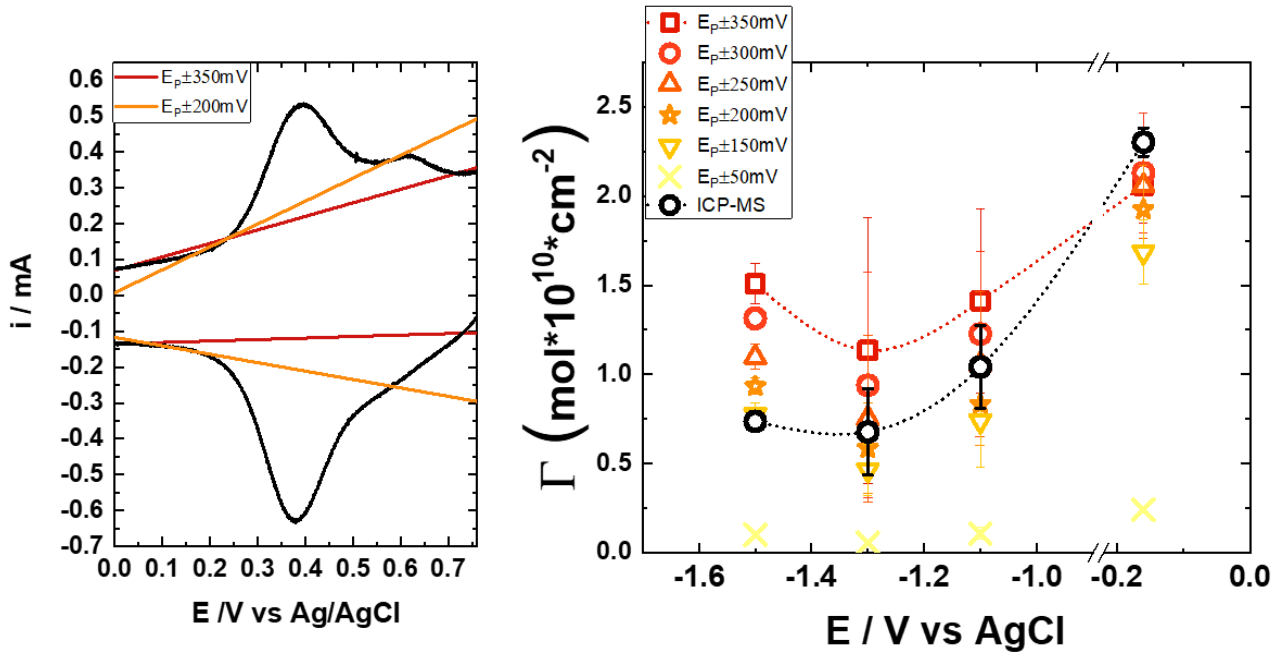

Figure 2-14 Left: CV of Fc-SAM after -1.5 V on 19.945 cm^2 electrode used for ICP-MS experiments. Right: Coverage measurements as a result of ICP-MS and CV measurements using linear interpolation. Different coverage measurements are shown for interpolation ranges showing an increasing distance from the ICP-MS data at more negative potentials for wider interpolation ranges which include more of the curve as the Fc peak.

To see if the background features in the blank SAMs can be used as an empirical baseline fit to the Fc-SAM CV data, several iterations of a machine learning model using LASSO regression and non-linear least-squares were deployed to fit the CV data and tested against coverage measurements from ICP-MS and linear interpolation. The motivations to use these new models is to improve the accuracy of the peak area measurement and avoid the bias introduced when arbitrarily choosing an interpolation range in non-ideal CV baselines. The following is a brief description of each model, and a more in-depth description of each model is found further bellow after the ICP-MS results.

The models use LASSO regression to construct a weighted average of the empirical 'blank' SAM CV data to match the baseline features in the Fc-SAM data to see if they can be used as more accurate baseline approximation. The model labeled 'LASSO+Fc Peak Fit' in figure 2-15, segments the Fc-SAM CV data into discrete sections that don't contain the Fc peak (presumably) and constructs a weighted average of the 'blank' SAM CV curves to approximate the Fc-SAM CV baseline. Each section generates a unique baseline estimate which is then fed into non-linear least squares fitting that includes a parametric equation for the Fc-peak, and a linear weight for each of the baseline solutions. The second LASSO model called 'unmasked LASSO' in figure 2-15 is purely empirical, where it weights the Fc peak extracted from the data before reductive potentials are applied, in a linear combination with the 'blank' baselines to fit the Fc-SAM CV after desorption. A third model was also constructed using pure peak fitting of the CV data with non-linear least squares and a parametric equation for the background peaks in addition to the Fc peak. A similar strategy to analyze Pt surface electrochemistry.[31]

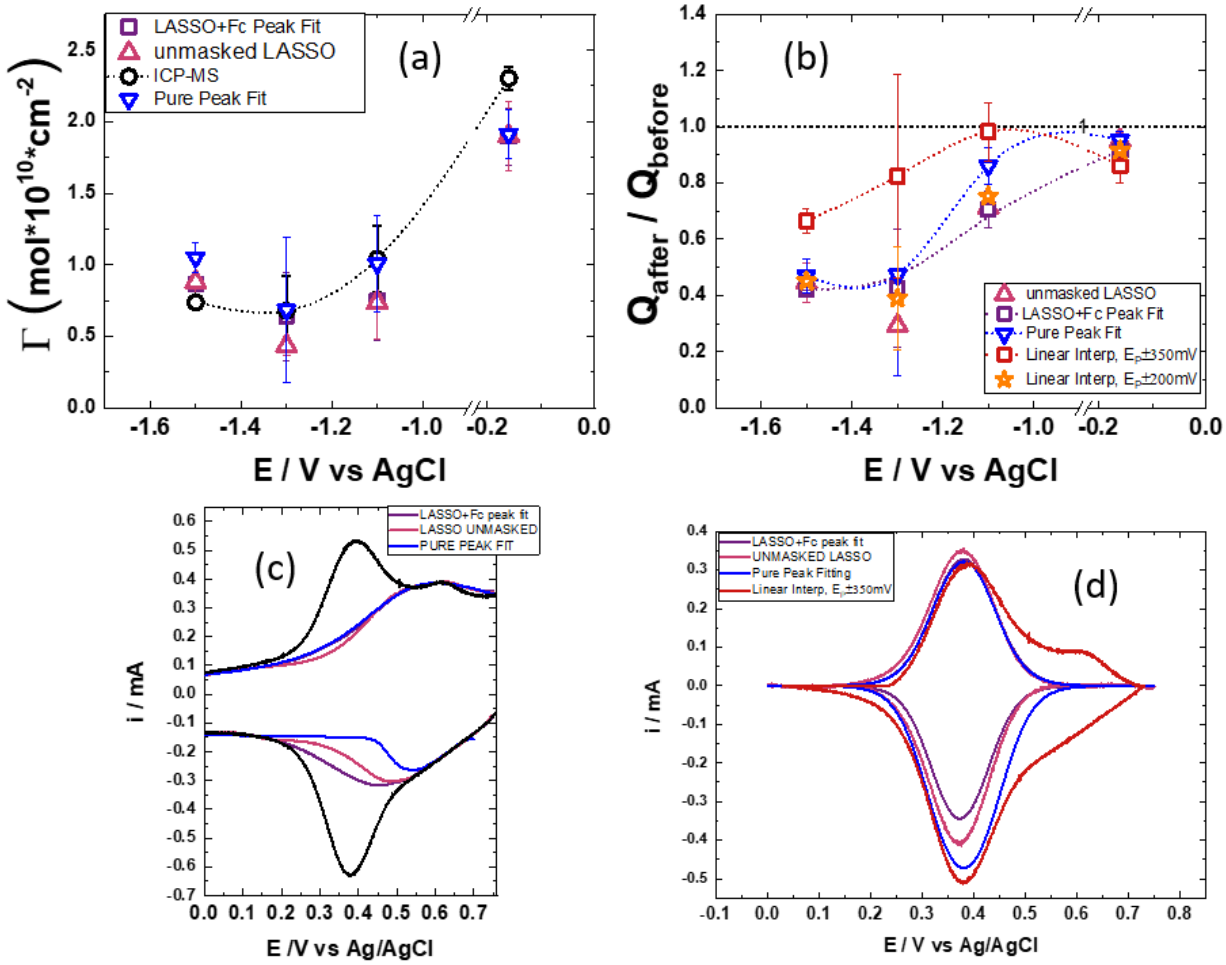

Figure 2-15 (a) Coverage of Fc-SAMs after the application of reductive potentials in hydroxide measured with cyclic voltammetry peaks baselined using machine learning models with empirical 'blank' baselines after desorption or pure peak fitting with non-linear least squares. ICP-MS measurement of the Fc coverage is included as a benchmark. (b) Normalized coverage using two different linear interpolation range on the Fc-SAMs used in the ICP-MS experiments, along with the normalized coverage from the machine learning models. (c) Fc-SAM CV after -1.1 V for the ICP-MS experiment showing the baseline approximation from the fitting models. (d) Baseline subtracted Fc-peaks from each of the baseline models from data in bottom left.

Figure 2-15 bottom left shows the baseline approximations (colored curves) from the LASSO based models and pure peak fitting, which are curved and peak shaped as they constructed from a weighted average of the C10-SAM peak shaped baselines after reductive desorption, or fitted with a pure peak fitting model which the assumes that extra peaks are background peaks. The cathodic and the anodic peaks were analyzed separately and averaged for the peak area estimate. The baseline subtracted peaks are shown compared to the results from linear interpolation in the bottom right of 2-15. Figure 2-15 top left shows that the using empirical baselines in the machine learning model biases the Fc coverage lower than most of linear interpolation models except for $E_P \mp 200$ mV, in general agreement with the ICP-MS data. Figure 2-15, top-right, shows the Q_{AFTER}/Q_{BEFORE} data from the ICP-MS experiments. No ICP-MS values for Q_{AFTER}/Q_{BEFORE} is available because it's a destructive technique that can only measure Q_{AFTER}. Again, the bias in the ratios from the choice in the linear interpolation range is apparent as $E_P \mp 350$ mV includes more of the curve biasing the peak area upwards, giving the impression that less desorption has occurred and that the SAMs are more stable. In contrast, the models that fit to empirical baselines using blank SAMs are more tightly clustered at lower values consistent with the ICP-MS data and the expectation that the SAM is less stable at these potentials.

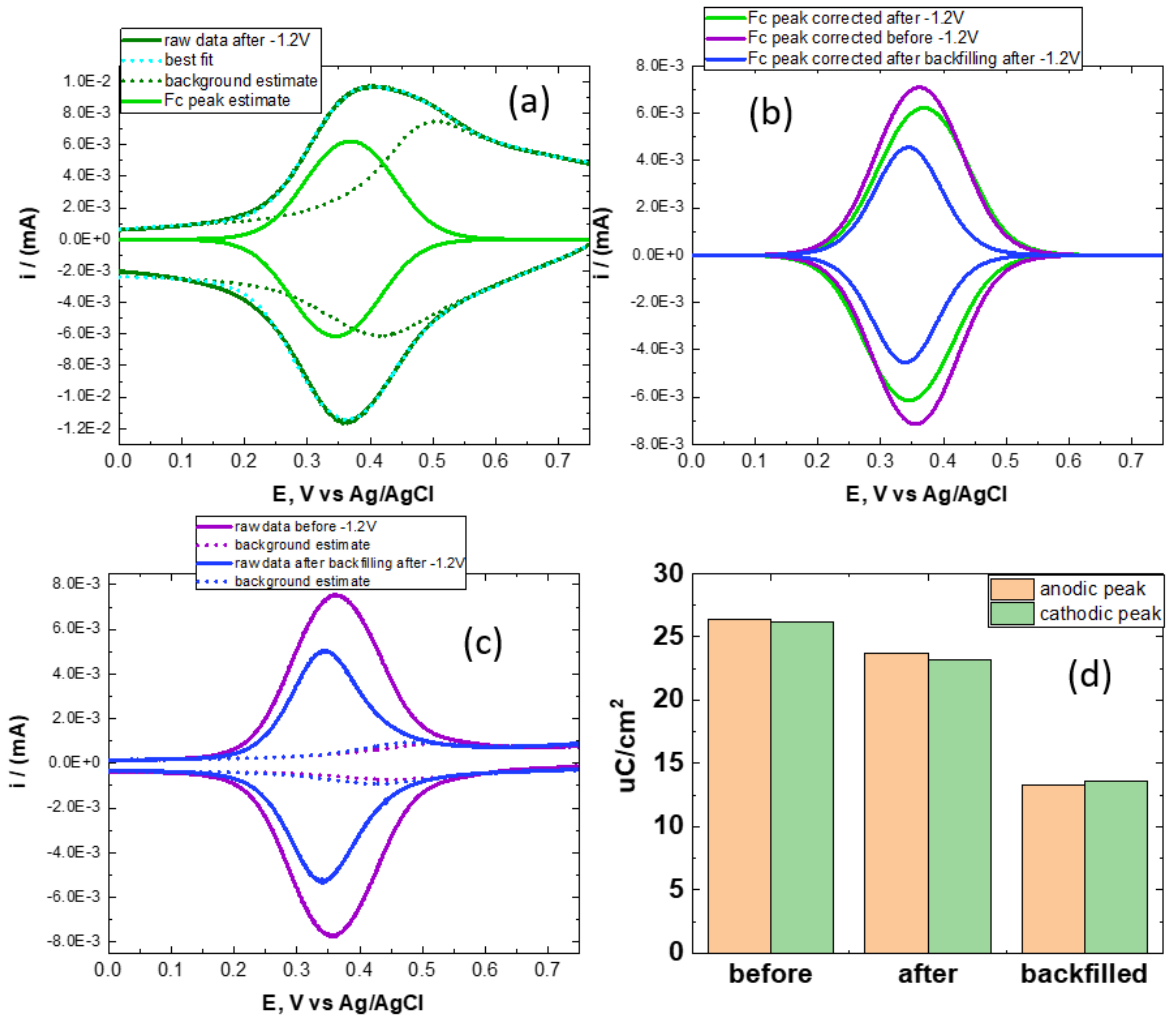

Figure 2-16 Background current correction of CVs from figure 2-10 using 'LASSO + Fc peak fit" model using LASSO regression of empirical backgrounds along with non-linear least squares of the Fc peak using a parametric equation for Fc peak. (a) CV of Fc-SAM after -1.2 V plotted with the model generated background current approximation. (b) CV peaks with backgrounds subtracted from Fc peaks for a Fc-SAM before, after and backfilled after exposure to -1.2V. (c) Raw CVs and background approximations of Fc-SAM before -1.2 V and after -1.2 V and backfilling procedure. (d) Surface area normalized Fc coverage measured using the background corrected peaks shown in (b).

Reexamining the data from figure 2-10 which showed a 180% increase in the measured Fc peak area after -1.2V using linear interpolation, is shown again in figure 2-16 but using the 'LASSO+ Fc peak fit' machine learning model with the empirical C10-SAM backgrounds. The fitting algorithm constructed a peak-shaped non-linear baseline and generated a Fc peak area after -1.2 V that measured an area with a value in between the 'before' measurement, and the results of the 'backfilled' measurement which restored the ideal baseline at the cost of exchanging some of the Fc-thiols for decanethiol (bottom right). In 2-16 top left is a total fit which is in good agreement with the raw data. The 'before' and 'backfilled' scans were also fit with the LASSO models which generates the same coverage values as linear interpolation. CVs of C10-SAM before desorption were included in the basis set making it capable of fitting flat backgrounds.. The 'backfilled' peak area in 2-12 using the LASSO model is ~ 15 $\mu C/cm^2$ which is roughly the same as the 'backfilled' peak area from the same data in figure 2-10 using linear interpolation. The desorption isotherms from figure 2-12 which showed large dispersion in the data points using different linear interpolation ranges were remeasured using the LASSO regression models and peak-fitting algorithms, and are shown in figure 2-17. The data points from the linear interpolation using $E_P \mp 200$ mV are biased higher than empirical machine learning fits which was not the case with the ICP-MS data, which suggests that there are some differences in the experiments using the small-scale electrodes in less pure electrolytes compared to the large-scale electrodes used for the ICP-MS experiments. The large-scale electrodes used high-purity (99.999%) trace-metal electrolytes to permit Fe analysis. The smaller electrode experiments used standard reagent hydroxide (85%) and perchloric acid. The trace metal

experiments did not produce background features as large as the small-scale electrodes in the less pure electrolytes, and showed more apparent desorption of the SAM. The scale and shape of the non-ideal backgrounds are most likely sensitive to impurity profile of the electrolyte, but an investigation into this topic is beyond the scope of this work.

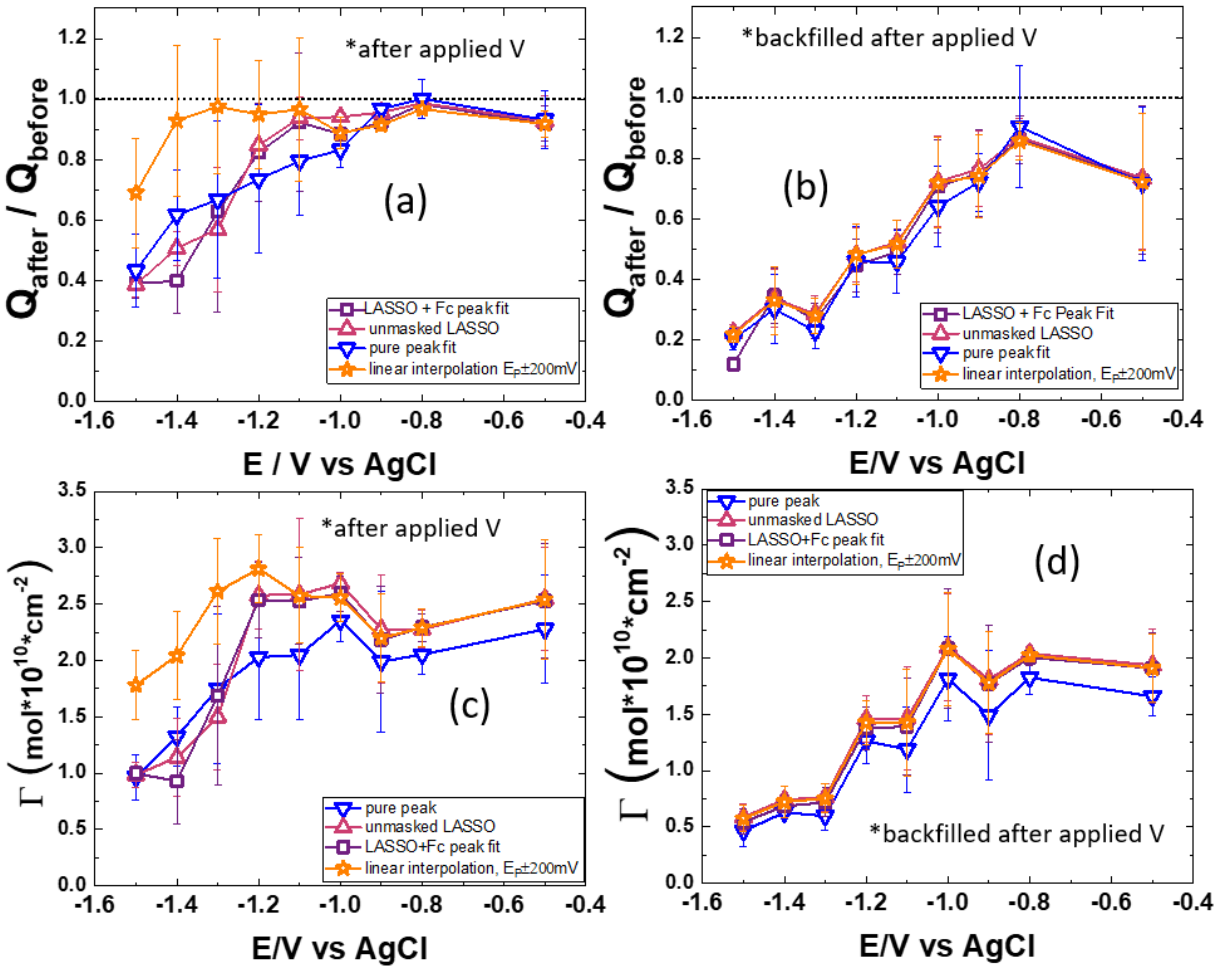

Figure 2-17 Comparison of potential dependent Fc-SAM surface coverages after the different background correction models proposed in the text, including linear interpolation. (a) Average Fc peak after the applied potential normalized with the Fc peak area before the applied potential. (b) Average Fc peak area after backfilling after the applied potential normalized with the before applied potential peak areas. (c) Fc-SAM surface coverage values after the applied potential. (d) Fc-SAM coverage values from backfilling after the applied potential.

Overall, there is less dispersion in the data between models that assume the presence of non-linear peaked-shaped backgrounds for reductively disordered Fc-SAMs compared to linear interpolation, which was shown to be extraordinarily sensitive to the choice of the interpolation range.

2.3.5 In Depth Description of LASSO and Peak Fitting Models with Empirical Backgrounds

The LASSO (least absolute shrinkage and selection operator) regression algorithm is a routine linear regression model found in R programming language for statistics and scikit-learn's machine learning library for Python, which like any linear regression model, finds coefficients for continuous variables and an intercept.[32,33] A standard linear regression representation is shown in 2.5.

(2.5) $$y_i = \beta_0 + \sum_{j=1}^{n} x_{ij}\beta_j + e_i$$

In the model, y_i is the response variable to be modeled, β_0 is an intercept, and $\beta = (\beta_1, \beta_2, .. \beta_n)$ are the coefficients (or weights) for the predictor variables $x = (x_1, x_2, .. x_n)$, where each x_j is a continuous variable with random error e_i. The coefficients are found by minimizing the mean square error:

(2.6) $$\text{minimize: } \frac{1}{2m} \sum_{i=1}^{m} (y_i - \beta_0 - \sum_{j=1}^{n} x_{ij}\beta_j)^2$$

The notable difference between LASSO regression and standard linear regression is that LASSO regression performs variable selection.[32] Variable selection occurs when a subset of variables is chosen from an ensemble of variables when it is not clear which variables are the best predictors or the most correlated. LASSO regression forces sparsity in the prediction variables by forcing

the worst predictor coefficients to zero using regularization, which is an added penalty to the mean square error function[32]:

(2.7) $$\text{minimize: } \frac{1}{2m}\sum_{i=1}^{m}(y_i - \beta_0 - \sum_{j=1}^{n} x_{ij}\beta_j + \lambda\sum_{j=1}^{p}|\beta_j|)^2$$

In 2.7, the added penalty is the term containing λ multiplied by the coefficient β_j. For predictors that have a larger error, λ forces the coefficients towards zero faster than the better correlated predictors. λ is chosen by the modeler when setting up the model, but a typical procedure uses vetted test data to determine which scale of λ is most appropriate by looking at the error as a function of λ. The appropriate λ will depend on the scale of the data.

LASSO regression capable of fitting a curve with an ensemble of standard curves as a basis, assuming the target function is composed of a sum of curves. In the basic electrochemical model of Fc-SAMs, the current response is modeled (to a first order approximation) as the sum of two parallel processes, the background current from double-layer charging (or any other process in parallel), and the Faradaic current from the Fc electron transfer to the surface.

(2.8) $$i_{total} = i_{Fc} + i_{Bckgrnd}$$

The background current, $i_{Bckgrnd}$, could be expanded to include double layer charging (i_{DL}) and potential dependent pseudo-capacitive peaks ($i_{psuedo\text{-}C}$) from specific adsorption at specified sites and pinhole defects in the SAM. The different sites and types of defects give rise to parallel responses which have different onset potentials, $i_{psuedo\text{-}C}$ could be further expanded.

(2.9) $$i_{Bckgrnd} = i_{DL} + i_{psuedo\text{-}C}$$

Using LASSO Regression for Interpolation

The first iteration uses LASSO regression to interpolate under the Fc peak using the C10-SAM CVs as a basis set. To execute this in code, the current data from the disordered C10-SAM was arranged in an n x m array (n columns, and m rows) where each *column* of the matrix is

current data from an individual C10 samples and each *row* corresponds to a potential. The rows have to be aligned at the correct potential going down the rows, along with the target Fc-SAM curve to be fit as 1-d array of length m, with position along the 1d array corresponding to potentials in the rows of the C10 data matrix. This was accomplished in a Jupyter notebook on a Windows machine using Python and scikit-learn's free open-source machine learning library, with Numpy for matrix manipulation, and Matplotlib for visualization.[33]

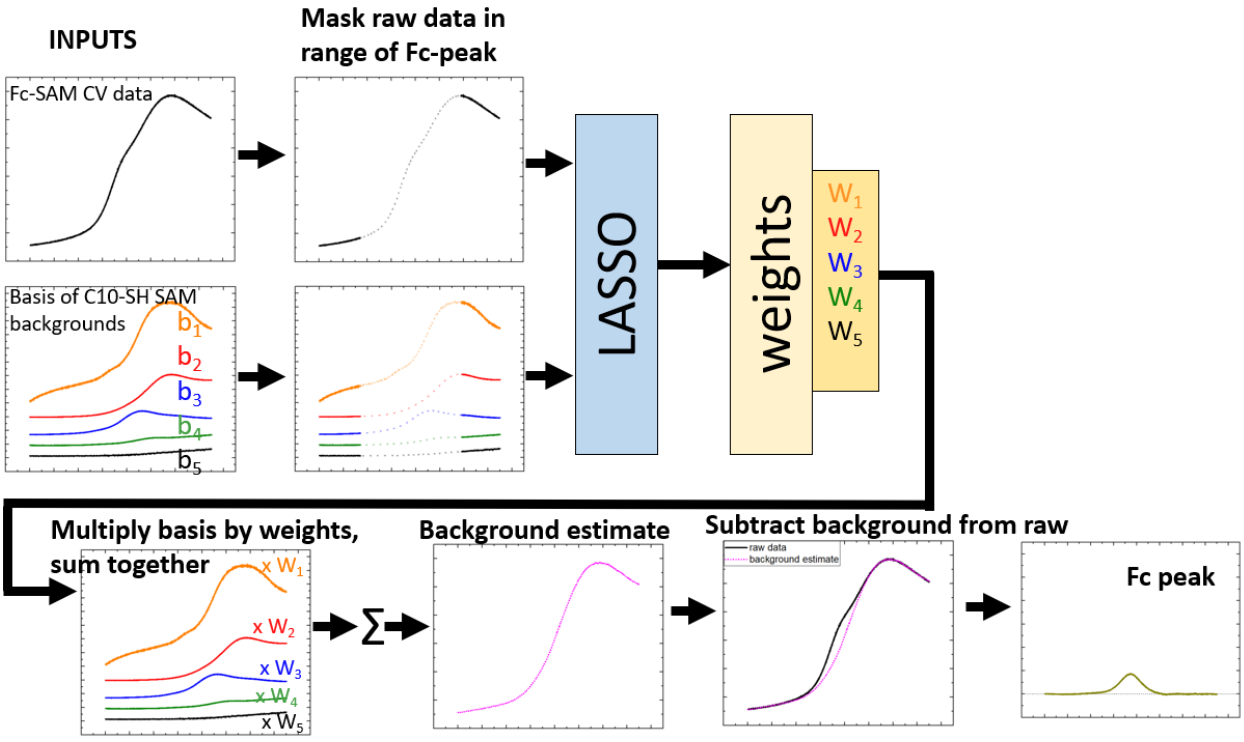

Figure 2-18 Graphical flow chart showing how an empirical basis of C10-SAM current data from desorption experiments can be used to approximate the baseline of a Fc-SAM CV using LASSO regression as an interpolation technique where data outside of the mask is used to generate a baseline.

The initial goal was to generate the baseline using current data only at potentials outside of the assumed Fc peak range, so the Fc peak data was 'masked' by removing the current data from the positions corresponding to the potential range of the Fc peak. Using a 'mask' introduces bias which will be discussed below. The number of rows of the C10 matrix have to match the length of the 'masked' Fc data vector, so the corresponding C10 matrix was masked by removing the equivalent rows which correspond to the potential positions removed from the Fc data vector. Once the Fc peak is masked along with the equivalent rows of the C10 matrix, the LASSO algorithm uses coordinate descent to solve for the weights in 2.10 where $i_{Fc\text{-}SAM}$ is the target data to be fit, and i^n_{C10} is the nth C10-SAM curve supplied as a vector in the basis with its associated weight W^n.

(2.10) $$i_{Fc\text{-}SAM} = W^1 i^1_{C10}(E) + W^2 i^2_{C10}(E) + \ldots + W^n i^n_{C10}(E)$$

This is can represented in matrix form.

$$\begin{pmatrix} i_1^1 & i_1^2 & . & . & i_1^n \\ i_2^1 & i_2^2 & . & . & i_2^n \\ . & . & . & . & . \\ . & . & . & . & . \\ i_m^1 & i_m^2 & . & . & i_m^n \end{pmatrix} \begin{pmatrix} W^1 \\ W^2 \\ . \\ . \\ W^n \end{pmatrix} = \begin{pmatrix} W^1 i_1^1 + W^2 i_1^2 + .. + W^n i_1^n \\ W^1 i_2^1 + W^2 i_2^2 + .. + W^n i_2^n \\ . \\ . \\ W^1 i_m^1 + W^2 i_m^2 + .. + W^n i_m^n \end{pmatrix} = \begin{pmatrix} i_2^h \\ i_2^h \\ . \\ . \\ i_m^h \end{pmatrix}$$

n x m matrix of C10 SAM current data aligned on E axis

Vector of weights to be solved in regression algorithm

result

The weights were restricted to positive numbers only, as the goal was to generate a weighted average of the C10 baselines. Figure 2-15 shows the masking of the data process graphically. After the masked data is fed into the model and the weights are generated, the weights are applied to the original C10 matrix without masking to produce a curve to fit a baseline underneath the Fc peak, which is subtracted for the raw data to isolate the Fc peak. The rationale for masking the data in the range of the Fc peak is to avoid creating a baseline from data that is a

combination of the Fc peak and the baseline. The choice of the mask range again presents a source of bias in the model (like the linear interpolation range) because it makes assumptions about where the Fc peak ends. Figure 2-19 shows different baseline approximations from shrinking the mask range ($E_P \mp 225\ mV \rightarrow E_P \mp 50\ mV$) changes the baseline approximation the raw Fc-SAM data (blue curve in figure 2-19). The arrows point in the direction of the increasing baseline magnitude, which increases as more of the Fc peak is revealed to the algorithm by shrinking the mask range on the Fc peak at 0.38 V. The basis set of C10-SAMs does not have peaks centered at 0.38 V, so it simply scales the baseline in such a way as to minimize the squared error function, which it does by distributing the error along the graph, and creates a poor fit which would be intuitively rejected by a human when it fails to fit to the curve. Assuming that the C10 baselines can be used as a reasonable baseline approximation, alternative approaches that fit all of the data simultaneously were constructed to avoid making explicit assumptions about the limits of the Fc peak. Fitting all of the data points simultaneously requires both a representation of the Fc peak and the baseline peaks in the model.

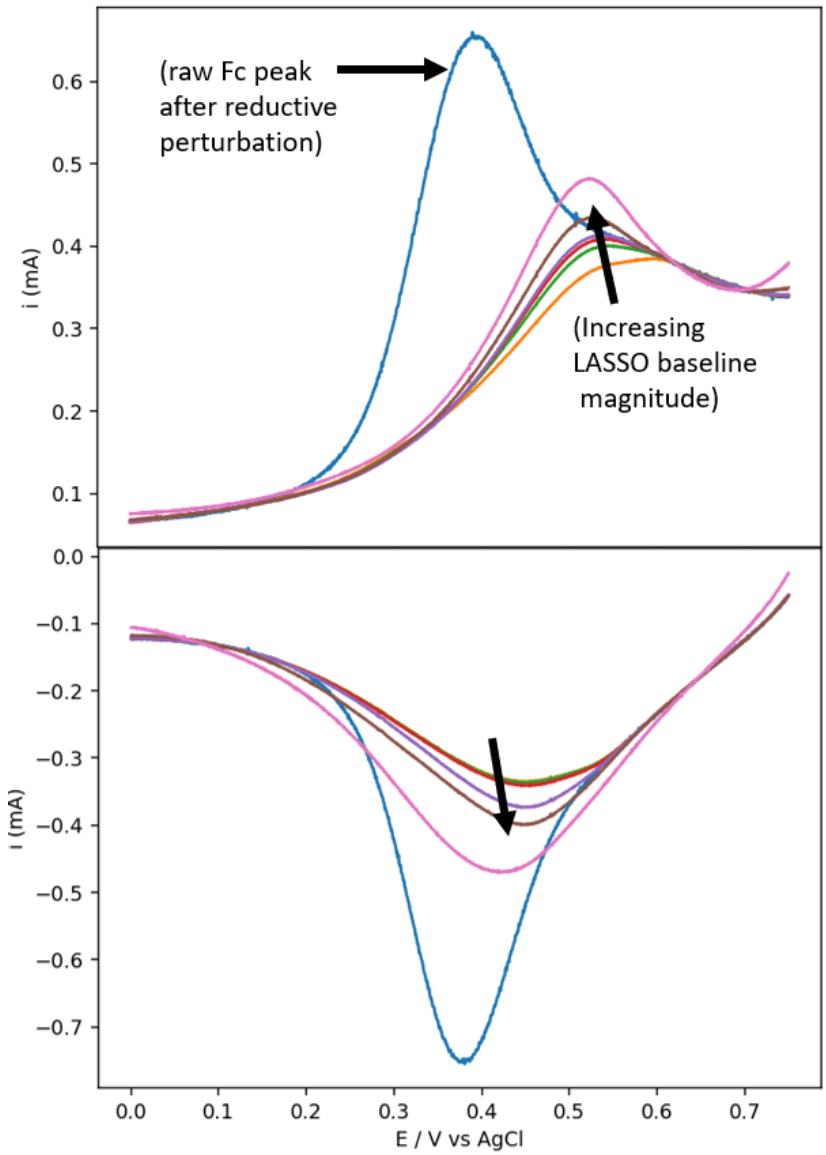

Figure 2-19 Baseline fits to the non-ideal Fc-SAM baseline. Each baseline curve is generated from a different masking range shrinking towards the Fc peak at 0.38 V.

LASSO + Fc Peak Fitting Using Non-Linear Least Squares and the Generalized Lateral Interaction Model

Fitting the Fc peak while simultaneously fitting the baseline with the ensemble of empirical solutions generated from different masking ranges avoids the bias of incorrectly overfitting the curve where the Fc peak is present. A blended approach using a suitable parametric equation for the Fc peak was employed. Alévêque and Levillain's generalized lateral interaction model, equation 2.11, was used for fitting the Fc peak.[34]

$$2.11\quad \mathrm{Fc(E)} = \frac{n^2F^2Av}{RT}\,\frac{\Gamma\exp(X)}{(1+\exp(X))^2-2\beta exp(X)}, \qquad X = \frac{nF(E-E_P)}{RT} + \frac{2\beta}{1-\exp\left(\frac{-nF(E-E_P)}{RT(1-Y\beta)}\right)} - \beta$$

In 2.11, n is the integer number of electrons passed in the redox molecule (Fc), F is Faraday's number, A is the surface area, v is the scan rate, R is the ideal gas constant, T is temperature and Γ is the surface coverage (mol/cm^2), E is potential, E_P is the peak potential, and β which is an interaction parameter which describes repulsive and attractive electrostatic forces between the redox molecules. When β=0, the attractive and repulsive forces are balanced. When β>0, there is a net attractive force and the resulting peak shape is sharp and narrow. When β<0, net repulsive forces dominate, which broadens the peak.

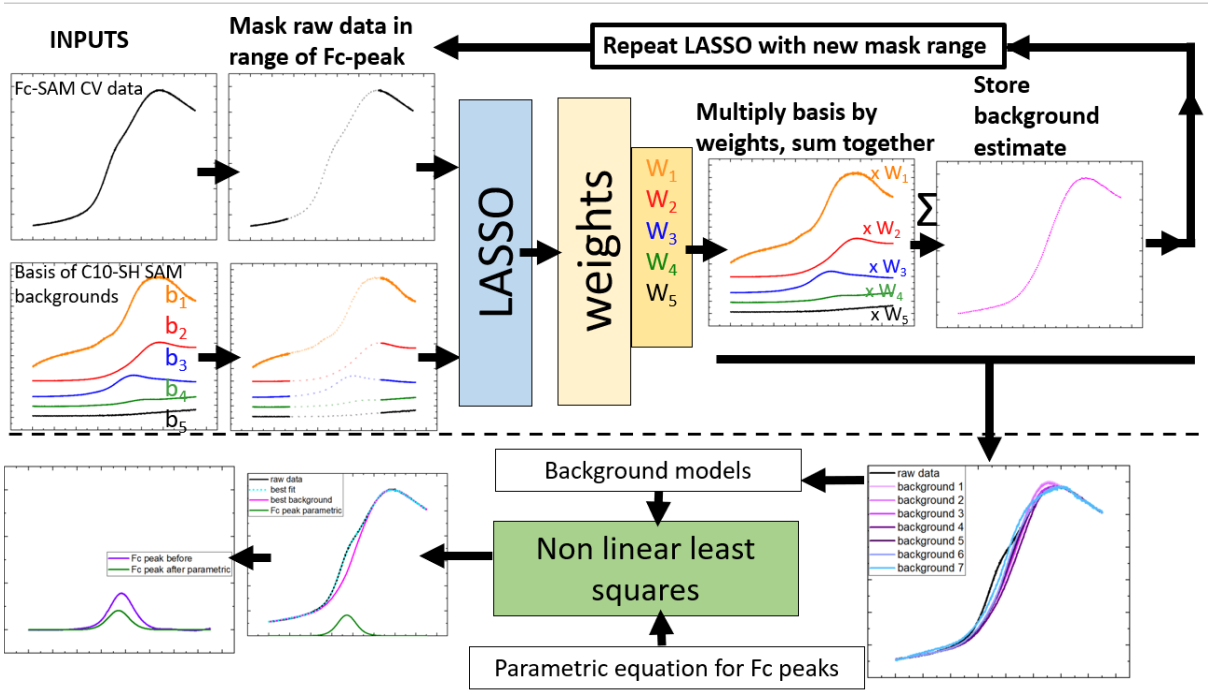

Figure 2-20 LASSO + Fc peak fitting flow chart. An ensemble of candidate baselines is generated by LASSO with different mask ranges shrinking toward 0.38 V. The Fc peak is fit with a parametric equation simultaneously applying using equation 2.11.

2.11 was employed using non-linear least squares in Python using the LMFIT module with the Levenberg-Marquardt algorithm for fitting non-linear parametric equations.[35] The ensemble of baselines generated from different masking ranges were fit simultaneously with the Fc peak parameters using weights to construct a weighted sum of the candidate baselines shown in equation 2.12.

(2.12) $i(E) = Fc(E) + W^1 i^1_{C10}(E) + W^2 i^2_{C10}(E) + \ldots + W^n i^n_{C10}(E)$

The fitting the procedure shown in 2-20 was applied to the data originally shown 2-19, in which different masking ranges produced different baselines. The baselines that poorly fit were assigned weights at or close to zero from fitting procedure, while simultaneously generating a fit for the Fc peak and a total fit for the curve, which is shown graphically in figure 2-21.

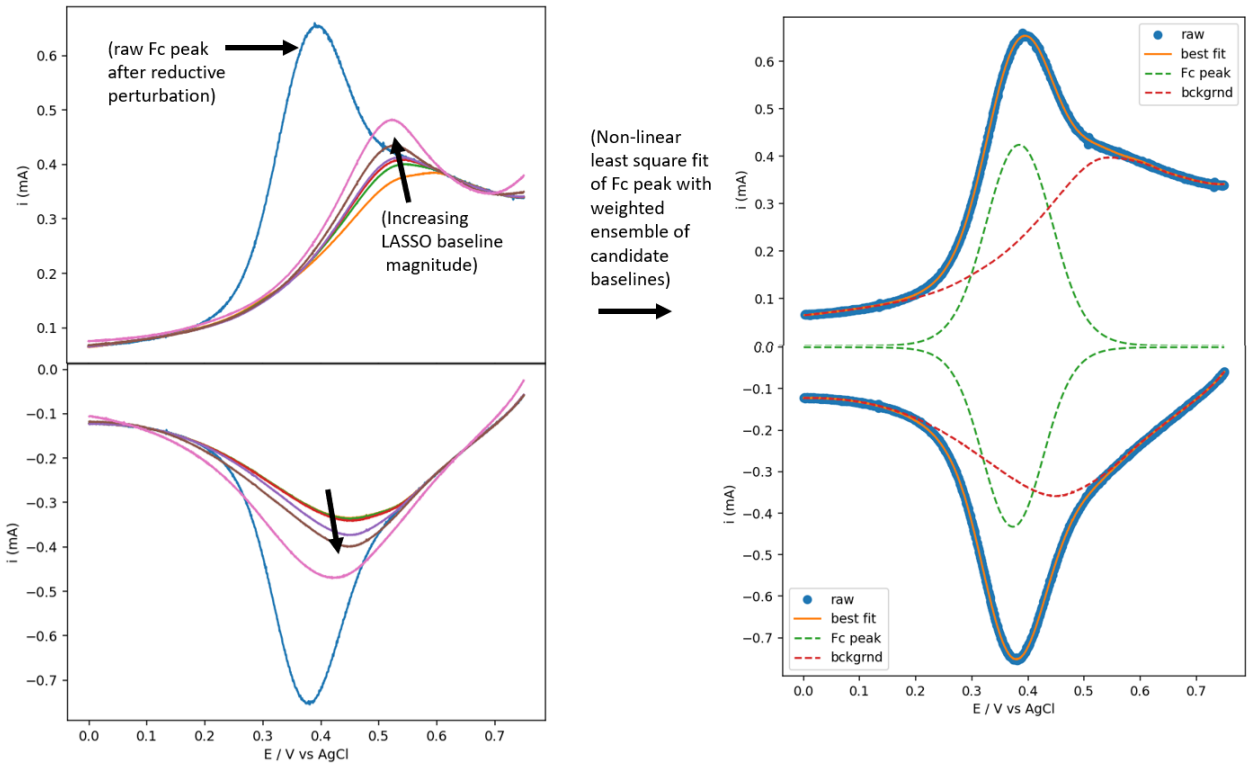

Figure 2-21 Left: Raw non-ideal Fc-SAM CV with ensemble of candidate baselines generated from different mask ranges of the raw data using LASSO regression. Right: Refined fit of the Fc-SAM curve using a weighted average of the baseline ensemble and a parametric equation for the Fc peak.

Unmasked LASSO Model

A purely empirical fit can be achieved with the LASSO regression model by adding the baseline corrected ‘before’ Fc peak to the matrix of C10 baselines and then fitting the data. This requires no masking or interpolation range as the data is fit simultaneously using the baselines and a representative Fc peak. The resulting weights for C10 columns in the fitting matrix are used to reconstruct the baseline and subtracted from the raw data to analyze the remaining Fc peak area. The weighted ‘before’ Fc peak which can also be used to estimate the Fc coverage after desorption. Figure 2-22 graphically depicts this method. Figure 2-20 shows the results of fitting the same data in 2-18 using the unmasked LASSO model.

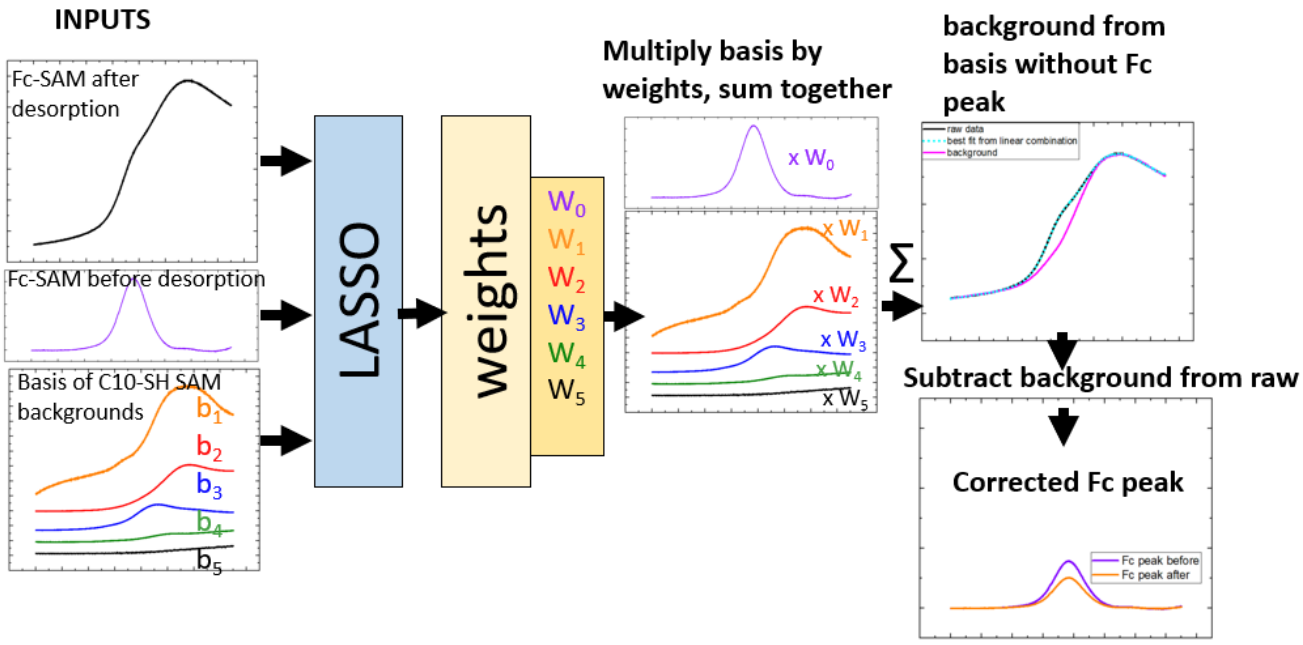

Figure 2-22 Graphical schematic of the unmasked LASSO fitting procedure.

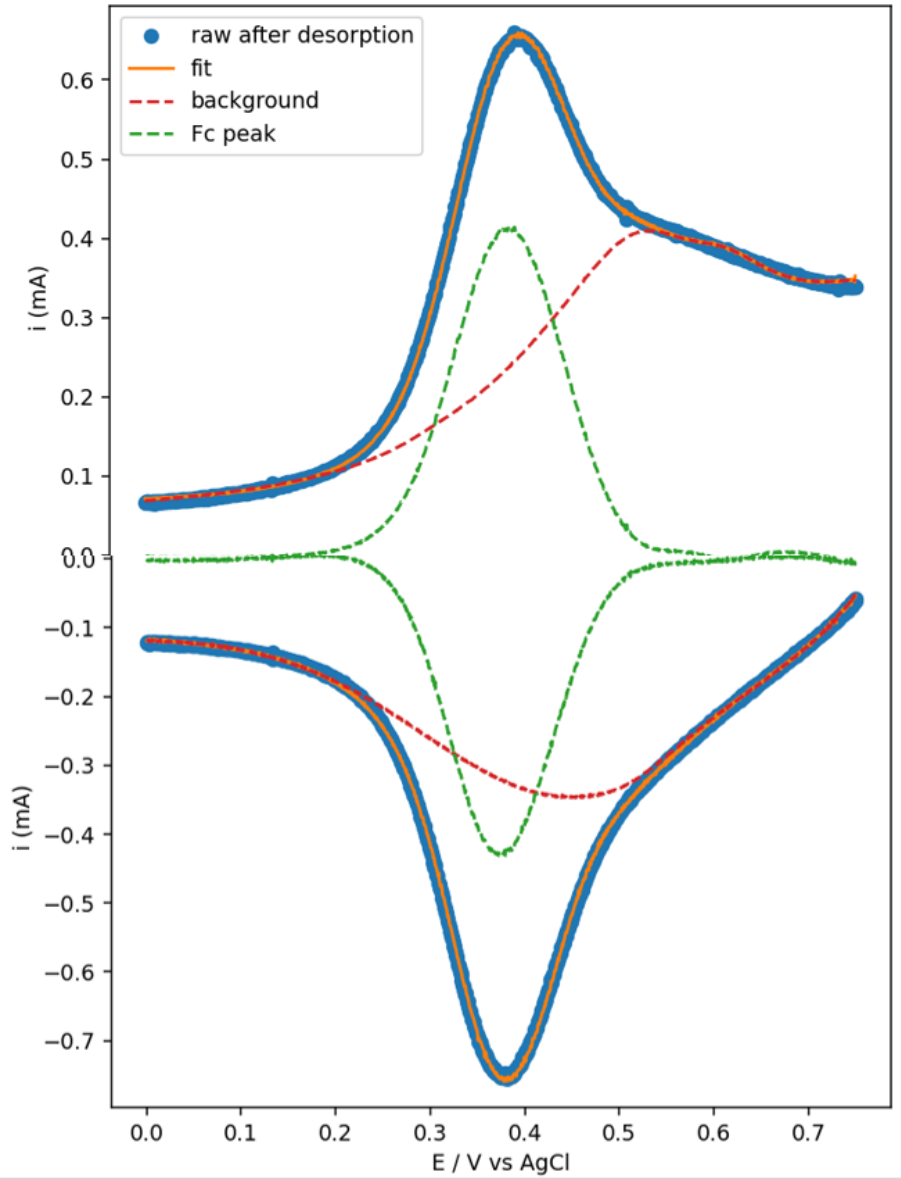

Figure 2-23 Results of LASSO Unmasked Model.

Pure Peak Fitting Model

The model labelled pure peak fitting used non-linear least squares and equation 2.11 to fit peaks the Fc peak and the two additional "background" peaks. A similar strategy was used to fit electrochemical surface peaks for Pt.[31] Here the two additional "background" peaks were initialized within the range of potentials positive of the Fc peaks (> 0.45V), along with a linear baseline with a slope for double layer charging. Only the peak first peak area was considered in the peak area analysis while the other two peak fitting and the linear baseline were added together and labelled as a baseline. Figure 2-24 shows the results of the fitting. The problem with this approach is the function of the baseline is unknown, and using the generalized interaction model for baseline peaks may not be the best function to approximate these peaks.

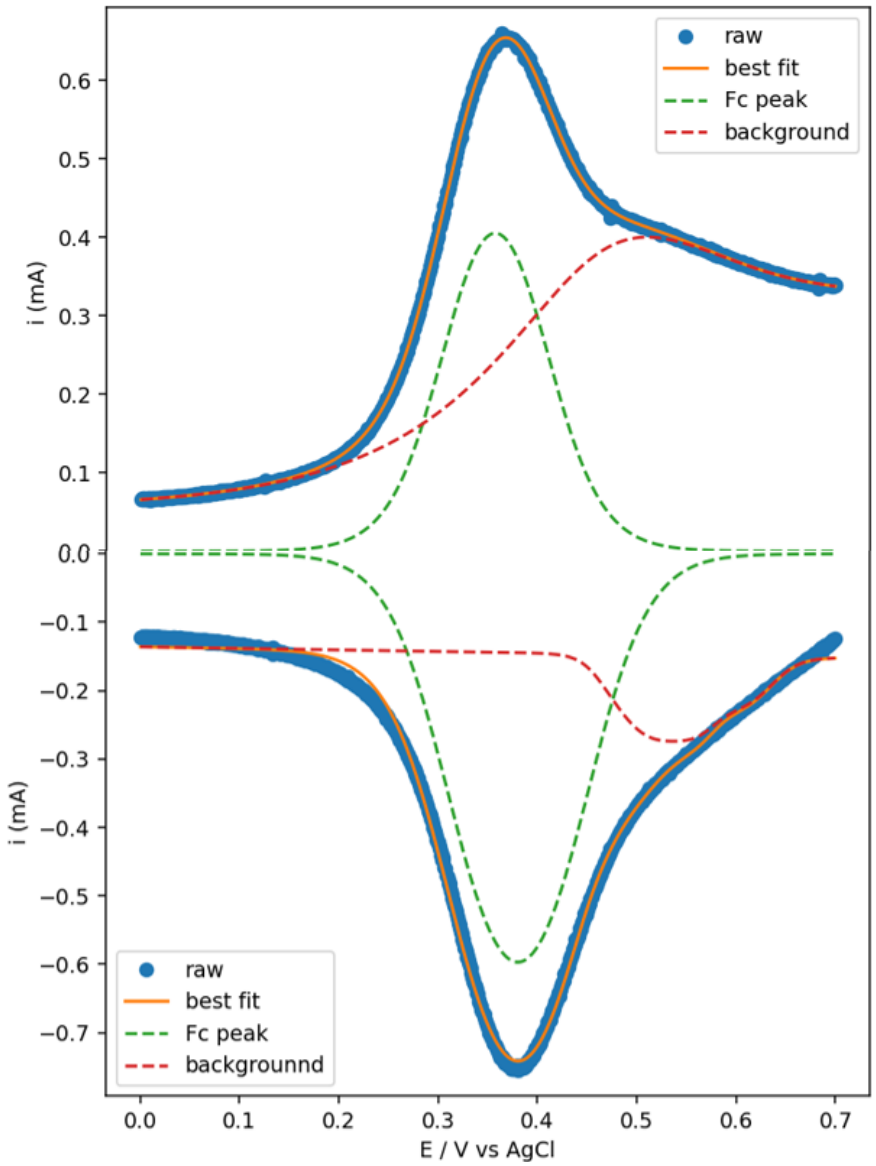

Figure 2-24 Results of peak fitting using non-linear least squares and the generalized interaction model for the Fc peak and background peak along with a linear baseline.

LASSO Model Limitations

The LASSO regression background correction models perform well for estimating coverages on χ=0.5 and χ=0.75 Fc-SAMs which have relatively high coverages before any potential perturbation is applied, but for χ=0.25 Fc-SAMs starting with lower Fc coverage, underfitting the background leads to unreliable results. Figure 2-22 top row shows an example of a successful fitting of a χ=0.25 Fc-SAMs where the fitting generates a peak area for the 'after' scan in between the 'before' CV scan and the backfilled CV scan. In contrast the bottom row shows the results of an unsuccessful baseline correction as the resulting peak area -1.3 V shows a peak area over double the initial peak area. Determining the limits of quantification for CV measurement of electrochemical SAMs is seldom discussed in the literature.

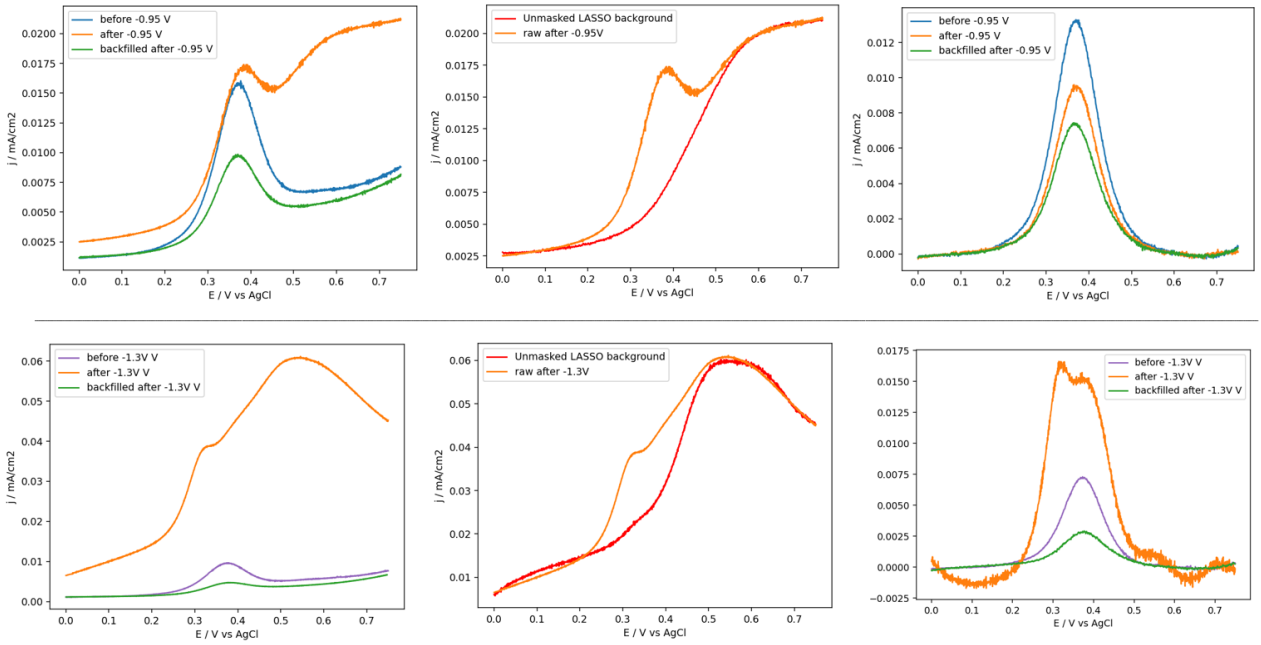

Figure 2-25 Top left shows the raw CV data for a χ=0.25 Fc-SAM of the before, after -0.95 V and backfilled scans. Top center shows the fitting of the baseline using the "unmasked LASSO" model. Top right shows the background corrected before, after and backfilled scans background corrected using the LASSO model. The bottom row shows the same sequence for a different χ=0.25 Fc-SAM when the applied potential was -1.3 V, where the model underfits the data (bottom center) leading to measurement of Fc coverage greater than before desorption.

2.4 Conclusions

Quantitative measurement of reductively disordered ferrocene self-assembled monolayers was explored using cyclic voltammetry. The application of reductive potentials transformed the Fc-SAM CV baselines from flat and ideal, to non-linear and curved, with features that correlate with peaks that were observed on bare Au and reductively disordered decanethiol SAMs. The resulting Fc peak area measurements after the reductive perturbations are extremely sensitive to the interpolation range used to baseline correct the CV. New CV baselining techniques which use empirical CV curves from reductively disordered decanethiol SAMs coupled with LASSO regression were able to reasonably approximate the Fc baseline without using explicit bias in the assuming the Fc peak limits. The LASSO regression model was benchmarked using secondary confirmation of the Fc coverage using ICP-MS and found to be in good agreement.

2.5 References

(1) Eckermann, A. L.; Feld, D. J.; Shaw, J. A.; Meade, T. J. "Electrochemistry of redox-active self-assembled monolayers," *Coord. Chem. Rev.* **2010**, *254*, 1769-1802.
(2) Bueno, P. R.; Fabregat-Santiago, F.; Davis, J. J. "Elucidating Capacitance and Resistance Terms in Confined Electroactive Molecular Layers," *Anal. Chem.* **2013**, *85*, 411-417.
(3) Fleischmann, S.; Mitchell, J. B.; Wang, R.; Zhan, C.; Jiang, D.-e.; Presser, V.; Augustyn, V. "Pseudocapacitance: From Fundamental Understanding to High Power Energy Storage Materials," *Chem. Rev.* **2020**, *120*, 6738-6782.
(4) Holtan, M. D.; Somasundaram, S.; Khuda, N.; Easley, C. J. "Nonfaradaic Current Suppression in DNA-Based Electrochemical Assays with a Differential Potentiostat," *Anal. Chem.* **2019**, *91*, 15833-15839.
(5) Costentin, C.; Porter, T. R.; Savéant, J.-M. "How Do Pseudocapacitors Store Energy? Theoretical Analysis and Experimental Illustration," *ACS Applied Materials & Interfaces* **2017**, *9*, 8649-8658.
(6) Mickelson, L.; Friesen, C. "A Minimally Arbitrary Numerical Method for the Separation of Faradaic and Background Currents of Interest," *Electrochem. Solid-State Lett.* **2009**, *12*, F43.
(7) Jakubowska, M. "Signal Processing in Electrochemistry," *Electroanalysis* **2011**, *23*, 553-572.
(8) Calvente, J. J.; Andreu, R. "Intermolecular interactions in electroactive thiol monolayers probed by linear scan voltammetry," *Current Opinion in Electrochemistry* **2017**, *1*, 22-26.
(9) Laviron, E. "The use of linear potential sweep voltammetry and of a.c. voltammetry for the study of the surface electrochemical reaction of strongly adsorbed systems and of redox modified electrodes," *Journal of Electroanalytical Chemistry and Interfacial Electrochemistry* **1979**, *100*, 263-270.
(10) Collman, J. P.; Devaraj, N. K.; Chidsey, C. E. "“Clicking” functionality onto electrode surfaces," *Langmuir* **2004**, *20*, 1051-1053.
(11) Brassard, C. J.; Zhang, X.; Brewer, C. R.; Liu, P.; Clark, R. J.; Zhu, L. "Cu(II)-Catalyzed Oxidative Formation of 5,5′-Bistriazoles," *The Journal of Organic Chemistry* **2016**, *81*, 12091-12105.
(12) Collman, J. P.; Devaraj, N. K.; Eberspacher, T. P. A.; Chidsey, C. E. D. "Mixed Azide-Terminated Monolayers: A Platform for Modifying Electrode Surfaces," *Langmuir* **2006**, *22*, 2457-2464.
(13) Chidsey, C. E. D. "Free Energy and Temperature Dependence of Electron Transfer at the Metal-Electrolyte Interface," *Science* **1991**, *251*, 919-922.
(14) Walczak, M. M.; Popenoe, D. D.; Deinhammer, R. S.; Lamp, B. D.; Chung, C.; Porter, M. D. "Reductive desorption of alkanethiolate monolayers at gold: a measure of surface coverage," *Langmuir* **1991**, *7*, 2687-2693.
(15) Azzaroni, O.; Vela, M. E.; Fonticelli, M.; Benítez, G.; Carro, P.; Blum, B.; Salvarezza, R. C. "Electrodesorption Potentials of Self-Assembled Alkanethiolate Monolayers on Copper Electrodes. An Experimental and Theoretical Study," *The Journal of Physical Chemistry B* **2003**, *107*, 13446-13454.

(16) Bengió, S.; Fonticelli, M.; Benítez, G.; Creus, A. H.; Carro, P.; Ascolani, H.; Zampieri, G.; Blum, B.; Salvarezza, R. C. "Electrochemical self-assembly of alkanethiolate molecules on Ni (111) and polycrystalline Ni surfaces," *The Journal of Physical Chemistry B* **2005**, *109*, 23450-23460.
(17) Popenoe, D. D.; Deinhammer, R. S.; Porter, M. D. "Infrared spectroelectrochemical characterization of ferrocene-terminated alkanethiolate monolayers at gold," *Langmuir* **1992**, *8*, 2521-2530.
(18) Valincius, G.; Niaura, G.; Kazakevičienė, B.; Talaikytė, Z.; Kažemėkaitė, M.; Butkus, E.; Razumas, V. "Anion Effect on Mediated Electron Transfer through Ferrocene-Terminated Self-Assembled Monolayers," *Langmuir* **2004**, *20*, 6631-6638.
(19) Ataka, K.-i.; Yotsuyanagi, T.; Osawa, M. "Potential-Dependent Reorientation of Water Molecules at an Electrode/Electrolyte Interface Studied by Surface-Enhanced Infrared Absorption Spectroscopy," *The Journal of Physical Chemistry* **1996**, *100*, 10664-10672.
(20) Hamelin, A.; Sottomayor, M. J.; Silva, F.; Chang, S.-C.; Weaver, M. J. "Cyclic voltammetric characterization of oriented monocrystalline gold surfaces in aqueous alkaline solution," *Journal of Electroanalytical Chemistry and Interfacial Electrochemistry* **1990**, *295*, 291-300.
(21) Hamelin, A.; Martins, A. M. "Cyclic voltammetry at gold single-crystal surfaces. Part 2. Behaviour of high-index faces," *J. Electroanal. Chem.* **1996**, *407*, 13-21.
(22) Hamelin, A. "Cyclic voltammetry at gold single-crystal surfaces. Part 1. Behaviour at low-index faces," *J. Electroanal. Chem.* **1996**, *407*, 1-11.
(23) Xu, X.; Makaraviciute, A.; Pettersson, J.; Zhang, S.-L.; Nyholm, L.; Zhang, Z. "Revisiting the factors influencing gold electrodes prepared using cyclic voltammetry," *Sensors and Actuators B: Chemical* **2019**, *283*, 146-153.
(24) Angerstein-Kozlowska, H.; Conway, B. E.; Hamelin, A.; Stoicoviciu, L. "Elementary steps of electrochemical oxidation of single-crystal planes of Au—I. Chemical basis of processes involving geometry of anions and the electrode surfaces," *Electrochim. Acta* **1986**, *31*, 1051-1061.
(25) Angerstein-Kozlowska, H.; Conway, B. E.; Hamelin, A.; Stoicoviciu, L. "Elementary steps of electrochemical oxidation of single-crystal planes of Au Part II. A chemical and structural basis of oxidation of the (111) plane," *Journal of Electroanalytical Chemistry and Interfacial Electrochemistry* **1987**, *228*, 429-453.
(26) Lipkowski, J.; Shi, Z.; Chen, A.; Pettinger, B.; Bilger, C. "Ionic adsorption at the Au(111) electrode," *Electrochim. Acta* **1998**, *43*, 2875-2888.
(27) Kerner, Z.; Pajkossy, T. "Measurement of adsorption rates of anions on Au(111) electrodes by impedance spectroscopy," *Electrochim. Acta* **2002**, *47*, 2055-2063.
(28) Zhumaev, U.; Lai, A.; Pobelov, I.; Kuzume, A.; Rudnev, A.; Wandlowski, T. "Quantifying perchlorate adsorption on Au (1 1 1) electrodes," *Electrochim. Acta* **2014**, *146*, 112-118.
(29) Corthey, G.; Rubert, A. A.; Benitez, G. A.; Fonticelli, M. H.; Salvarezza, R. C. "Electrochemical and X-ray photoelectron spectroscopy characterization of alkanethiols adsorbed on palladium surfaces," *The Journal of Physical Chemistry C* **2009**, *113*, 6735-6742.
(30) Collman, J. P.; Hosseini, A.; Eberspacher, T. A.; Chidsey, C. E. D. "Selective Anodic Desorption for Assembly of Different Thiol Monolayers on the Individual Electrodes of an Array," *Langmuir* **2009**, *25*, 6517-6521.
(31) Bucur, R. "Structure of the voltammograms of the platinum-black electrodes: Derivative voltammetry and data fitting analysis," *Electrochim. Acta* **2014**, *129*, 76-84.

(32) Hastie, T.; Tibshirani, R.; Wainwright, M. "Statistical learning with sparsity," *Monographs on statistics and applied probability* **2015**, *143*, 143.
(33) Pedregosa, F.; Varoquaux, G.; Gramfort, A.; Michel, V.; Thirion, B.; Grisel, O.; Blondel, M.; Prettenhofer, P.; Weiss, R.; Dubourg, V. "Scikit-learn: Machine learning in Python," *the Journal of machine Learning research* **2011**, *12*, 2825-2830.
(34) Alévêque, O.; Levillain, E. "A generalized lateral interactions function to fit voltammetric peaks of self-assembled monolayers," *Electrochem. Commun.* **2016**, *67*, 73-79.
(35) Newville, M.; Stensitzki, T.; Allen, D. B.; Rawlik, M.; Ingargiola, A.; Nelson, A. "LMFIT: Non-linear least-square minimization and curve-fitting for Python," *Astrophysics Source Code Library* **2016**, ascl: 1606.1014.

Chapter 3 The Effect of Potential, Time and Electrolyte Composition on the Reductive Stability of Ferrocene-capped Self-Assembled Monolayers

3.1 Introduction

The concept of electrochemical reductive desorption of alkanethiol self-assembled monolayers (SAMs) on Au surfaces has evolved after decades of research, from a simplified reductive elimination type mechanism, to a more complex process involving surface and solvent interactions.[1] Initial reports used the charge passed under a desorption peak observed in cyclic voltammetry (CV) for estimating thiol coverages assuming a one-electron process as shown in equation 3.1.[2]

$$\text{(3.1)} \quad \text{Au-S-R} + e^- \rightleftharpoons \text{Au} + {}^-\text{S-R}$$

Loss of the reduced thiol to the bulk electrolyte was presumed, but later investigations concluded that not all SAMs immediately dissolve, and more complicated hypotheses developed about multi-stage desorption (equation 3.2), or in some cases no desorption all.[3-19]

$$\text{(3.2)} \quad \text{Au-S-R} + e^- \rightleftharpoons \text{Au}(0) + {}^-\text{S-R}_{\text{surface}} \rightleftharpoons \text{Au}(0) + {}^-\text{S-R}_{\text{electrolyte}}$$

In equation 3.2, ${}^-\text{S-R}_{\text{surface}}$ is a thiolate physiosorbed near or on the surface after the reduction which breaks the Au-S bond and will diffuse into the bulk electrolyte to become the solvated species, ${}^-\text{S-R}_{\text{electrolyte}}$. The extent of diffusion into the electrolyte depends on the length of the alkyl chain[7,13,14,16], the pH[4,5,9], and in some reports, the time[7,10,12,19] at a given potential. The evidence for SAM retention near the surface comes from 1) observation of an oxidative re-adsorption peak[6,7,20] upon scanning back towards positive potentials in "desorption" CVs and the persistence of the cathodic desorption peak[13,14,16] observed in

repeated cycles after the first cathodic sweep, and 2) observation of infra-red (IR) vibrational modes of alkyl-stretches using surface-selective spectroscopy techniques[13,14,16]. While the evidence is compelling at qualitatively describing the complexity of SAM reductive desorption, a few caveats are worth considering. A challenge in interpreting surface spectroscopic data is the requirement of a net dipole component normal to the surface, and non-random orientation breaking inversion symmetry[21]. Disorganized molecules present on the surface with randomly-oriented dipoles present no spectroscopic handle for measurement, making them invisible even though they could remain present on the surface. Similar arguments can be made for the CV oxidative re-adsorption peaks mentioned above, which is really only observed for longer chained alkyl-thiols and appears to be sensitive to the surface preparation.[7,11] A quantitative measurement of the surface coverage independent of these methods could confirm complete or incomplete desorption and its correlation to the cathodic peak observed in the reductive "desorption" CVs.

A direct measurement of thiol surface coverage is challenging using traditional analytical chemistry techniques due to the small amounts of material (~ 0.7 nano-moles cm^{-2}) in question for a typical electrode dimension (5 mm diameter). However, accurate surface coverages can be measured with cyclic voltammetry of redox-active SAMs at stable anodic potentials where SAMs are functionalized with redox-active moieties such as with ferrocene (Fc) terminated SAMs.[22] Fc-SAMs undergo the well-known reversible one-electron reduction and oxidation (equation 3.3) and the relationship of Faradays law is used to convert charge to molar quantities (equation 3.4).[23]

$$\text{(3.3)} \quad \text{Au-S-R-Fc}^{+} + e^{-} \rightleftharpoons \text{Au-S-R-Fc}$$

$$\text{(3.4)} \quad \Gamma = Q/AnF$$

Γ is the SAM coverage in mol cm^{-2}, Q is the charge measured via integration of the Fc oxidation or reduction peak in a CV, A is the area of the electrode, n is the integer number of electrons passed per mole of Fc and F is the conversion factor from charge to moles. Surprisingly, very few papers take advantage of redox-active SAMs to measure surface coverage after reductive desorption CVs.

A few studies have used Fc-SAMs as a tool to measure coverage after reductive desorption. Fc-SAMs were used indirectly to label bare Au sites after a reductive desorption of tetradecanethiol SAMs, and noted that Fc-SAMs themselves were not appreciably desorbed after sweeping past the SAM desorption CV peak evidenced by the 92% of the Fc peak remaining.[10] Similar results were observed from the other works with mixed-Fc-SAMs using hexanethiol as a diluent.[8] A more negative desorption peak was observed with increasing Fc-terminated fraction of the SAM, but again, no appreciable loss of the Fc peaks themselves after several cathodic sweeps in hydroxide solutions. Earlier work measured Fc-SAM reductive desorption directly in dichloromethane, but not in aqueous electrolytes, and $\sim$ 0.75 hours at -1.8V vs AgCl was required to appreciably remove the Fc-SAMs.[24]

These studies leave some remaining questions about the effects of reductive perturbations of Fc-SAMs in aqueous electrolytes. Could there be a time-dependence for desorption away from the surface in aqueous electrolytes? If Fc-thiols remain near or on the surface after reductive desorption in aqueous electrolytes, could hydrodynamic flow remove them during an applied constant potential? Could the extent of desorption, and the desorption kinetics be increased using mixed aqueous/methanolic electrolytes? The goal of this study will be to probe these questions and reflect on how these measurements agree or

disagree with the simplified interpretation that desorption CV peaks indicate the loss of the SAM from the surface.

3.2 Experimental Methods

3.2.1 Materials

Chemicals purchased were used as received. Water was purified to 18.2MΩ cm resistivity with a Thermo Scientific GenPure UV-TOC/UF x CAD-plus water purification system. 11-bromo-1-undecanol was purchased from Accela. Methanesulfonyl chloride (99.5%), copper (II) sulfate pentahydrate (99+%), and potassium thioacetate (98%) were purchased from Acros Organics. Ferrocenecarboxylic acid was purchased from Aldrich. Perchloric acid (ACS, 60-62%), L-(+)-ascorbic acid (ACS, 99+%), tripropargylamine (97%), benzyl azide (94%), copper (II) acetate (anhydrous powder), and decanethiol (96%) were purchased from Alfa Aesar. Ethynylferrocene was acquired from Chem Scene. Ethanol (200 proof, anhydrous) was purchased from Decon Laboratories. Ethyl Ether was purchased from Fisher. Hydrochloric acid (GR ACS) was purchased from Millipore. Sodium phosphate monobasic and dibasic (Bioultra ≥ 99.0%) were purchased from Sigma. Potassium Hydroxide (ACS reagent, >85% pellets), methanol (HPLC grade, ≥ 99.9%), N,N-dimethylformamide (anhydrous, 99.8%), triethylamine (≥99%), tetrahydrofuran (anhydrous, ≥99.9%), sodium bicarbonate (ACS reagent >99.7%), tert-butanol (ACS reagent, ≥99.0%), and dimethyl sulfoxide (ACS reagent ≥ 99.9%) were purchased from Sigma-Aldrich. Potassium chloride (99%) and sodium azide were purchased from Thermo Scientific. Si wafers were purchased from University Wafers.

3.2.2 Synthesis of 1-Azidoundecane-11-thiol

1-Azidoundecane-11-thiol was synthesized following the procedure found in " "Clicking" Functionality onto Electrode Surfaces" by Collman et al.[25]

3.2.3 Synthesis of tris[(1-benzyl-1H-1,2,3-triazol-4-yl)methyl]amine (TBTA)

TBTA was synthesized using the "modified TBTA synthesis" found in "Cu(II)-Catalyzed Oxidative Formation of 5,5′-Bistriazoles" by Brassard et al.[26]

3.2.4 Gold Electrodes

Gold electrodes were prepared by physical vapor deposition of a 20-25 nm titanium adhesion layer followed by 200-250 nm of gold onto silicon wafers using an Angstrom Engineering Evovac Evaporator in the clean room at the Lurie Nanofabrication Facility.

3.2.5 Preparation of Mixed Ferrocene-capped Self-Assembled Monolayers on Au Electrodes

One millimolar stock solutions of 1-azidoundecane-11-thiol and decanethiol in neat ethanol pre-sparged with nitrogen gas to slow down oxidation of the thiols to disulfide, were prepared as separate solutions. For a desired mole-fraction (χ), the stock solutions were added to a beaker with proportionate volumes of the stock thiol solutions to achieve the desired χ, then stirred for five to ten minutes using a stir bar/magnetic stir plate, to thoroughly mix the solution, under a blanket of nitrogen gas, in a chemical fume hood. Freshly evaporated Au coated silicon wafers were hand-cut into ~ 1 cm x 2 cm coupons using a glass cutter and placed into a 20 mL scintillation vials. The mixed thiol solution was added to the scintillation vials with the Au coupons, and capped tightly, wrapped in aluminum foil, and stored in the dark for four days.

Reaction of ethynylferrocene with azide-terminated SAMs was adapted from work of Collman et al.[27] After four days of thiol deposition, the "Cu(I) Click" solution was prepared first by dissolving Cu (II) sulfate pentahydrate (7.5 mg) into 25 mL of purified water. Next TBTA (21

mg), and ethynylferrocene (21 mg) were dissolved in 75 mL of dimethylsulfoxide (DMSO). The water solution containing Cu(II) and DMSO solutions with TBTA and ethynylferrocene, were combined in a beaker and stirred using a stir bar and magnetic stir plate, in a chemical fume hood, until the heat of solvation dissipated and the resulting solution returned to room temperature. While the DMSO/water solution was cooling, the Au coupons with the deposited thiols were removed from the vials, thoroughly rinsed with copious amounts of ethanol and purified water, and returned to clean scintillation vials. 70 mg of ascorbic acid was added to the DMSO/water solution and stirred for 5 minutes before adding the solution to the vials containing the Au-SAMs. The vials were capped and stored in the dark overnight to allow the Cu click reaction to proceed, after which the Au-SAMs were removed from the DMSO/water solutions, and thoroughly rinsed with ethanol, dichloromethane and water, and then stored in clean dry scintillation vials in the dark until needed.

3.2.6 Electrochemical Methods

The electrochemical cell for analyzing the Au-Fc-SAMs is a Teflon cone with a hollow body, open at the top (~ 2-inch inner diameter) to accommodate a Teflon lid with holes for the graphite counter-electrode, and a AgCl reference electrode hanging into the electrolyte solution in the body of the cell. The bottom of the cone cell narrows to a tip, with an opening pressed against a Viton O-ring sitting on top of the Au-Fc-SAM sample for analysis. The inner diameter of the O-ring, 0.153 cm^2, defines the geometric surface area of the electrode. Electrical contact with the working Au electrodes is made using copper tape tapped to the Au sample sticking out from under the O-ring outside of the cone cell. The reference electrode was a custom made AgCl / saturated potassium chloride cell, with the AgCl coated Ag electrode housed in a glass body with a porous glass frit capping one end.

All electrolytes were sparged with nitrogen gas before the experiment for at least one-half an hour, and during the experiment, the solution was blanketed with nitrogen gas through one of the lid holes. Electrochemical measurements were made using either a Bio-Logic SP200 and SP300, or a VersaSTAT 3 potentiostat. Electrochemical peak area analysis was made using custom Python software written for electrochemical background correction described in Chapter 2, and for more routine measurements, the accompanying commercial software of the potentiostat.

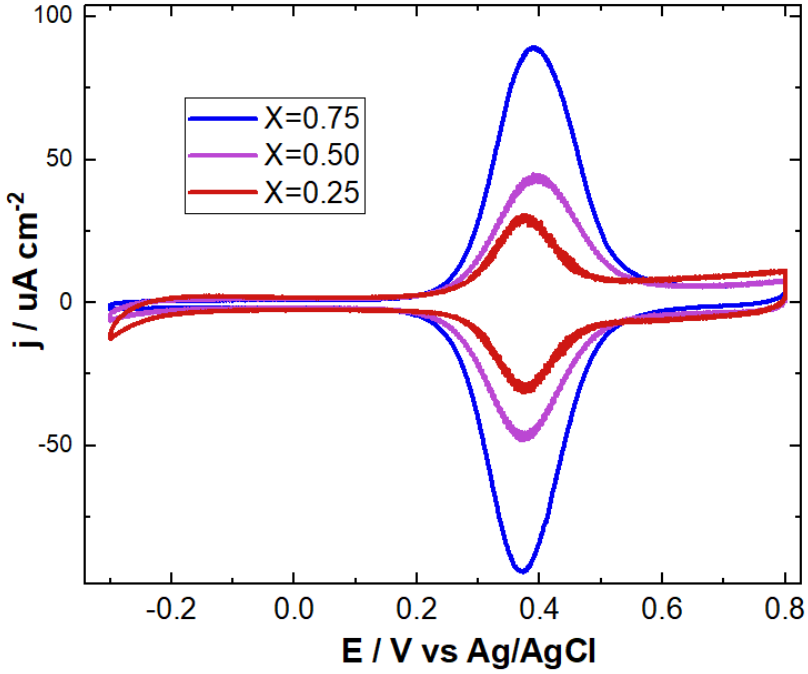

Figure 3-1 Representative CVs of mixed Fc-SAMs of different χ measured in 0.5 M perchloric acid. 0.3 V/s scan rate.

3.3 Results and Discussion

3.3.1 Cyclic Voltammetry of As-Prepared Fc-SAMs

Figure 3.1 shows the CVs of Fc-SAMs resulting from the mole fraction (χ) of azido-undecanethiol to decanethiol ratio in the ethanolic deposition solution. The average coverage values for χ each are listed in table 3.1 and are in agreement with previous works.[27] Coverage estimate were made using the geometric surface area defined by the Viton O-ring inner diameter (0.153 cm^2) placed between the Fc-SAM functionalized Au electrode and the Teflon cone cell.

Table 3-1 Coverage of ferrocene of Fc-SAMs vs azido-undecanethiol mole fraction measured via cyclic voltammetry.

χ, mole fraction of azido-thiol	**Ferrocene Coverage ($\times 10^{-10}$ mol cm^{-2})**
0.25	0.4 ± 0.2
0.5	1.7 ± 0.3
0.75	3.1 ± 0.8

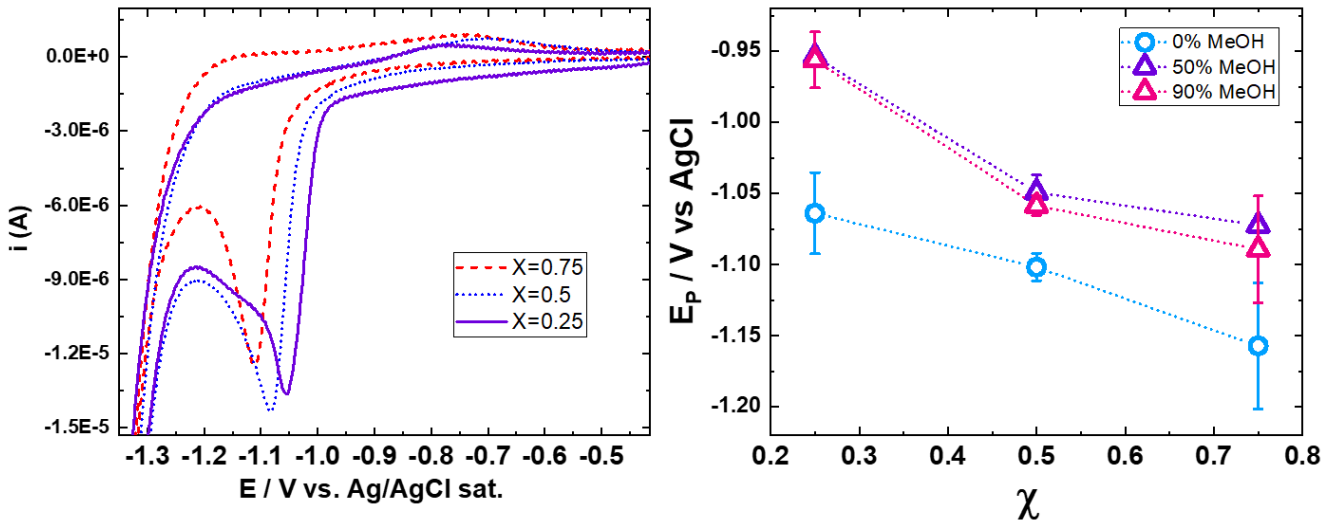

Figure 3-2 Left: Reductive desorption CVs of Fc-SAMs in aqueous 0.1 M aqueous potassium hydroxide, for different χ, the mole fraction of azido-undecanethiol in the SAM deposition solution. Right: E_P, desorption peak potential vs χ, taken in 0.1 M aqueous potassium hydroxide with 0%, 50% or 90% methanol content by volume.

3.3.2 Reductive Desorption CVs of Fc-SAMs

Mixed Fc-SAMs reductive desorption CVs were taken in 0.1 M potassium hydroxide aqueous solutions to confirm the χ coverage dependence as has been previously observed in other work. Figure 3-2 shows a more negative CV desorption peak (**E_P**) correlated with increasing mole fraction and coverage of Fc-thiol relative to the diluent decanethiol. With increasing χ, the length of the alkyl chains increases on average, which correlates with more negative E_P in both binary[28] and single-component SAMs.[29] The desorption CVs were also taken in mixed methanolic/aqueous 0.1 M potassium hydroxide at 50% and 90% methanolic components by volume to see effect of the χ dependence. Both pure aqueous and methanolic electrolytes exhibit a similar χ dependence, which shows that SAM structure similarly effects desorption peak potentials in methanolic electrolytes. In another report, the ΔG of alkanethiol absorption increased from -1.02 kcal/mol per CH_2 in pure aqueous hydroxide to -0.45 kcal/mol per CH_2 in methanolic hydroxide, by a weakening of the hydrophobic effect from the increased solubility in methanol.[30] Increasing the ΔG of adsorption should shift SAM surface coverage towards zero after applying reductive potentials < E_P.

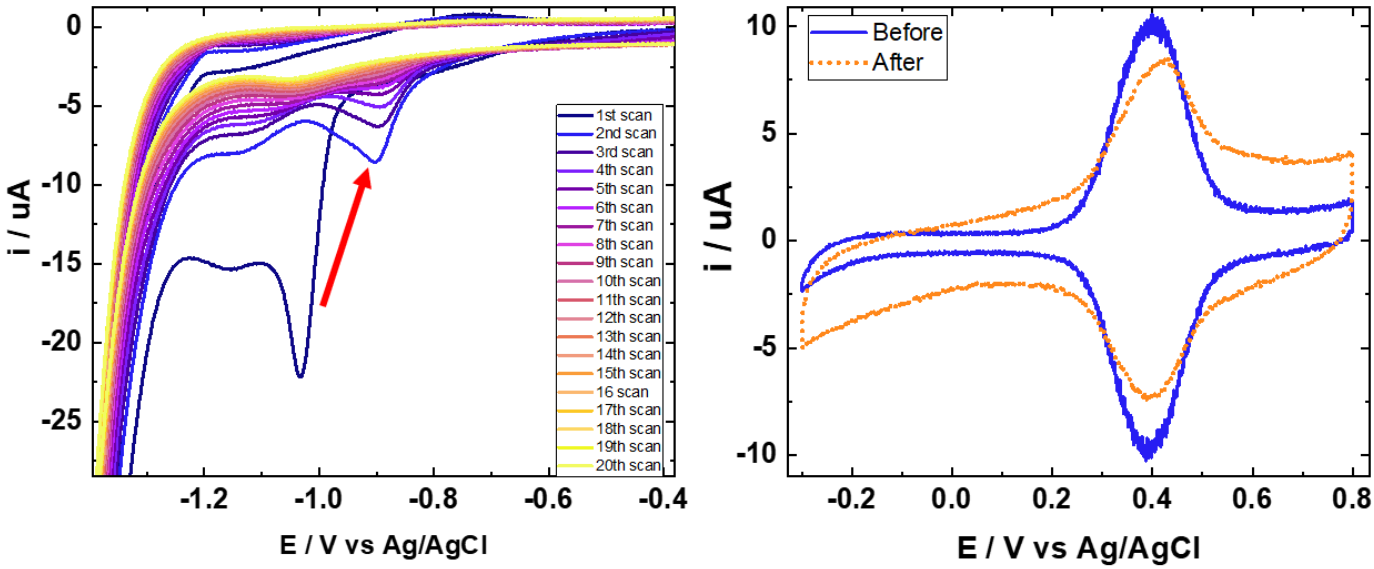

Figure 3-3 Left: 20 consecutive reductive desorption CVs of a mixed χ=0.75 Fc-SAM in aqueous 0.1 M potassium hydroxide from 0 V to -1.4 V vs AgCl. Scan rate 100 mV/s. The red arrow points in the direction of the changing desorption peak with successive scans. Right: CVs of ferrocene peaks of Fc-SAM used in left panel, before and after 20 reductive desorption CV sweeps. CV was measured in 0.5 M perchloric acid. 300 mV/s scan rate.

Figure 3-3, right, confirms that Fc-SAMs are retained at the electrode surface in aqueous electrolyte at potentials negative of the cathodic peaks observed in the desorption CV cycles. After 20 scans cathodic sweeps, approximately 62% of the original Fc peak remained, in contrast to the 92% remaining peak remaining after one cathodic sweep used in another study.[10] In figure 3-3, left, a clear desorption peak (E_P) is observed on the first scan of the desorption CV, and remains above the background currents until the 10^{th} or 11^{th} scan, decreasing in magnitude upon each cycle until it disappears. E_P shifts positive ~ 100 mV after the first scan indicating a change in the packing and structure of the SAM upon reductive cleavage and re-adsorption at positive potentials. At the end of the scans, the presence of the Fc peak, coupled with the disappearing desorption peak suggests that the structure of the Fc-SAM after repeated desorption CV cycles may no longer include direct sulfur interactions with the Au surface, but more physiosorbed type structures.[16] Two hypotheses to explore are that (i) Fc-SAMs will desorb more completely given enough time at a reducing potentials, or (ii) that the Fc-SAMs coverages at reducing potentials are time independent and that potential is only important parameter. The latter was explored next using chronoamperometry, where the potentials is held constant and the current is observed, to determine the effect of potential at a given time.

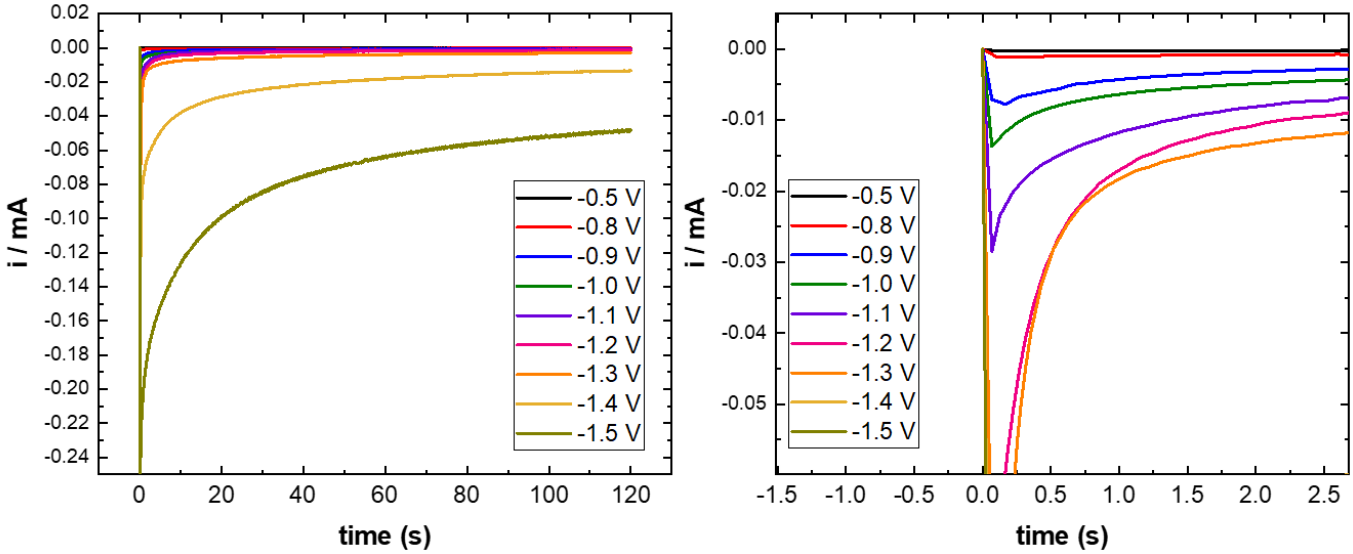

Figure 3-4 Left: Data from 2-min reductive chronoamperograms of $\chi = 0.75$ Fc-SAMs in aqueous 0.1 M potassium hydroxide. Right: Same as left but zoomed in on features within the first 3 seconds.

3.3.3 Desorption Chronoamperometry in Alkaline Aqueous Electrolyte

To investigate the effect of applied potential for a constant time interval on the coverage of Fc-SAMs in aqueous 0.1 M potassium hydroxide, two-minute long chronoamperometry (CA) measurements were chosen for exploratory analysis. For each sample, the Fc-SAM coverage was measured using CV in 0.5 M perchloric acid, after which the acid was removed from the cell, rinsed thoroughly with pure water, and then filled with 0.1 M potassium hydroxide. In the hydroxide solution, a potential was applied to the Fc-SAM electrode during a two-minute CA where presumably some of the Fc-SAM is reductively desorbed, after which the hydroxide solution was removed and the cell was again rinsed thoroughly with pure water. After rinsing the cell, perchloric acid was returned to the cell, and the remaining Fc coverage was measured once more to determine the effect of the potential perturbation on the Fc-SAM coverage. For each sample, only one applied reductive potential was applied. A final experiment was performed on the samples after the measurement of the Fc coverage where the defect sites in the SAM were backfilled with decanethiol to fill in the exposed gaps after desorption, but the results of this side experiment are reserved for a separate discussion in another section below with more detail.

Figure 3-4 shows the current decay transients from the reductive potentials applied to χ=0.75 Fc-SAMs for two-minutes, an initial spike or peak in the current which decays to a steady baseline, although incompletely for the more negative potentials, given the length of time chosen here. The larger currents in -1.4 V and -1.5 V CAs are from the hydrogen evolution reaction (HER), which can be seen at potentials negative of the desorption peak in the reductive CVs. In the CAs, the asymmetric current “peaks” at more negative potentials are similar to the shapes observed in Yang and Morins paper on alkanethiol desorption CAs for longer alkanethiols, but

decay at much slower rates than presented in their paper, suggesting a slower growth of "etching center" perimeters, and the creation of a larger number of "etching centers" according to their model for longer alkyl-chain lengths and more negative potentials.[31] No attempt to model the CAs using Yang and Morin's model was made for this study, but instead more attention is given to the measurement of the Fc peak areas after the reductive CA as a function of applied potential.

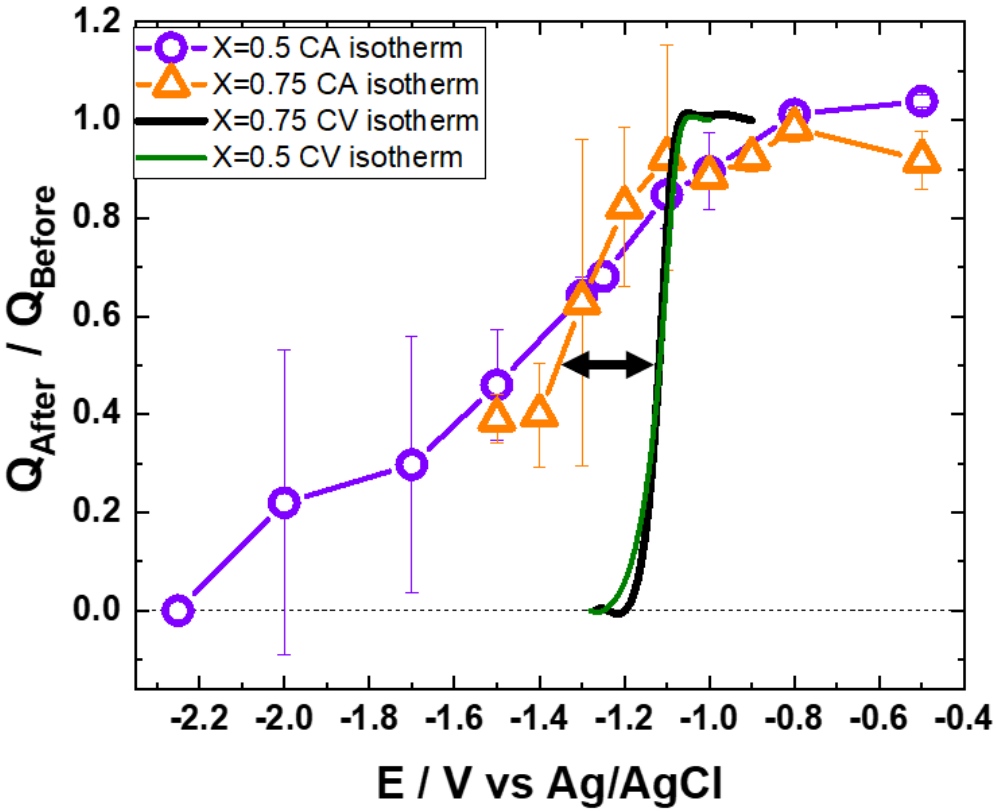

Figure 3-5 CV and CA derived isotherms from aqueous 0.1 M potassium hydroxide.

3.3.4 Desorption Isotherms Resulting from Reductive Chronoamperometry in Aqueous 0.1 M Hydroxide Electrolyte

Fc peak areas (charge) measured after the reductive CAs in aqueous 0.1 M potassium hydroxide at various potentials is plotted in figure 3-5, normalized by the Fc peak area before the applied reductive potential, denoted as Q_{after}/Q_{before} in the figure, which represents the fraction of remaining Fc on the surface after the applied potential of reductive CA. To make visual comparison of the Fc ratios after the CAs to the desorption peak potentials (E_P) in the reductive CVs, figure 3-6 shows how the reductive CV peaks can be transformed from the current-potential values to normalized charge ratios, which represents the ratio of coverage at potential E to the initial total coverage, which requires the assumption that the SAM desorption is fast and irreversible during the reductive CV. The value Q_E represents the charge passed to the thiols in the desorption CV from the onset of the peak up to potential E. This value is normalized by the total charge under the peak, Q_{Total}. SAM coverages were historically estimated using Q_{Total} until Lipkowski showed that this method introduces systematic error due to inaccurate background charging estimates.[32] Estimated coverages using Q_{Total} from the method shown in figure 3-5 yielded Fc-SAM coverages from 0.7 to 1.2 nano-moles cm^{-2}, higher than the measured Fc peak coverages, which is expected, due to the charges passed to the diluent thiol, decanethiol, present on the surface with the Fc-terminated thiols, and the crude method of backgrounding using splines. The CV derived desorption isotherms show inflection points at Q_E/ Q_{Total} of ~ 0.5 coincide approximately with the CV desorption peak potential E_P.

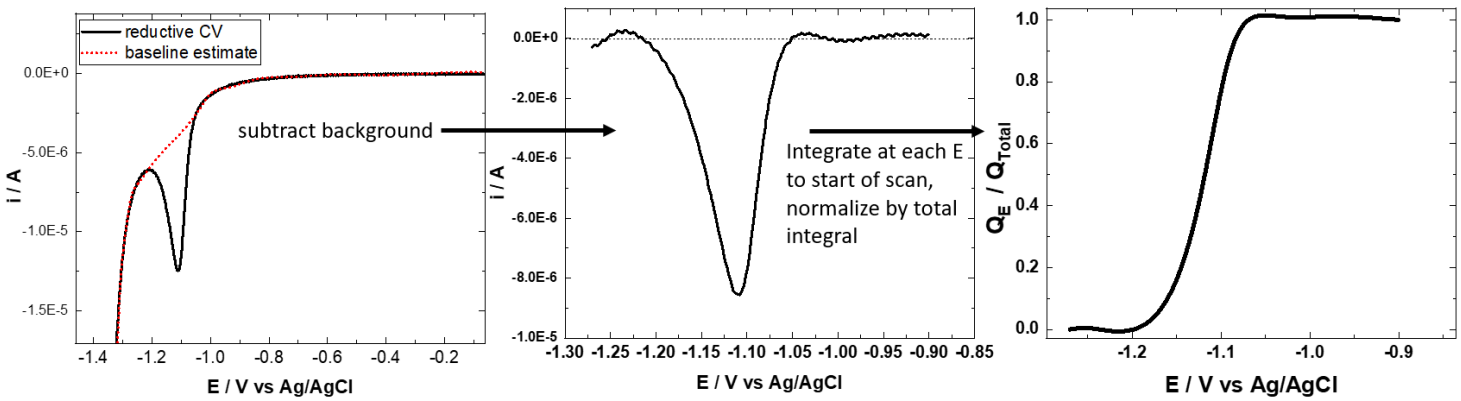

Figure 3-6 Left: Representative reductive CV peak. Background estimated using a spline. Center: Results of subtracting the background estimate. Right: CV derived desorption isotherm as a result of the normalized cumulative integral from potential E to the beginning of the scan. Each Q_E is the charge passed under the reductive peak from the onset of the peak up to the potential E. This value is normalized by the total charge under the peak, Q_{Total}, which represents the total Fc-SAM coverage measured by the cathodic peak.

The CV derived isotherms are plotted alongside the isotherms derived from the Fc coverage after the two-minute CAs for comparison in figure 3-5 for χ=0.5 and χ=0.75. The CV derived isotherm predicts Fc-SAM coverages of zero at potentials beyond -1.2 V. In contrast, the CA derived isotherms show coverages of 60% to 80% in the same range and 80% to 90% in the range of the CV derived isotherm inflection points where ~ 50% coverages are expected. The double-arrow in figure 3-5 shows that -250 mV to -300 mV more negative potentials than E_P were required to reduce the Fc coverage by 50%. Recall that significant HER current onset begins at -1.3 V of which the non-polar H_2 bubbles may help facilitate movement of the reduced Fc-thiols away from the surface as others have suggested. Only at extreme overpotentials of -2.2 V was a Fc free surface CV observed after the reductive CA, which is shown in figure 3-7. A working hypothesis up to this point is that the low-solubility of the Fc-SAMs significantly hinders their ability to rapidly dissolve into purely aqueous bulk electrolytes, assuming that the description of the electrochemical cleavage of the Au-S bond postulated in the literature is accurate. This suggests that using less polar electrolytes should shift towards more rapid dissolution upon applying potentials that coincide with the CV desorption peak. However, before jumping straight to the use of methanolic electrolytes to probe Fc-SAM desorption, as series of CA experiments using hydrodynamic flow was conducted using rotating disk voltammetry in pure aqueous hydroxide solutions, to see if more dissolution can be achieved by forced convective flow of the electrolyte over the electrode surface.

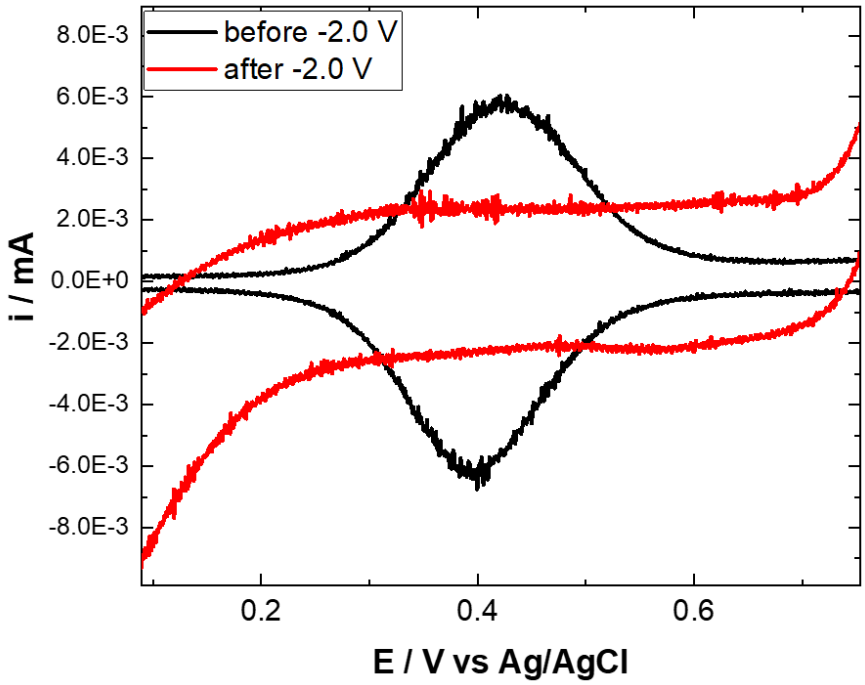

Figure 3-7 CV of Fc peaks of Fc-SAM after the application of -2 V vs AgCl in aqueous hydroxide showing complete loss of the Fc peak.

3.3.5 Reductive Desorption Chronoamperometry with Forced Convective Flow in Aqueous and Methanolic Electrolytes

To see if forced convective hydrodynamic flow over the electrode surface would remove the reduced Fc-thiols from the surface at reductive potentials more efficiently than quiescent solutions, χ=0.5 Fc-SAMs were deposited on 5 mm diameter Au rotating disc electrodes (RDE), and reductive CA experiments were performed at -1.3 V vs AgCl with various rotation rates to see if the coverage changed with rotation rate. With RDE experiments, the electrode disc rotates in the electrolyte which creates directed flow from the bulk electrolyte towards the electrode surface normal, which radiates outward from the center of the electrode.[23] This reduces the thickness of the diffusion layer at the electrode surface, with the hypothesis that as the thiols diffuse through a shallower diffusion layer, they will be rapidly swept away from the surface into the bulk electrolyte by the radial flow pattern outside of the diffusion layer, and shift the equilibrium towards more desorption. The resulting bulk thiol concentration would be infinitesimal. Figure 3-8 shows the Fc-SAM coverage ratio after two-minute desorption CAs (-1.3 V) at various rotation rates, which shows no effect from increasing the rotation rate at the two-minute time scale. This experiment was repeated at -1.3 V at 3000 rpm, but with increasing the volume percent of methanol in the 0.1 M potassium hydroxide, and the results (3-8, right) show a clear decrease in Fc coverage with increasing methanolic content. Although this shows an interpretable trend with respect to methanol content, using the same potential (-1.3 V) in the different electrolyte does not make them perfectly comparable due to the extra-thermodynamic assumptions required when comparing potentials in different electrolytes. To further explore the relationship of the methanol content in removing Fc-SAMs at reductive potentials coinciding

with CV desorption peaks, CA desorption isotherms were constructed using the same techniques in section 3.4.3 and 3.4.4.

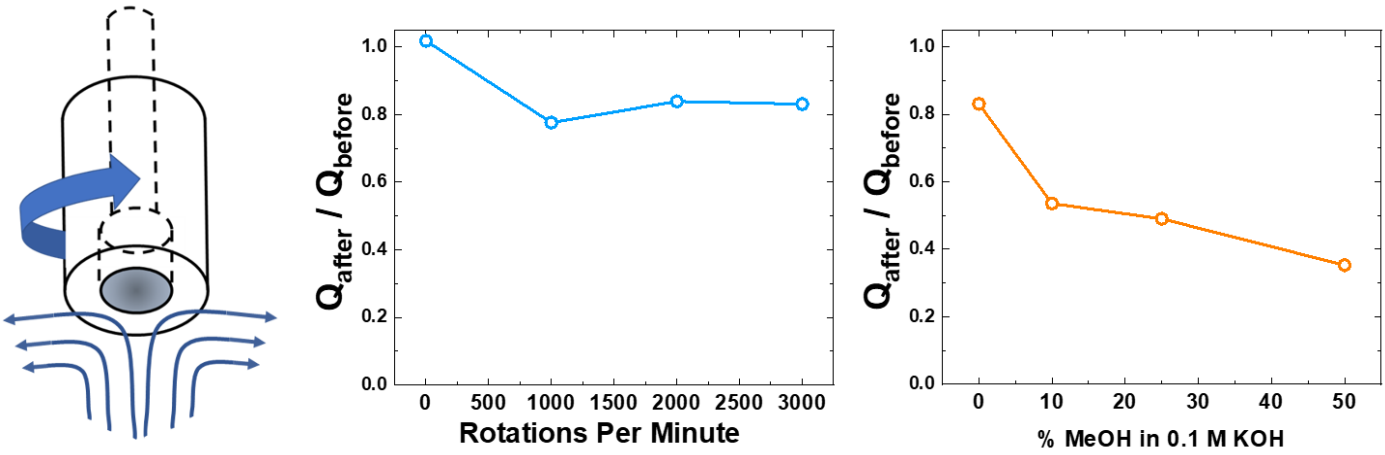

Figure 3-8 Left: Cartoon of a rotating disk electrode and the liquid flow profile introduced at the surface of the electrode. Center: Fc-SAM coverage ratio vs rotation rate while applying -1.3 V vs AgCl using RDE. Right: Fc-Sam coverage ratio after desorption CAs at -1.3 V using RDE with 3000 rpm in various potassium hydroxide solutions with increasing methanolic percent by volume.

3.3.6 Reductive Chronoamperometry and Derived Isotherms in Methanolic 0.1 M Hydroxide Solutions

To test if decreasing the polarity of the electrolyte would shift the CA derived isotherms closer to the shape and potentials of CV derived isotherms, mixed methanolic/aqueous 0.1 M potassium hydroxide was prepared with 50% and 90% methanol by volume. First the Fc-Sam coverage was measured in 0.5 M perchloric acid, then removed and the cell rinsed, after which the methanolic hydroxide solution was added to the cell for a two-minute reductive CA. At the end of the CA, the methanolic electrolyte was removed from the cell, thoroughly rinsed with pure water, and perchloric acid returned to the cell to measure the remaining Fc peaks. Figure 3-9 shows example CAs in 90% methanolic hydroxide with χ=0.75 Fc-SAMs, which shows at potentials of -0.95 V and -1.0 V, the growth of a peak over the first few seconds which then decays. The growth of a peak at -0.95 V takes longer to reach its apex than the peak at -1.0 V and more negative potentials, which according to Yang and Morin's nucleation and growth model, is indicative of growth in size of "etching centers" within the film.[31] This was not observed in the pure aqueous electrolytes above which suggests different time scales for the etching rates in aqueous vs methanolic electrolytes. The peak becomes sharper and more asymmetric at more negative potentials as the mechanism changes from the growth of the "etching centers" to a large increase in the number of "etching centers" as the driving force for ion penetration into the film increases with more negative potentials according to Yang and Morin's model.[31]

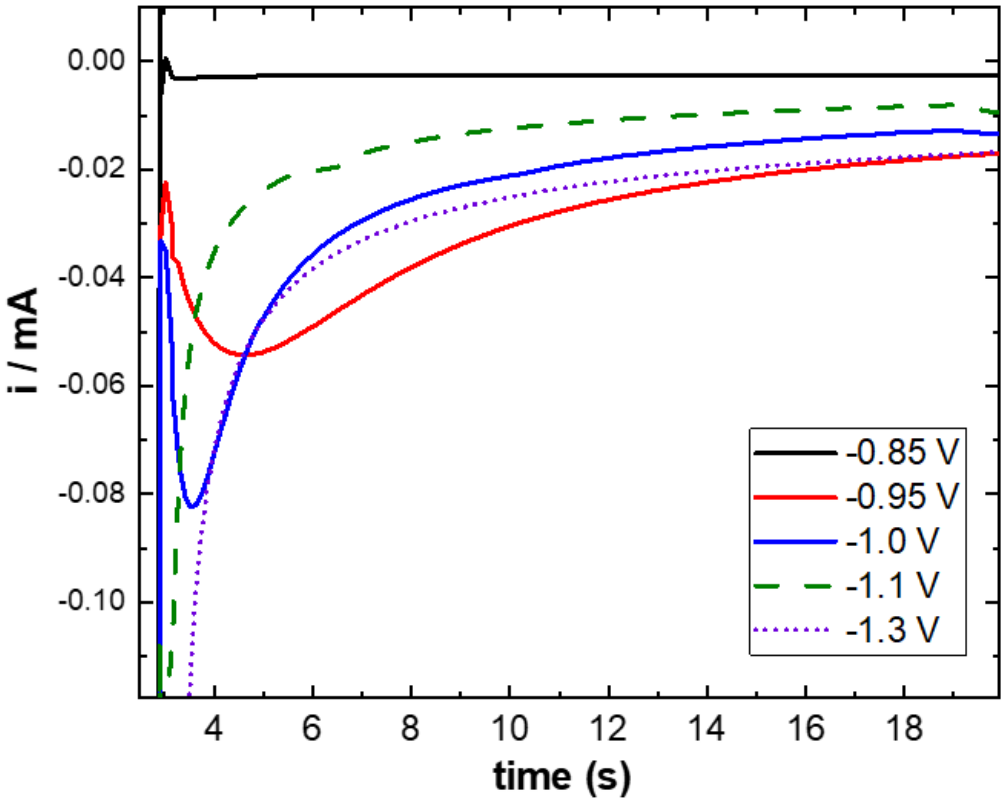

Figure 3-9 Reductive chronoamperograms of χ=0.75 Fc-SAMs in 90% methanolic 0.1 M potassium hydroxide.

Figure 3-10 shows the CA derived isotherms for χ=0.5 and 0.75, which are constructed using the normalized Fc coverages after desorption, compared to the CV derived isotherm which uses the integrated charge in the cathodic peaks observed in the reductive CVs. In 3-10 left, the χ=0.75 coverage drops to approximately 60% at potentials close to the inflection point of the CV derived isotherm in 50% methanolic electrolyte, a 20% decrease compared to the pure aqueous counterpart in figure 3-6 above. For χ=0.5, an even greater drop to ~ 45% of its initial coverage is observed on average in 50% methanolic electrolyte. For figure 3-10 right for 90% methanolic hydroxide, both χ=0.5 and 0.75 CA derived isotherms have a nearly identical shape dropping to 50% of its initial coverage coinciding with the potentials near the inflection points of the CV derived isotherms, but show coverages around 20 to 30% where the CV isotherms predict coverages closer to zero.

To summarize the effect of using methanolic electrolytes vs pure aqueous electrolytes, figure 3-11 was constructed to highlight the differences between the electrolytes using the metric E_D-E_P, where E_D is the potential from the CA derived isotherms where the average coverage of the Fc-SAM has dropped to 50% of its initial value (extrapolated between data points), and E_P is the average reductive CV peak potential, which coincides with the inflection points of the CV derived isotherms at 50% coverage. A negative value for E_D-E_P indicates that the Fc-SAM coverage is higher than would be expected if relying on the reductive CV peaks to make a prediction, most likely caused by slow mass transfer from the electrode surface into the bulk electrolyte due to low solubility of the Fc-thiols. E_D-E_P in 3-11 shows a clear trend with increasing values from -270 mV to 38 mV. In methanolic electrolytes, the coverage of the Fc-SAMs vs applied potential provides information consistent with coverage predictions from the

reductive desorption peaks, while in aqueous electrolytes, relying on the coverage measurements alone gives a distorted view of the reductive stability of the film within the 250-mV range between E_D and E_P, of which other clues, such as increase in the background charges, paints a picture of reductive instability in this range.[33]

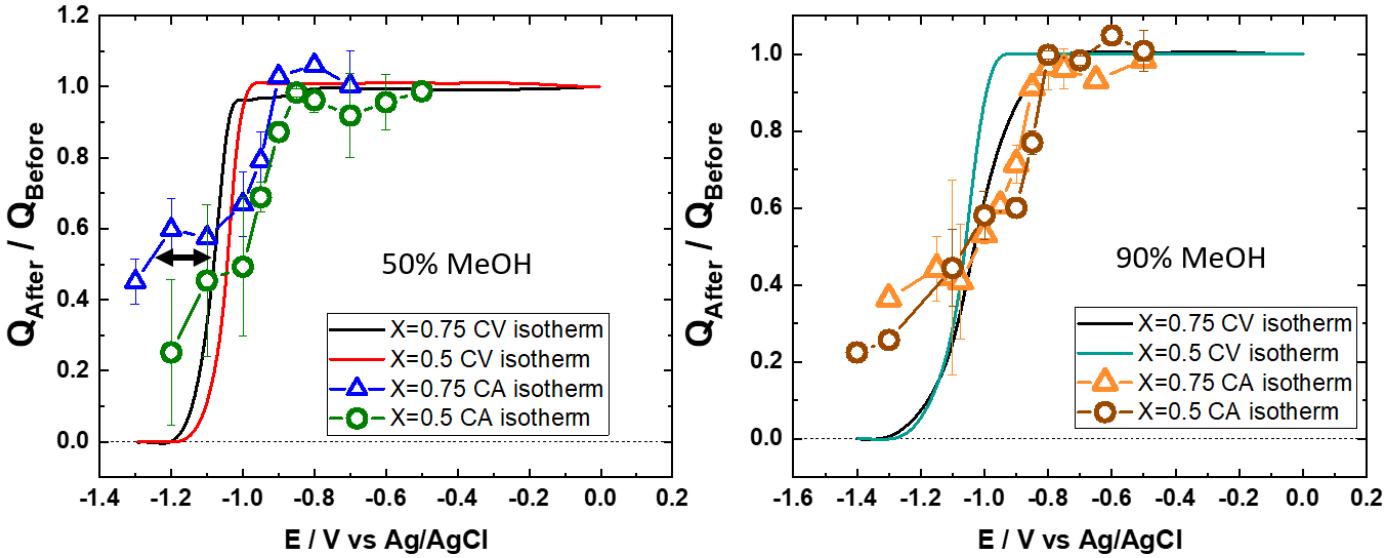

Figure 3-10 CA and CV derived isotherms for χ=0.5 and 0.75 in 50% and 90% methanolic 0.1 M potassium hydroxide.

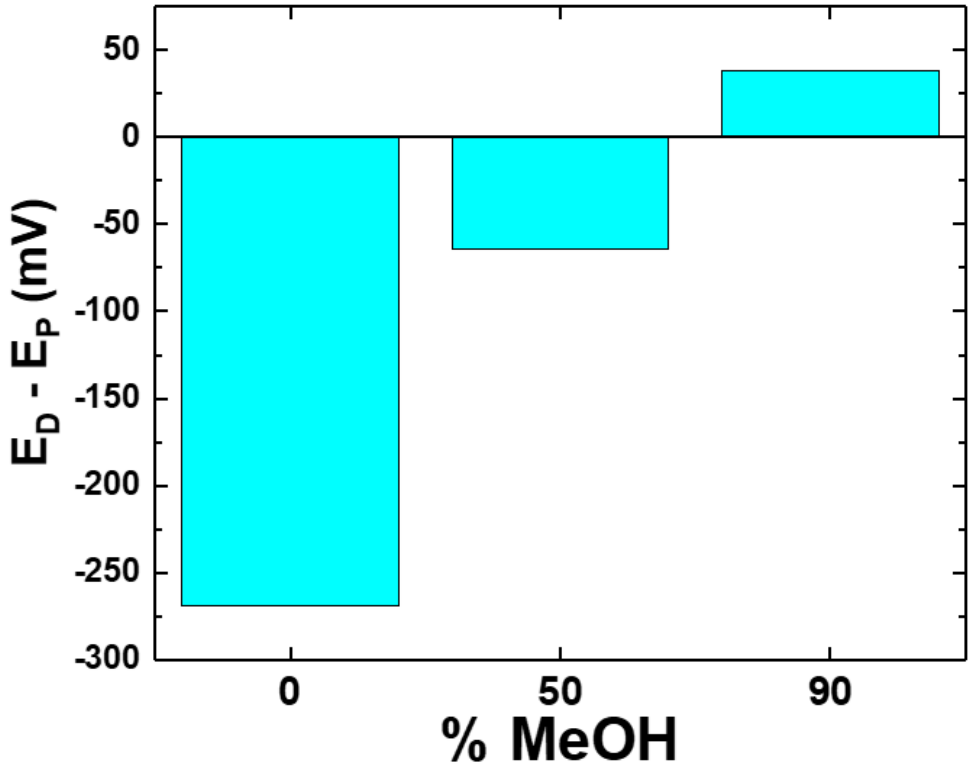

Figure 3-11 E_D - E_P for Fc-SAMs vs percent methanol in 0.1 M potassium hydroxide. E_D is the potential where the CA isotherms shows a 50% loss in coverage, and E_P from the reductive CVs, is the cathodic peak potential, and the potential where 50% of the film has been reduced and cleaved from the surface. E_D - E_P highlights the difference in the two methods in interpreting the Fc-SAM stability. E_D - E_P shown here are the average values from both χ=0.5 and 0.75 Fc-SAMs.

3.3.7 Exploring Time Dependence at Constant Potentials on Fc-SAM Coverage using Chronoamperometry in Aqueous and Mixed Aqueous Methanolic Electrolytes

To explore time dependence of Fc-SAM mass transfer away from the electrode surface at reductive potentials close to the desorption peak, a series of experiments were conducted with reductive CAs using time as the variable while keeping potential constant in 0%, 50% and 90% methanolic 0.1 M potassium hydroxide electrolytes. The same procedure for the CA derived isotherms was used with measurement of the Fc-SAM coverage before and after the reductive CA. The applied potential was -1.13 V for 0% methanol solutions and -1.12 V for 50% and 90% methanol solutions, with times ranging from 10 seconds to 1 hour. Figure 3-12 shows the results. For 0% methanol electrolyte, the coverage drops rapidly within 500 seconds and then appears o equilibrate with the coverage of roughly 66% its initial value, which is 15 to 20% lower than what was reported at for two-minute isotherms at comparable potentials in figure 3-6. For 50% and 90% methanolic solutions, the time dependence is apparent over the entire span of an hour with decreasing Fc coverage at longer times at reductive potentials. Pesika et al proposed a model of SAM reductive desorption where upon reductive cleavage of the Au-S bond, the rate of loss of the SAM is linearly dependent on the square root of time, a hallmark of a diffusion process, and that the rate of diffusion was governed by the bulk solubility which shows up in the slope of the linear model.[7] Of the 3 curves presented here, only the 90% methanol time-dependent curve showed reasonable linearity with $s^{1/2}$ (R^2=0.911, right figure in 3-12), but compared to the R^2 of other linearized models in electroanalytical chemistry, this data is not sufficiently explained by the model. To further compare time dependence, the CA derived isotherms in 90% methanolic electrolyte were taken again but using one-hour long time intervals

instead of two minutes, shown in figure 3-13. Figure 3-13 shows that the hour-long reductive CVs isotherm is shifted positive relative to the 2-minute isotherm, and the CV isotherm derived from the CV cathodic desorption peak. It has previously been shown that CV desorption peaks are distorted at fast scan rates, and shift positive with slower scan rates, which gives the system time to equilibrate and approach the thermodynamic equilibrium. Using longer times in the reductive CAs has a similar effect, but note that there is still ~ 25% coverage measured at -1.4 V where complete desorption is expected from the CV isotherm. The key takeaway is that measurement of SAM coverage is time-dependent and electrolyte-dependent at applied potentials associated with the cleavage of the Au-S bond.

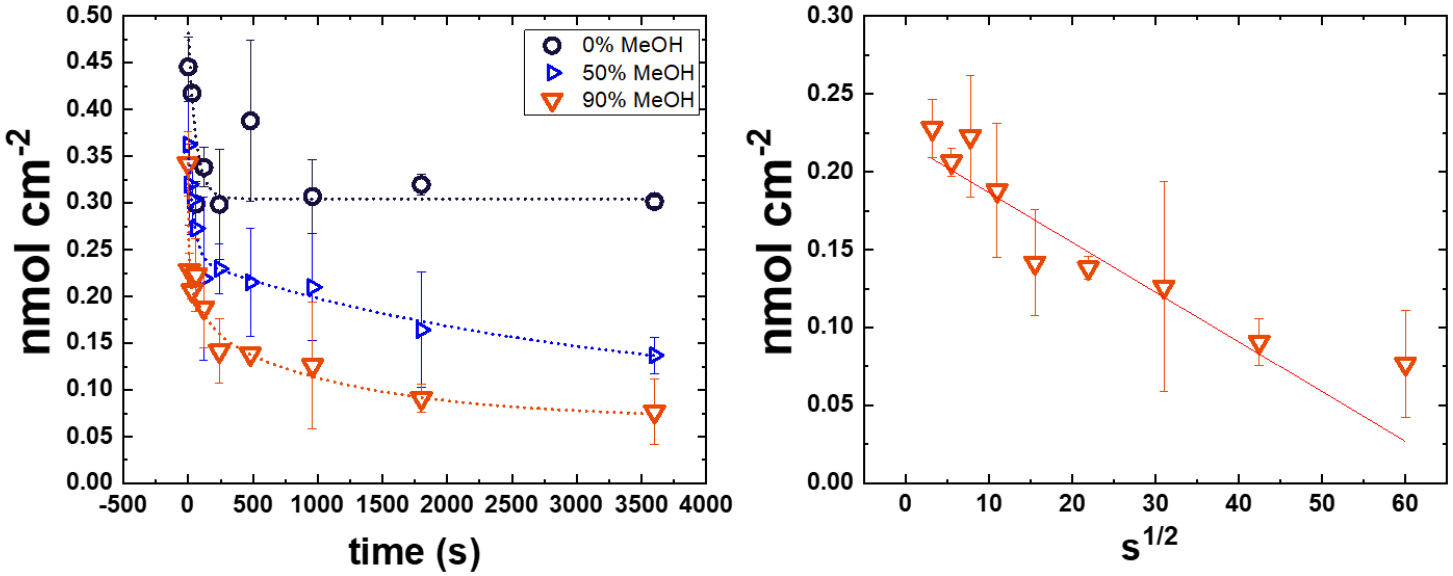

Figure 3-12 Right: Measurement of χ=0.75 Fc-SAM coverage as a function of time at a constant potential in 0%, 50% and 90% methanolic 0.1 M potassium hydroxide. Dashed lines are a guide for the eye. Left: Data from 90% methanol on right replotted vs the square root of time (s) to examine if data fits linear model proposed by Pesika et al.

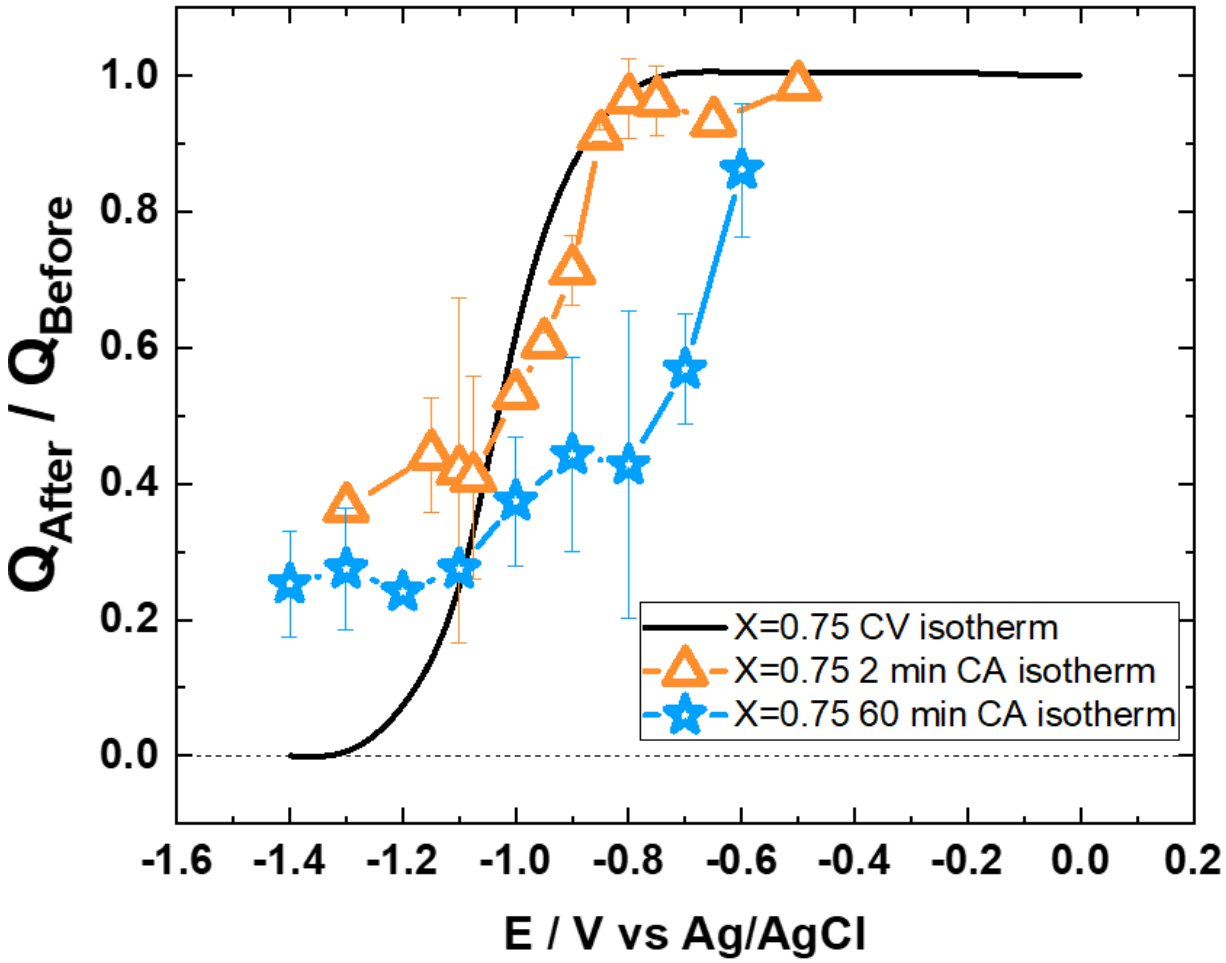

Figure 3-13 CA and CV derived isotherms for χ=0.75 Fc-SAMs in 90% methanolic 0.1 M potassium hydroxide. One set of CA isotherms taken from 2-minute CAs, and the other from 60-minute CAs.

3.4 Conclusions

Electrochemical reductive stability of mixed Fc-SAMs on Au electrodes was probed using cyclic voltammetry and chronoamperometry in aqueous and mixed aqueous methanolic potassium hydroxide electrolytes. The Fc peak was used to measure the coverage of the SAMs after reductive potentials were applied to the Fc-SAM electrode. In aqueous electrolyte, a significant portion of the Fc-SAM remained on the surface at potentials coinciding with the reductive desorption CV peak. Using chronoamperometry at potentials well-beyond the CV desorption peak, it was found that significant overpotentials of 250 mV or greater was required to see a significant drop in the Fc-SAM coverages. In contrast to the aqueous electrolyte, reductive desorption in 50% and 90% methanolic potassium hydroxide electrolytes show a more substantial loss in the Fc-SAM coverage at potentials coinciding with their CV desorption peaks measured with the same electrolytes. Time dependence at reductive potentials was also explored, which showed that most of the changes to the Fc-SAM coverage happened with 500 seconds in aqueous hydroxide and then the coverage remained stable and time independent up to an hour. Time dependence in methanolic hydroxide solutions saw a continual decrease in Fc-SAM coverage over the entire hour, which shows that choosing shorter times at a reductive potential will bias the measurement towards higher coverages. This work is in qualitative agreement with in-situ spectroscopic measurements in other works which show that reductive desorption is a complex and incomplete process dependent on a myriad of factors, such as the SAM structure, surface and electrolyte interactions, and time at a given potential, but here it was shown with quantitative measurement of the Fc-SAM coverage. The key takeaway is that time and electrolyte composition are important parameters that are underexplored in assessing the

reductive stability of SAM systems under applied potentials, and shown here to have a direct quantitative effect on the coverage measurements.

3.5 References

(1) Salvarezza, R. C.; Carro, P. "The electrochemical stability of thiols on gold surfaces," *J. Electroanal. Chem.* **2018**, *819*, 234-239.
(2) Widrig, C. A.; Chung, C.; Porter, M. D. "The electrochemical desorption of n-alkanethiol monolayers from polycrystalline Au and Ag electrodes," *Journal of electroanalytical chemistry and interfacial electrochemistry* **1991**, *310*, 335-359.
(3) Kondo, T.; Sumi, T.; Uosaki, K. "A rotating gold ring–gold disk electrode study on electrochemical reductive desorption and oxidative readsorption of a self-assembled monolayer of dodecanethiol," *J. Electroanal. Chem.* **2002**, *538-539*, 59-63.
(4) Doneux, T.; Buess-Herman, C.; Lipkowski, J. "Electrochemical and FTIR characterization of the self-assembled monolayer of 2-mercaptobenzimidazole on Au(111)," *J. Electroanal. Chem.* **2004**, *564*, 65-75.
(5) Yang, D.-F.; Wilde, C.; Morin, M. "Studies of the electrochemical removal and efficient re-formation of a monolayer of hexadecanethiol self-assembled at an Au (111) single crystal in aqueous solutions," *Langmuir* **1997**, *13*, 243-249.
(6) Thom, I.; Buck, M. "Electrochemical stability of self-assembled monolayers of biphenyl based thiols studied by cyclic voltammetry and second harmonic generation," *Surf. Sci.* **2005**, *581*, 33-46.
(7) Pesika, N. S.; Stebe, K. J.; Searson, P. C. "Kinetics of Desorption of Alkanethiolates on Gold," *Langmuir* **2006**, *22*, 3474-3476.
(8) Fujii, S.; Murase, K.; Sugimura, H. "Multicycle Desorption-Adsorption Voltammetry for Self-Assembled Mixed Monolayer Containing Ferrocenylthiol Molecules: A Discussion on Molecular Interaction in the Mixed Layer," *Electrochemistry* **2007**, *75*, 523-527.
(9) Madueño, R.; García-Raya, D.; Viudez, A. J.; Sevilla, J. M.; Pineda, T.; Blázquez, M. "Influence of the Solution pH in the 6-Mercaptopurine Self-Assembled Monolayer (6MP-SAM) on a Au(111) Single-Crystal Electrode," *Langmuir* **2007**, *23*, 11027-11033.
(10) Lee, L. Y. S.; Lennox, R. B. "Electrochemical Desorption of n-Alkylthiol SAMs on Polycrystalline Gold: Studies Using A Ferrocenylalkylthiol Probe," *Langmuir* **2007**, *23*, 292-296.
(11) Thom, I.; Buck, M. In *Z. Phys. Chem.* 2008; Vol. 222, p 739.
(12) Lemay, D. M.; Shepherd, J. L. "Electrochemical fabrication of a heterogeneous binary SAM on polycrystalline Au," *Electrochim. Acta* **2008**, *54*, 388-393.
(13) Cai, X.; Baldelli, S. "Surface Barrier Properties of Self-Assembled Monolayers as Deduced by Sum Frequency Generation Spectroscopy and Electrochemistry," *The Journal of Physical Chemistry C* **2011**, *115*, 19178-19189.
(14) Pensa, E.; Vericat, C.; Grumelli, D.; Salvarezza, R. C.; Park, S. H.; Longo, G. S.; Szleifer, I.; De Leo, L. P. M. "New insight into the electrochemical desorption of alkanethiol SAMs on gold," *PCCP* **2012**, *14*, 12355-12367.

(15) Casanova-Moreno, J. R.; Bizzotto, D. "What Happens to the Thiolates Created by Reductively Desorbing SAMs? An in Situ Study Using Fluorescence Microscopy and Electrochemistry," *Langmuir* **2013**, *29*, 2065-2074.
(16) Jacob, J. D. C.; Lee, T. R.; Baldelli, S. "In Situ Vibrational Study of the Reductive Desorption of Alkanethiol Monolayers on Gold by Sum Frequency Generation Spectroscopy," *The Journal of Physical Chemistry C* **2014**, *118*, 29126-29134.
(17) Haag, A.-L.; Toader, V.; Lennox, R. B.; Grutter, P. "Selective in situ potential-assisted SAM formation on multi electrode arrays," *Nanotechnology* **2016**, *27*, 455501.
(18) Kemnade, N.; Chen, Y.; Muglali, M. I.; Erbe, A. "Electrochemical reductive desorption of alkyl self-assembled monolayers studied in situ by spectroscopic ellipsometry: evidence for formation of a low refractive index region after desorption," *PCCP* **2014**, *16*, 17081-17090.
(19) Stolar, R. B.; Guerra, E.; Shepherd, J. L. "The Influence of Thiolate Readsorption on the Quality of Mixed Monolayers Formed through an Electrochemcial Method," *Langmuir* **2015**, *31*, 2157-2166.
(20) Wong, S.-S.; Porter, M. D. "Origin of the multiple voltammetric desorption waves of long-chain alkanethiolate monolayers chemisorbed on annealed gold electrodes," *J. Electroanal. Chem.* **2000**, *485*, 135-143.
(21) Zamlynny, V.; Lipkowski, J. "Advances in Electrochemical Science and Engineering," *Diffraction and Spectroscopic Methods in Electrochemistry* **2006**, 315-376.
(22) Eckermann, A. L.; Feld, D. J.; Shaw, J. A.; Meade, T. J. "Electrochemistry of redox-active self-assembled monolayers," *Coord. Chem. Rev.* **2010**, *254*, 1769-1802.
(23) Bard, A. J.; Faulkner, L. R.; Leddy, J.; Zoski, C. G. *Electrochemical methods: fundamentals and applications*; wiley New York, 1980; Vol. 2.
(24) Everett, W. R.; Welch, T. L.; Reed, L.; Fritsch-Faules, I. "Potential-Dependent Stability of Self-Assembled Organothiols on Gold Electrodes in Methylene Chloride," *Anal. Chem.* **1995**, *67*, 292-298.
(25) Collman, J. P.; Devaraj, N. K.; Chidsey, C. E. "“Clicking” functionality onto electrode surfaces," *Langmuir* **2004**, *20*, 1051-1053.
(26) Brassard, C. J.; Zhang, X.; Brewer, C. R.; Liu, P.; Clark, R. J.; Zhu, L. "Cu(II)-Catalyzed Oxidative Formation of 5,5′-Bistriazoles," *The Journal of Organic Chemistry* **2016**, *81*, 12091-12105.
(27) Collman, J. P.; Devaraj, N. K.; Eberspacher, T. P. A.; Chidsey, C. E. D. "Mixed Azide-Terminated Monolayers: A Platform for Modifying Electrode Surfaces," *Langmuir* **2006**, *22*, 2457-2464.
(28) Kim, Y.-K.; Koo, J. P.; Huh, C.-J.; Ha, J. S.; Pi, U. H.; Choi, S.-Y.; Kim, J. "Adsorption behavior of binary mixed alkanethiol molecules on Au: Scanning tunneling microscope and linear-scan voltammetry investigation," *Appl. Surf. Sci.* **2006**, *252*, 4951-4956.
(29) Walczak, M. M.; Popenoe, D. D.; Deinhammer, R. S.; Lamp, B. D.; Chung, C.; Porter, M. D. "Reductive desorption of alkanethiolate monolayers at gold: a measure of surface coverage," *Langmuir* **1991**, *7*, 2687-2693.
(30) Hatchett, D. W.; Uibel, R. H.; Stevenson, K. J.; Harris, J. M.; White, H. S. "Electrochemical measurement of the free energy of adsorption of n-alkanethiolates at Ag (111)," *J. Am. Chem. Soc.* **1998**, *120*, 1062-1069.
(31) Yang, D.-F.; Morin, M. "Chronoamperometric study of the reductive desorption of alkanethiol self-assembled monolayers," *J. Electroanal. Chem.* **1998**, *441*, 173-181.

(32) Laredo, T.; Leitch, J.; Chen, M.; Burgess, I. J.; Dutcher, J. R.; Lipkowski, J. "Measurement of the Charge Number Per Adsorbed Molecule and Packing Densities of Self-Assembled Long-Chain Monolayers of Thiols," *Langmuir* **2007**, *23*, 6205-6211.
(33) Corthey, G.; Rubert, A. A.; Benitez, G. A.; Fonticelli, M. H.; Salvarezza, R. C. "Electrochemical and X-ray photoelectron spectroscopy characterization of alkanethiols adsorbed on palladium surfaces," *The Journal of Physical Chemistry C* **2009**, *113*, 6735-6742.

Chapter 4 Extending the d-Band Model to Describe Trends in Reductive Stability of Self-Assembled Monolayers on Metal Surfaces, and Preliminary *operando* EXAFS Measurements of Electrochemical Au-S Bond Cleavage

4.1 Preface

The following (unpublished) work is part of a collaboration between my advisor, Associate Professor Charles McCrory, and Professor Jim Penner-Hahn, who's writing, reputation and expertise landed a successful NSF grant to fund this work. In preparation of the grant, Charles helped me to filter out the less useful ideas, and guided me in developing a hypothesis about the connection between Nørskov's d-band model and the reductive stability of adsorbates on transition metal surfaces. Professor Penner-Hahn's renowned expertise in x-ray absorbance spectroscopy has been critical in designing the experiments. Included in this collaboration is research and beamline scientist Aniruddha Deb, who was taught me much about designing and building spectroelectrochemical cells for XAS, in which we spent many late nights together going over minute details to make sure dimensions were right. Aniruddha is responsible for processing and analyzing the data presented below, as well overseeing the data collection. Beamline scientist Ryan Davis of SLAC National Accelerator Laboratory is another invaluable collaborator, who developed the grazing incidence XAS technique used in this work, and designed the current iteration of the cell, along with Sarah Edwards (also of SLAC) who supplied us with detailed information about the previous cell construction. Credit also belongs to Lirong Shi, who is taking over my project upon my departure, who is responsible for putting together the latest iteration of the beamline cell used in this work.

4.2 Introduction

The identity of the metal on which self-assembled monolayers (SAMs) are deposited on has a large effect on their electrochemical reductive stability as measured by their desorption peak potentials (E_P) observed in cyclic voltammetry (CV) and other indirect estimates of potential dependent stability.[1,2] CV results from previous works show E_P of Ag-SAMs are more negative than on Au-SAMs[1,2], and more indirect measurements of Cu-SAMs[2] suggest that Cu-SAMs are more reductively stable than Ag-SAMs. Other works suggest that there is enhanced reductive stability on Ni[3], Pd[4,5] and Pt[5,6] relative to Au as well, but not all works are in agreement as they use a variety of indirect methods to estimate the potential limits of stability. While considering all of the different experimental approaches to assess SAM stability, it is worthwhile to examine the chemical properties of the metal-sulfur interactions that would predict stability trends for comparison to the data. Bjørk Hammer and Jens Nørskov's d-band model[7-9] offers a theoretical framework for predicting and interpreting trends in the chemisorption bond strength between transition metal surfaces and adsorbates, which will be shown below to have a correlation with existing trends in the published SAM reductive stability.

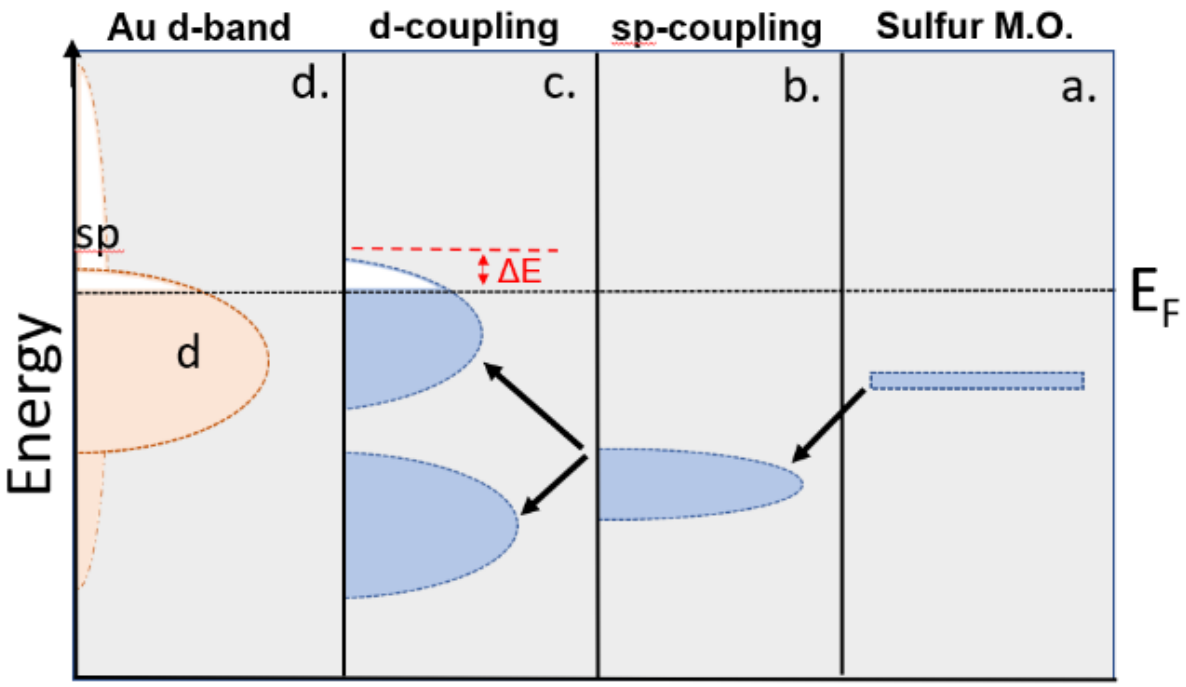

Figure 4-1Graphic model of d-band coupling of sulfur to a Au surface. In panel d. is the ½ filled sp band and nearly filled d-band density of states (DOS) of Au. Panel a. is the discrete isolated S molecular orbital energy before adsorption. Panel b. is the DOS after coupling to the sp band and panel c. is after coupling to the d-states giving rise to bonding and anti-bonding adsorbate states. ΔE is the minimum energy required to move E_F to fill the anti-bonding states. Figure adapted from reference 9.

4.2.1 The d-Band Model

Hammer and Nørskov developed the d-band model to describe a variety of adsorbate-surface chemical bonding models, of which the most relevant to SAM chemisorption is the radical-coupling mechanism[8,9] which has been invoked to describe the Au-S interaction.[10,11] In the d-band model for radical coupling of sulfur to transition metal surfaces, the strength of the chemical bond formed between the metal surface and the adsorbate is the result of the two interactions: 1) the coupling of the adsorbate molecular orbitals to the metal s and p bands (figure 4.1, panel a and b) to form an adsorbate band below the Fermi energy which Hammer and Nørskov describe as a "deep-lying filled bonding state and an empty antibonding state", and 2) interactions with the d-bands (figure 4.1, panel c) which give rise to anti-bonding and bonding states which determine the final strength of the bond.In the d-band model, for adsorbates such as oxygen and sulfur, the chemisorption energy of coupling to the half-filled s and p band is approximately the same among the noble metals on the order of -5 eV.[8] The main energy difference in chemisorption on different metals is caused by the anti-bonding states arising from interactions with the filled d-states. Noble metals on the right side of the periodic table have filled d-orbitals from which repulsive terms in the energy balance arise from the Pauli exclusion principle, described as an "orthogonalization energy penalty".[8] Hammer and Nørskov expand upon two trends which predict the chemisorption strength from the d-orbital interactions; 1) the fractional filling of the d-band from left to right along a row of transition metals leading to decreased stability, and 2) the spatially extended d-band states in 3d space moving down the columns for metals on the periodic table, weakening the surface bonds. For the first trend, the fractional filling of the d-band is described by the center of the d-band in relation to the Fermi

energy (figure 4.1, E_F); below which the d-band states are occupied and give rise to the adsorbate anti-bonding states. Moving left to right across a periodic row effectively moves the Fermi energy up in relation to the center of the d-band, which proportionately fills more of the anti-bonding states. The second trend moving down a group or column on the periodic table, the d-states are extended further into space, leading to greater overlap and therefore a larger orthogonalization penalty, weakening the surface bond, which explains why Au is the noblest metal, and does not form surface oxides, while Cu can form weak surface oxide bonds.[8] Hammer and Nørskov further explain why sulfur chemisorbs on Au while oxygen does not; sulfur orbitals are larger and have larger bond distances and therefore less overlap with d-bands making the orthogonalization penalty lower than oxygen. Oxygen has contracted orbitals and therefore requires a closer approach to form a bond with the sp band but a closer approach creates more overlap with the d-states, making the orthogonalization penalty high enough to nullify the bond formation. (A visualization of the distance vs bond energy for oxygen and sulfur on different metals is found in reference 8 on page 317).[8]

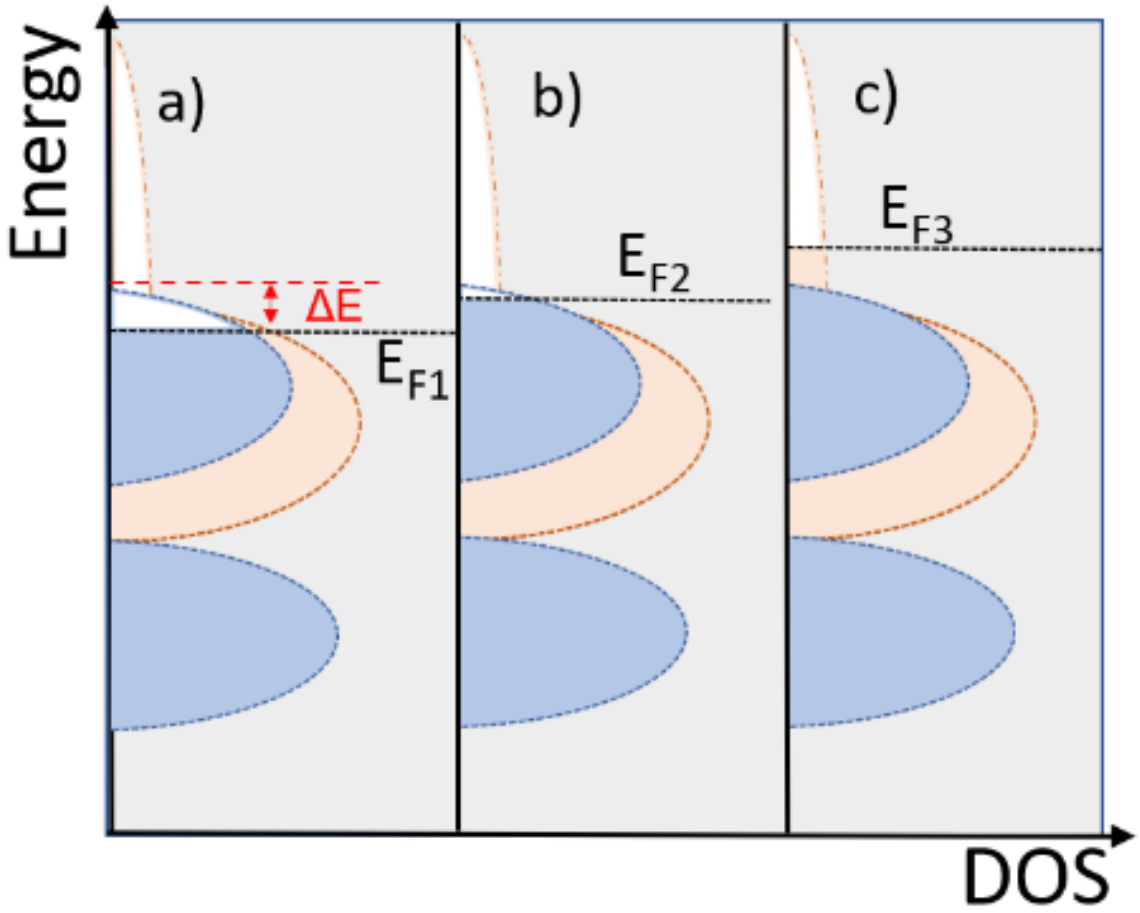

Figure 4-2 Graphic of d-band model a) Fermi level E_{F1} at open circuit potential, and the adsorbate bond has more bonding character than anti-bonding character. b) The electrode potential is lowered and the Fermi level is made higher (E_{F2}) filling more of the anti-bonding states and weakening the surface bond. c) The electrode potential is low enough that the surface bonds are fully broken when the Fermi level is at E_{F3}.

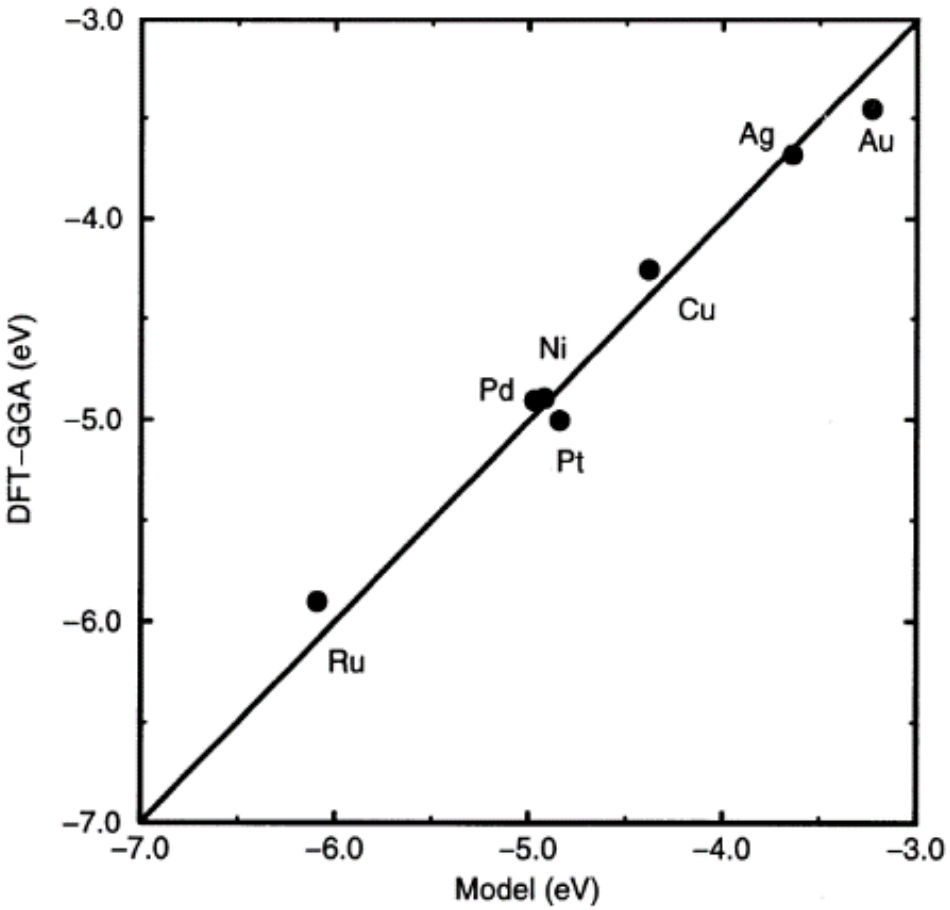

Figure 4-3 Nørskov's d-band model of S chemisorption energies vs DFT calculations, which shows a predicted ordering of the S-metal chemisorption bond strength. From reference 8 page 324.

4.2.2 Extending the d-Band Model for Predicting SAM Reductive Stability on Different Transition Metals

To extend the d-band model as a predictor for trends in SAM reductive stability on transition metals, the role of the Fermi energy in electrochemical experiments must be considered. In electrochemistry, changing the applied potential towards negative potentials increases the Fermi energy in the metal electrode, where the highest energy electrons in the electrode reside.[12] In the context of the d-band model, raising the Fermi energy effectively fills the anti-bonding adsorbate bands which cleaves the surface bond. The overpotential at which this occurs on a given metal will depend on the fractional filling of the d-band state, which is dictated by the chemical identity of the metal. Metals with lower fractional d-band occupancy at open circuit potential, where the Fermi level is below the center of the d-band, will have to raise the Fermi energy higher (more negative applied potential) to fill the anti-bonding states compared to metals where the Fermi level starts above the center of the d-band. In figure 4.2, the minimum energy required to fill the anti-bonding states is labelled ΔE and successively more negative potentials are applied raising the Fermi level. Based on this rationale, the d-band model predicts greater reductive stability for alkanethiol SAMs moving from right to left across a row on the periodic table, and likewise, the same trends moving up a group as the d-states are more contracted which lowers the orthogonalization penalty as described by Nørskov.[8] Comparing predictions from the d-band model chemisorption energy (Nørskov figure 4-3) with published measurements of hexanethiol SAM desorption potentials in figure 4-4, shows a striking correlation for Au, Ag and Cu in aqueous and methanolic sodium hydroxide.[2,8] The correlation is not as strong (or linear)

for group 10 elements (Ni[3], Pd[4], Pt[6]), where figure 4-3 predicts they have roughly the same chemisorption energy for sulfur, but instead a spread in E_P values is observed. Group 10 elements should also have more negative desorption potentials than Cu, Ag and Au according to the d-band model, but are more positive than Cu in figure 4-4. A complicating factor in this analysis is the use of varied and indirect measurements of potential-dependent stability for Pt, Pd, Ni and Cu, due to large hydrogen evolution currents which obscure CV desorption peaks that are commonly observed on Au and Ag.[2-4,6] Direct measurement of the metal-sulfur interactions as a function of applied potential would bring clarity in assessing the d-band model predictions. One method capable of direct assessment of metal-sulfur bonds is x-ray absorbance spectroscopy (XAS).

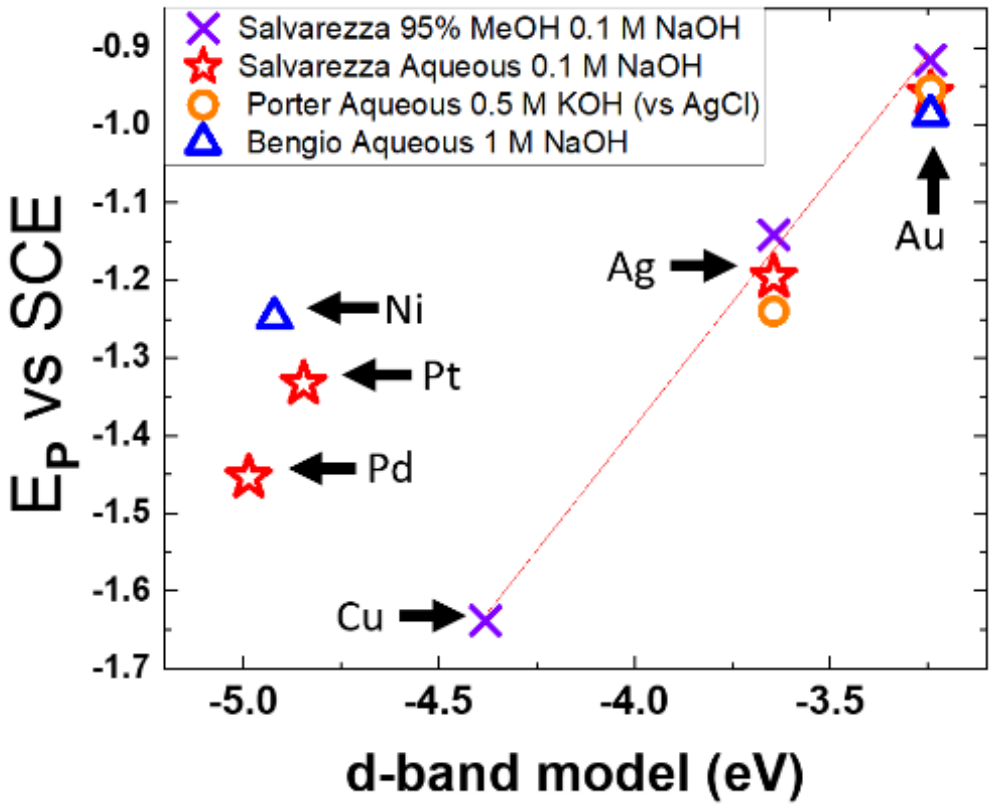

Figure 4-4 Reported desorption peak potentials for hexane-thiol SAMs (E_P) plotted as a function of calculated chemisorption energies for thiol-adsorbates on transition metal surfaces determined from Nørskov's d-band model (ref 8) of S chemisorption energy for transition metal surfaces (x-axis). Electrolyte conditions and authors are listed in the key for Au (ref 1,2),Ag (ref 1,2),Cu (ref 2), Ni (ref 3), Pd (ref 4) and Pt (ref 5).

4.2.3 Operando X-ray Absorbance Spectroscopy

X-ray absorbance spectroscopy is capable of measuring bond lengths between nearest neighbors in bulk materials at the angstrom scale, which in principle could detect changes in metal-SAM bond lengths from potential-dependent perturbations.[13,14] Recent work has focused on making XAS measurements on electrochemical surfaces possible through grazing angle techniques and electrochemical cell designs featuring thin electrolyte layers above the electrode surface, which minimizes unwanted attenuation of the incident x-ray beam from water.[14] In this preliminary work, the Au-S bond length of decanethiol SAMs on evaporated Au surfaces was probed as a function of applied potential in aqueous hydroxide electrolyte using x-ray absorbance fine structure (EXAFS) with a specially designed electrochemical cell.

In XAFS measurements, the energy of the incident photons (20-30 eV above the material absorbance threshold) ejects photoelectrons from the target atoms with a de Broglie wavelength on the order of the interatomic distances.[13] The photoelectrons are back-scattered by nearest neighbors, creating constructive and destructive waves depending on their wavelength induced by the incident photon energy.[13] The wave interference creates local minima and maxima in the photoabsorption cross-section depending on the photon energy, which produces an oscillating pattern in the fluorescence or absorbance intensity when plotted against the photon energy (eV).[13] The absorbance data is then normalized by the absorption cross-section in the absence of EXAFS effects, Fourier-transformed, and fit to a function which includes parameters for the number of scattering atoms and the absorber-scatterer distances, which are visualized as peaks vs radial distance from the atom being probed with x-rays.[13]

The absorber-scatterer distance between Au atoms and S atoms on the electrode surface will give direct information about the stability of the Au-S interaction as a function of potential in a reductive desorption experiment using EXAFS. In this preliminary work, a special electrochemical cell was designed to facilitate grazing-angle EXAFS measurements *operando* to directly measure changes the Au-S bond distance as a function of applied potential. This work lays the groundwork for future measurements which will probe metal-SAM interactions beyond Au surfaces to other metals such as Cu, Ni, Pt and Pd, to determine if these metals can be used to construct more reductively stable SAM systems.

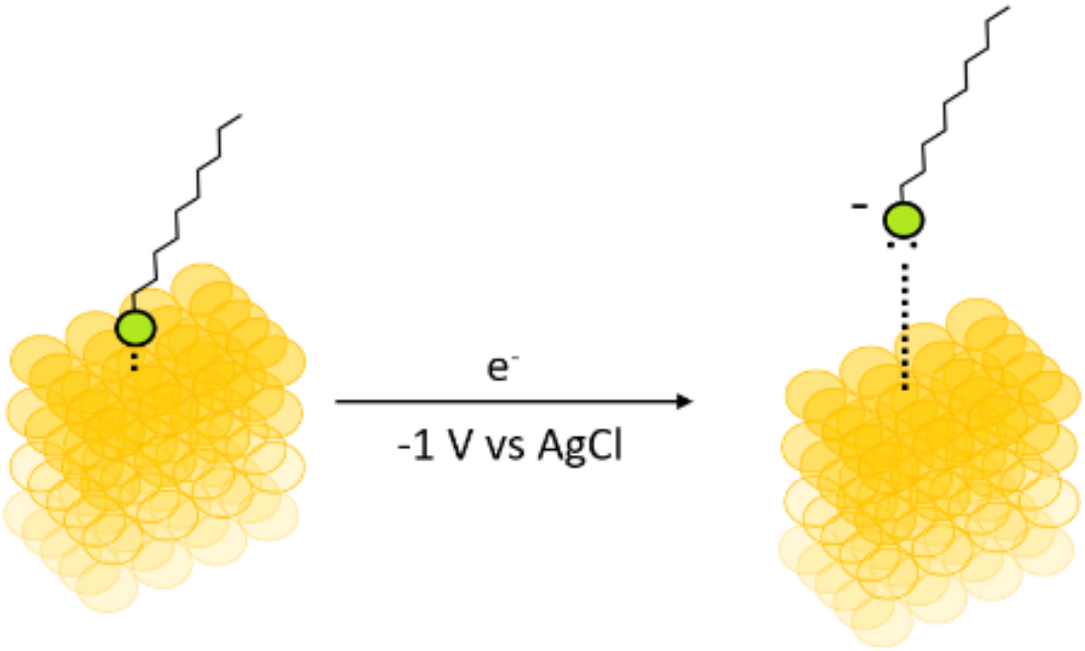

Figure 4-5 Cartoon of Au-S distance changing upon reductive desorption.

4.3 Experimental

4.3.1 Chemicals and Materials

Decanethiol (96%) were purchased from Alfa Aesar. Ethanol (200 proof, anhydrous) was purchased from Decon Laboratories. Gallium indium eutectic (99.99% metals basis) was purchased from Thermo Scientific. Potassium hydroxide (ACS reagent >85%, pellets) was purchased from Sigma Aldrich. Silicon wafers were purchased from University Wafers.

4.3.2 Evaporated Au Surfaces and SAM Deposition

Gold electrodes were prepared by physical vapor deposition of a 20-25 nm titanium adhesion layer followed by 200-250 nm of gold onto silicon wafers using an Angstrom Engineering Evovac Evaporator in the clean room at the Lurie Nanofabrication Facility. The Au covered wafers were covered with a protective semi-conductor grade dicing tape before being cut into 5 mm by 5 mm coupons using an ADT 7100 Dicing Saw.

Electrical connection to the back of the Au coupon was established by scratching away the oxide layer on Si side with a diamond-tipped scribe and simultaneously introducing a drop of indium gallium eutectic into the scratched area. A Cu wire was pressed into the eutectic area and a dab of silver paint was added to the contact point with the wafer to increase the surface area of conductive contact. The Cu wire was supported from above while a drop of epoxy cured and sealed the contact point over night.

The protective dicing tape was removed from the Au coupons after the attachment of the Cu wire back connection, and the adhesive residue was removed with repeated isopropanol,

acetone and water rinses. The cleaned Au surfaces were exposed to 1 mM decanethiol in ethanol in a centrifuge tube in a hanging meniscus configuration to prevent the thiol/ethanol solution from dissolving the back connection to the Cu wire. The thiol deposition proceeded overnight after which the Au-SAM surface was rinsed with ethanol and pure water to remove physisorbed thiols.

4.3.3 Operando Electrochemical Flow Cell

The custom-designed electrochemical cell was 3D printed by ProtoCafe. The cell material is a blend of urethane oligomers. The cell design (figure 4-4) feature 3 main parts: the cell body, the sample holder and the lid. The Au-SAM sample is fixed to the top of sample holder with epoxy, with the Cu wire back connection exiting the shaft in the sample holder to allow electrical contact. The sample holder holds the Au-SAM sample above the body with a lid height that restricts the electrolyte to a thickness of 10 μm with an x-ray transparent window made of Kapton above the sample surface. The lid design for the Kapton window exposes the side profile of the sample to the x-ray beam path for grazing incident angles. For the counter-electrode, a 200 μm diameter Pt wire is looped around the sample-holder beneath the surface of the sample out of the path of the x-rays in the lid chamber, and is fished through channels in the lid to the exterior of the cell for electrical contact. The body of the cell features 2 channels that connect to HPLC pumps at the bottom of the cell; with one channel working as the inlet for pumping electrolyte over the surface of the sample, and an outlet channel for electrolyte outflow. A third channel intersects the inlet channel to allow a 1 mm diameter leakless AgCl reference electrode to contact the flowing electrolyte solution.

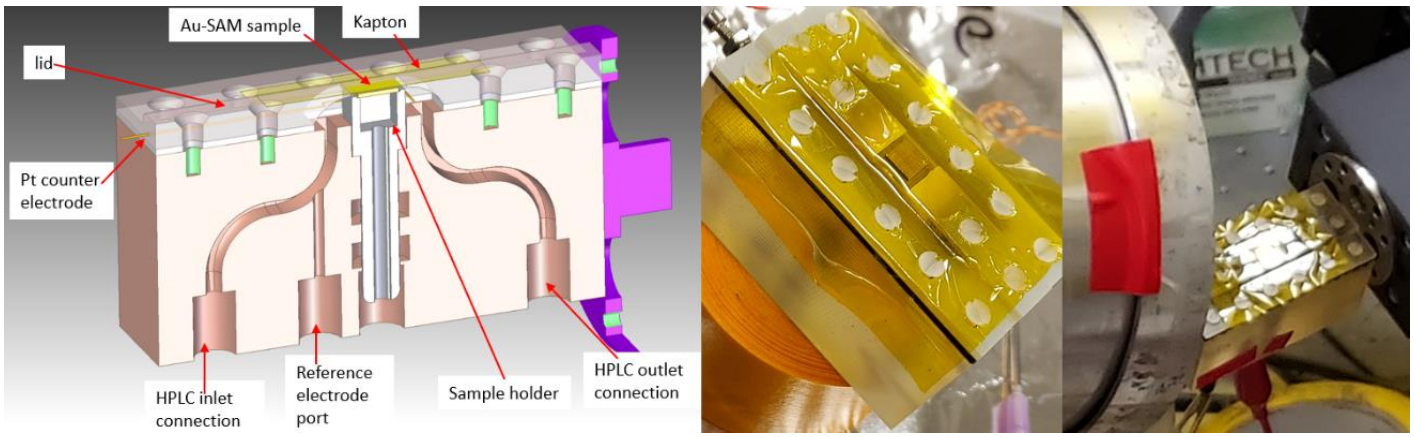

Figure 4-6 Left: Schematic of operando spectroelectrochemical cell for grazing incidence x-ray absorbance spectroscopy (courtesy of Ryan C. Davis of SLAC National Laboratory). Center: Photo of assembled with Au-SAM sample visible underneath the Kapton window of the lid. Right: Assembled cell on the goniometer with electrical leads (red alligator clips) at a 30º incident angle 11-2 beamline at SLAC. Germanium 100 element detector is adjacent to the cell (red tape).

4.3.4 X-ray Absorbance Spectroscopy

XAS experiments were conducted at the 11-2 beamline at the Stanford Synchrotron Radiation Lightsource (SSRL) at SLAC National Accelerator Laboratory. A 100 element Germanium detector positioned at an angle 90 degrees to the incident beam collected the energy resolved fluorescence signal. Grazing incidence angles were controlled with a Huber two-circle goniometer. The size of the wafer used for the XAS studies were 5x5 mm^2. The beam was focused vertically to 30 microns that was impinged on the wafer at glancing incidence of 0.15 degrees which probes ~1.3 nm of the surface. The Ge detector was gated around the Au L3 edge fluorescence. The EXAFS measurements were performed at different potentials after the electrode surface reached equilibrium.

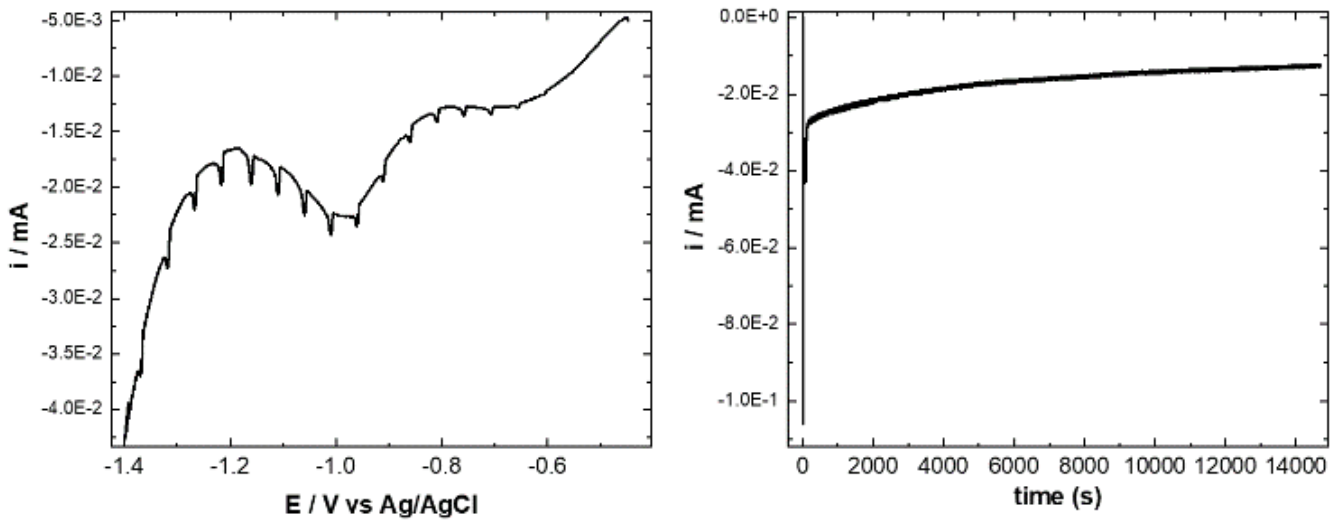

Figure 4-7 Left: Cyclic Voltammogram of Au-SAM (decanethiol) in grazing incidence XAS cell, 0.1 M potassium hydroxide, 20 mV/s, 3 mL/min flow rate. Right: Chronoamperometry of Au-SAM at -1.4 V for ~ 4 hours during XAS measurement.

4.4 Results and Discussion

4.4.1 Cyclic Voltammetry and Chronoamperometry

Figure 4-7 shows a reductive desorption cyclic voltammogram (CV) (left) and chronoamperometry (CA) (right) of a decanethiol SAM on Au coupon in 0.1 M potassium hydroxide in the grazing incident XAS flow cell with a 10 μm electrolyte layer above the Au surface, connected to the HPLC pump with a 3 mL/minute flow rate. Pulsing can be observed in the electrochemical data from the HPLC pump. The reductive desorption CV shows a distinct desorption peak at ~ -0.99 V vs AgCl before the onset of hydrogen evolution currents at -1.3 V, consistent with a typical Au-SAM reductive desorption experiment. The chronoamperogram (right) was taken at -1.3 V over the four hours during an XAS measurement of the surface, and is consistent with desorption CAs taken in a typical electrochemical cell. A spike from double-layer charging and the reduction of the SAM is observed with the first few seconds on top of larger hydrogen evolution currents which steadily decays over the four-hour measurement. These measurements demonstrate that the grazing incident spectroelectrochemical cell with a thin layer electrolyte operates as a typical electrochemical cell for measurement of SAM reductive stability.

4.4.2 Operando EXAFS Measurements

Preliminary EXAFS spectra of decanethiols SAMs on Au were taken with the x-ray beam at two incident angles; 30 and 0.15 degrees. EXAFS spectra were first collected without electrolyte in the cell, taken at 30 degrees to probe below the surface into the bulk Au structure which does not have Au-S bonds. After collecting the dry bulk Au spectra, the incident beam angle was set to

0.15 degrees and EXAFS data was collected to measure the Au-S bonds of Au-SAM surface in the dry cell without electrolyte. After the spectra of the surface in the dry cell was taken, hydroxide electrolyte was pumped in to the cell with continuous flow (3 mL/minute) and EXAFS spectra were taken at 0.15 degrees at open circuit potential (-0.23 vs AgCl), and then at -1.3 V, the potential where the SAM is reductively desorbed according to the cyclic voltammetry peak (fig). The reduced Au surface was allowed to equilibrate for 5 minutes before spectra collection began. Figure 4-5 shows the results of the grazing angle EXAFS. All of the collected spectra display the characteristic Au-Au twin peaks centered around 3 angstroms.[15-17] For the 30-degree spectra, only the Au-Au peaks are observed as expected due to most of signal is generated from the pure Au below the surface of the electrode. For the 0.15-degree spectra of the Au-SAM in the dry cell and with electrolyte at open circuit, a new peak is observed at 2.31 angstroms which has been identified as the Au-S peak in other works.[15-17] Spectra was then collected at -1.3 V at 0.15 degrees, and the Au-S peak is conspicuously absent, taken as evidence of cleavage of the Au-S bond, which should be reductively cleaved from the Au surface according to the hypothesis that potentials beyond the threshold potential (E_P) will cleave the Au-S bond. This data proves that a change in the chemical bonding environment of the Au surface as a function of potential is measurable for Au-SAMs in the grazing incident cell and represents the first time a Au-S SAM bond was measured directly during an electrochemical experiment using XAS.

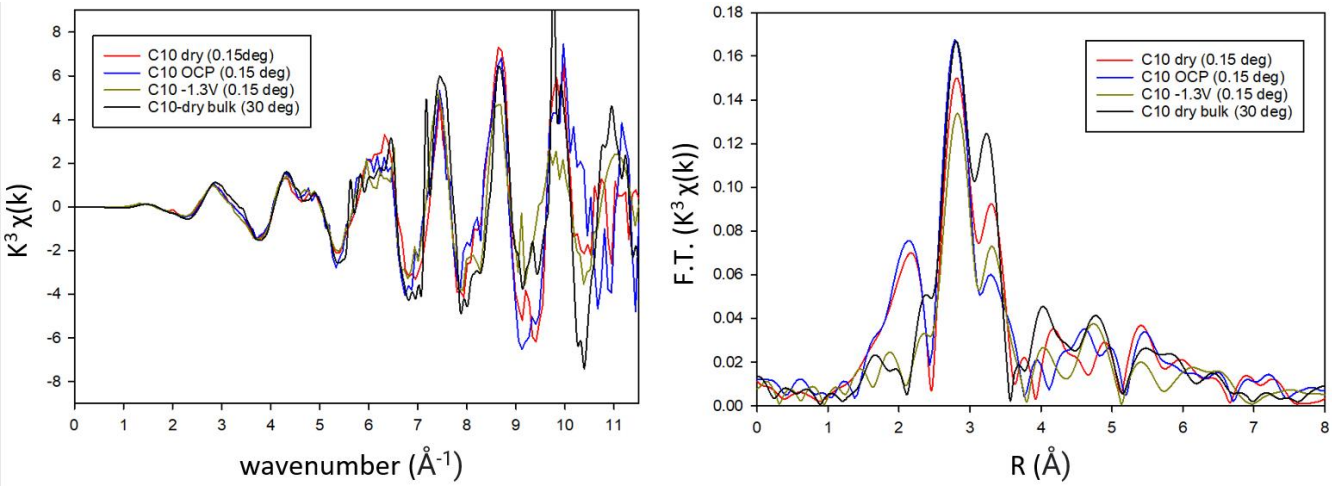

Figure 4-8 Left: EXAFS k space spectra of decanethiol Au-SAMs under various condition and incident angles. Right: Fourier-transformed EXAFS of data from the left showing Au-Au peaks ~ 3 angstroms and Au-S peaks at ~ 2 .3 angstroms.

More experiments were planned, such as taking spectra at various potentials leading up to -1 V to see if longer Au-S bond distances can be observed before the onset of desorption, which would represent filling of the adsorbate anti-bonding band in the d-band model hypothesis, but experiments were cut short by issues with the cell leaking and bubble formation within the cell internal chamber, which prevented the collection of quality spectra for those additional experiments in the short amount of time granted for the spectroscopy.

Adjustments have been made to the cell and more Au-SAM beamline experiments are being conducted at the SLAC beamline at the time of this writing, which hopefully will yield enough information to test the d-band model hypothesis, and pave the way for future measurements of SAM reductive stability on other metals such as Ni, Cu, Pd and Pt, which have proven difficult to assess SAM stability directly.

4.5 Conclusions

In this work, *operando* grazing incidence EXAFS of Au-S bonds of a decanethiol SAM was collected during the application of reductive potentials with a 10μm electrolyte thickness in spectroelectrochemical cell. Spectra of bulk Au below the SAM was taken at 30 degrees which only showed characteristic Au-Au peaks in the EXAFS. Spectra at grazing incidence (0.15 degrees) of the Au-SAM was taken at open circuit potentials in hydroxide solution which showed Au-S and Au-Au peaks. Grazing incidence EXAFS was then taken at -1.3 V, where only the Au-Au peak was observed, which implies that the Au-S bond was cleaved and the thiol was lost from the surface. Current work is underway to investigate the Au-S bond distances at more potentials to capture a change in the bond length as a function of potential, and future

measurements will focus on the potential dependent stability of adsorbates on other metals to test the extended d-band hypothesis as a predictor of metal dependent electrochemical stability.

4.6 References

(1) Widrig, C. A.; Chung, C.; Porter, M. D. "The electrochemical desorption of n-alkanethiol monolayers from polycrystalline Au and Ag electrodes," *Journal of electroanalytical chemistry and interfacial electrochemistry* **1991**, *310*, 335-359.
(2) Azzaroni, O.; Vela, M. E.; Fonticelli, M.; Benítez, G.; Carro, P.; Blum, B.; Salvarezza, R. C. "Electrodesorption Potentials of Self-Assembled Alkanethiolate Monolayers on Copper Electrodes. An Experimental and Theoretical Study," *The Journal of Physical Chemistry B* **2003**, *107*, 13446-13454.
(3) Bengió, S.; Fonticelli, M.; Benítez, G.; Creus, A. H.; Carro, P.; Ascolani, H.; Zampieri, G.; Blum, B.; Salvarezza, R. C. "Electrochemical self-assembly of alkanethiolate molecules on Ni (111) and polycrystalline Ni surfaces," *The Journal of Physical Chemistry B* **2005**, *109*, 23450-23460.
(4) Corthey, G.; Rubert, A. A.; Benitez, G. A.; Fonticelli, M. H.; Salvarezza, R. C. "Electrochemical and X-ray photoelectron spectroscopy characterization of alkanethiols adsorbed on palladium surfaces," *The Journal of Physical Chemistry C* **2009**, *113*, 6735-6742.
(5) Williams, J. A.; Gorman, C. B. "Alkanethiol Reductive Desorption from Self-Assembled Monolayers on Gold, Platinum, and Palladium Substrates," *The Journal of Physical Chemistry C* **2007**, *111*, 12804-12810.
(6) Floridia Addato, M. A.; Rubert, A.; Benítez, G.; Zelaya, E.; Cabello, G.; Cuesta, A.; Thomas, J. E.; Visintín, A.; Salvarezza, R. C.; Fonticelli, M. H. "Electrochemical Desorption of Thiolates and Sulfur from Nanoparticle and Planar Platinum Surfaces," *The Journal of Physical Chemistry C* **2013**, *117*, 7589-7597.
(7) Hammer, B.; Norskov, J. K. "Why gold is the noblest of all the metals," *Nature* **1995**, *376*, 238.
(8) Hammer, B.; Nørskov, J. "Theory of adsorption and surface reactions," In *Chemisorption and Reactivity on Supported Clusters and Thin Films*; Springer: 1997, p 285-351.
(9) Pettersson, L. G. M.; Nilsson, A. "A Molecular Perspective on the d-Band Model: Synergy Between Experiment and Theory," *Top. Catal.* **2014**, *57*, 2-13.
(10) Häkkinen, H. "The gold–sulfur interface at the nanoscale," *Nature Chemistry* **2012**, *4*, 443.
(11) Reimers, J. R.; Ford, M. J.; Halder, A.; Ulstrup, J.; Hush, N. S. "Gold surfaces and nanoparticles are protected by Au(0)–thiyl species and are destroyed when Au(I)–thiolates form," *Proc. Natl. Acad. Sci. U.S.A.* **2016**.
(12) Bard, A. J.; Faulkner, L. R.; Leddy, J.; Zoski, C. G. *Electrochemical methods: fundamentals and applications*; wiley New York, 1980; Vol. 2.
(13) Penner-Hahn, J. E. "X-ray absorption spectroscopy," *Comprehensive Coordination Chemistry II* **2003**, *2*, 159-186.
(14) Farmand, M.; Landers, A. T.; Lin, J. C.; Feaster, J. T.; Beeman, J. W.; Ye, Y.; Clark, E. L.; Higgins, D.; Yano, J.; Davis, R. C.; Mehta, A.; Jaramillo, T. F.; Hahn, C.; Drisdell, W. S. "Electrochemical flow cell enabling operando probing of electrocatalyst surfaces by X-ray spectroscopy and diffraction," *PCCP* **2019**, *21*, 5402-5408.

(15) López-Cartes, C.; Rojas, T. C.; Litrán, R.; Martínez-Martínez, D.; de la Fuente, J. M.; Penadés, S.; Fernández, A. "Gold Nanoparticles with Different Capping Systems: An Electronic and Structural XAS Analysis," *The Journal of Physical Chemistry B* **2005**, *109*, 8761-8766.
(16) Frenkel, A. I.; Nemzer, S.; Pister, I.; Soussan, L.; Harris, T.; Sun, Y.; Rafailovich, M. H. "Size-controlled synthesis and characterization of thiol-stabilized gold nanoparticles," *The Journal of Chemical Physics* **2005**, *123*, 184701.
(17) Shivhare, A.; Chevrier, D. M.; Purves, R. W.; Scott, R. W. J. "Following the Thermal Activation of Au25(SR)18 Clusters for Catalysis by X-ray Absorption Spectroscopy," *The Journal of Physical Chemistry C* **2013**, *117*, 20007-20016.

Chapter 5 Future Directions, Recommendations, and Unfinished Projects

5.1 Synthesis of Ethynyl-hydroquinone For Quinone Derivatization of Azide-terminated SAMs for Coverage Measurements on Cu, Ni after Applying Reductive Potentials

Chapter 2 and 3 grappled with the use of a tethered redox probe (Fc) to estimate the SAM coverage as a function of potential as a direct indicator of SAM reductive stability, which presented challenges with differentiating redox peaks from features that were correlated to those observed on bare Au surfaces observed experimentally and in the literature.[1,2] Using the same strategy on other bare metal surfaces such as Ni and Cu present their own unique challenges as scanning too positively during a CV will promote surface oxidation of the metal which could oxidatively desorb the surface attachment while trying to measure the coverage.

Using a hydroquinone functionalized redox-probe would be useful because the peaks are located at more negative potentials relative to ferrocene, and their peak position can be adjusted using the pH of the electrolyte solution. The hydroquinone peaks shift with the pH because the reduction or oxidation is accompanied by protonation or deportation of the hydroxyl groups on the molecule shown in figure 5-1.

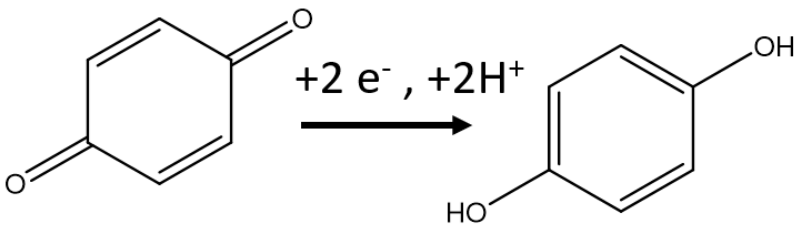

Figure 5-1 Hydroquinone reduction reaction.

Earlier work of hydroquinone tethered to alkanethiol SAMs show a Nernstian shift in the $E_{1/2}$ of the redox peaks, which was tentatively confirmed by rotation student Becca Dawley during her rotation in the McCrory lab. In figure 5-2, the peaks from commercial (Sigma) hydroquinone-undecanethiol deposited on Au exhibit pH dependent shift of the quinone redox peaks.[3]

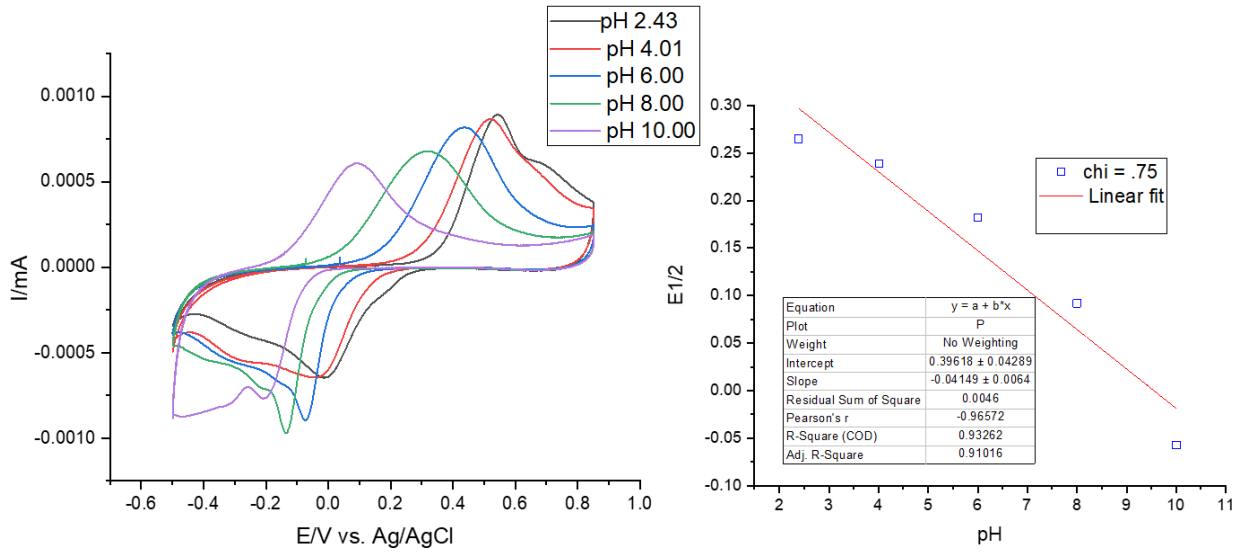

Figure 5-2 All work shown here credit to Becca Dawson Left:CVs of hydroquinone undecanethiol SAM on Au in Britton Robinson buffer at various pH. Right: pH dependence on the redox peak $E_{1/2}$.

Initial work showed non-ideal cathodic peaks, and deviation from ideal Nernstian behavior, but shows that the pH dependent strategy may provide some flexibility in the peak position which is beneficial in avoiding convoluting background peaks.

Attempts were made to synthesize (Sonogashira coupling) the ethynyl-hydroquinone for the Cu catalyzed Click reaction to the azido-undecanethiol SAMs, but are not yet successful.

5.2 Clicked Cu-phenanthroline SAMs on Au and Reductive Desorption

Alternatives to the ferrocene (Fc) capped SAMs were explored to avoid using Fc because of potential issues with high Fe backgrounds in the ICP-MS experiments used for secondary confirmation of SAM coverage after applied potentials.

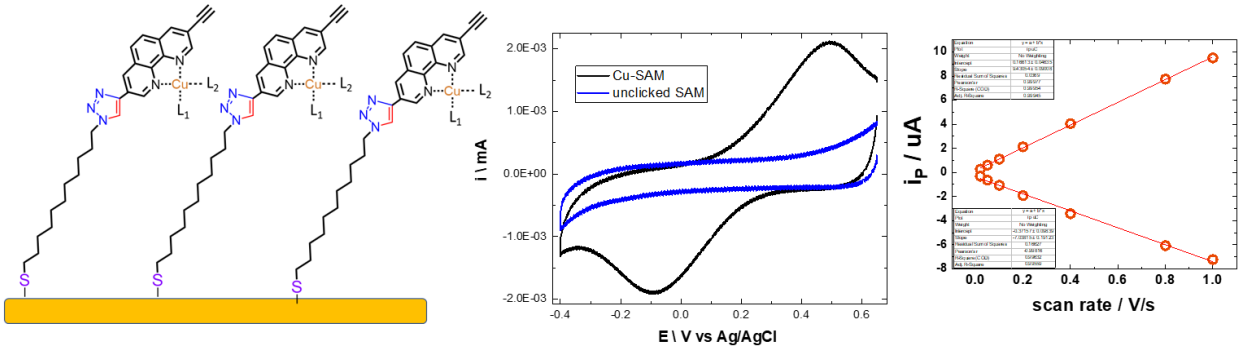

Figure 5-3 Left: Cartoon of Cu-phenanthroline tethered to undecanethiol SAM via triazole linkage. Center: Cu-phen SAM vs unclicked blank SAM CV in perchlorate/acetate buffer. Scan rate dependence on peak currents indicating the absence of diffusion in the CV measurement.

Cu-phenanthroline tethered to undecanethiol SAMs via a triazole linkage from the Click reaction was prepared for the secondary analysis experiments using ICP-MS. Credit for synthesis of the diethynyl phenanthroline molecule goes to Jeremy Kallick. Figure 5-3 left shows the proposed structure of the Cu-phen SAMs on a Au surface, center shows the CV response vs an unclicked blank SAM, and the right shows the CV scan rate dependence indicating that the redox peaks belong to a surface tethered species.[4]

Initial coverage dependence on χ was explored and found to produce coverage measurements much lower than the Fc-SAMs prepared the same way as shown in figure 5-4. The increase in the size of the redox molecule may be limiting coverage but its important to point out that no optimization studies of the Click reaction on this system were performed and higher coverages may still be possible with optimization.

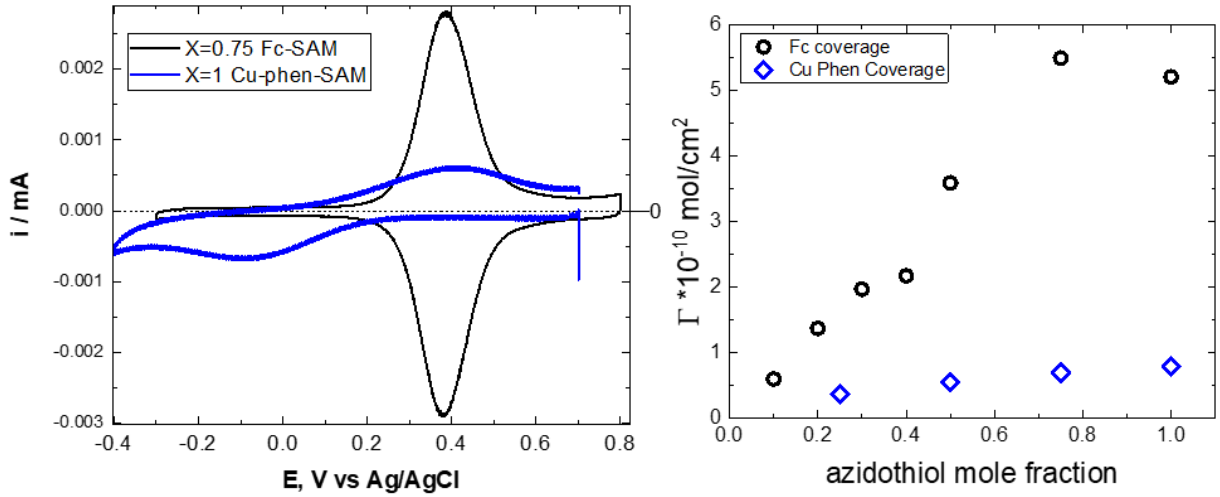

Figure 5-5 Left: Cu-phen SAMs CV compared to Fc-SAM CV. Right: Coverage dependence of clicked Fc-SAM vs Cu-phen SAMs.

The CV baselines (figure 5-5) after the application of reductive potentials indicated complexity which would convolute the peak area measurement, which would make this a good candidate system to test the LASSO regression models. Collection of more post-desorption CVs of the Cu-phen SAM and blank SAMs would be necessary to test the baseline correction model on this system.

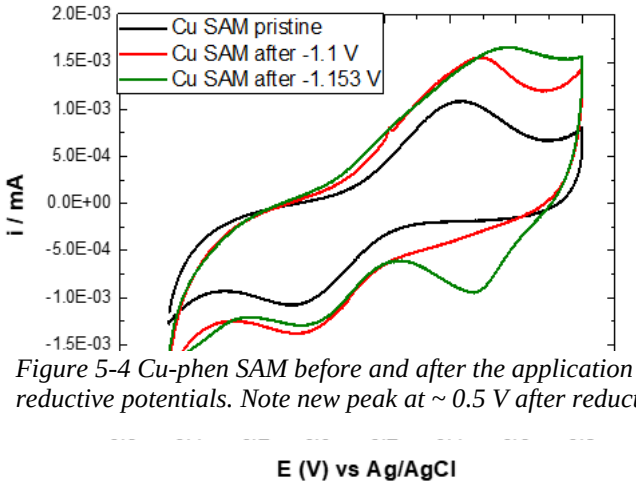

Figure 5-4 Cu-phen SAM before and after the application of reductive potentials. Note new peak at ~ 0.5 V after reduction.

5.3 Surface Limited Redox Replacement for Controlled Deposition of Cu Layers on Au Surface, Followed by SAM Deposition and Reductive Desorption Experiments

The original strategy for the *operando* x-ray absorbance spectroscopy of SAM metal surfaces during reductive desorption was to grow a thin metal Cu layer on top of a Au surface to avoid the complication of measuring bulk metal during spectroscopy. Growth of controlled Cu layers using an electrochemical technique called Surface Limited Redox Replacement (SLRR) was tested for future beamline experiments at SSRL. SLRR uses a Pb underpotential deposition (UPD) followed by redox replacement with Cu was pioneered by Dimitrov et al, and tested in the McCrory lab for the purpose of growing thin Cu layers on Au.[5-7]

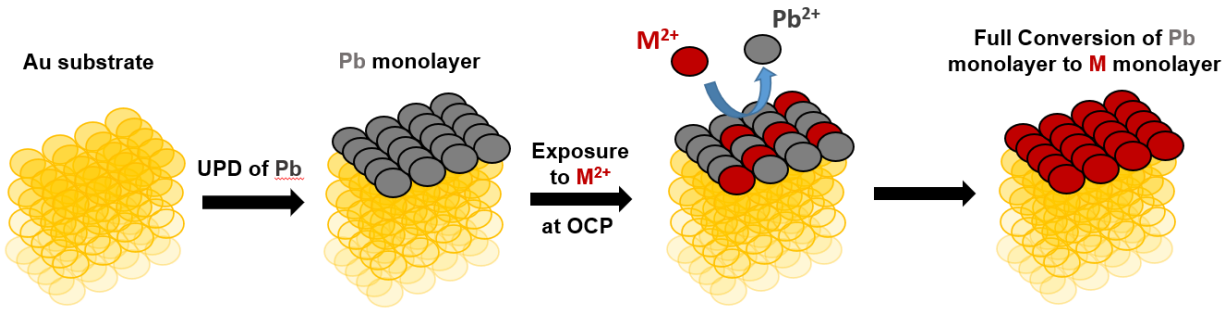

Figure 5-6 Cartoon of SLRR using Pb UPD followed by redox replacement of Pb with Cu to deposit a single Cu later or sub monolayer on a Au substrate.

In the SLRR experiments, a Au electrode in a Pb^{2+} solution with a concentration 1000 times greater than a Cu^{2+} present in the solution, is pulsed to -0.4 V vs AgCl, which is negative enough to deposit a Pb or a Cu UPD layer (figure 5-7), but Pb at much higher concentrations will outcompete Cu at the surface limited deposition sites on Au. Immediately after the Pb UPD pulse, the potential is relaxed to open circuit potential. Because of the Cu UPD potential occurs at potentials more positive than Pb UPD, the Cu will oxidize and exchange with and replace the

Pb on the surface. Pb UPD also occurs on Cu surfaces, which allows more pulses to sequentially build up Cu layers on the Au/Cu surface.

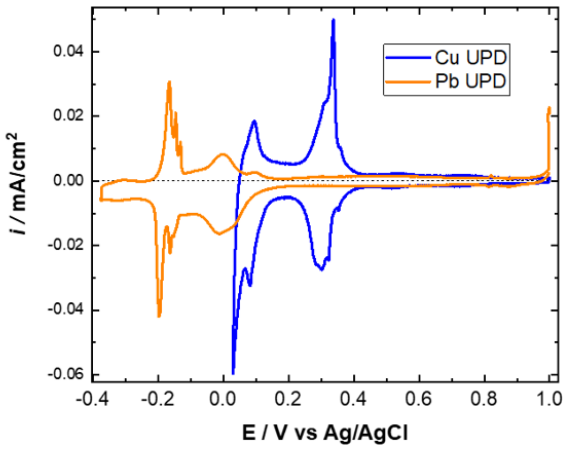

Figure 5-7 Cu and Pb UPD CVs taken on Au surface to compare the peak potential.

Figure 5-8 shows the potential measured during different stages of a pulsed SLRR multi-layer deposition of Cu. The experimental sequence went as follows: (1) Open circuit potential (OCP) was measured for consistency, (2) a 30s 1V potential was applied to clean the surface, (3) the potential was dropped to -0.375 V which in figure 5-7 corresponds to potential negative of the Pb UPD peak, (4) return to OCP to allow Cu to exchange with Pb at more positive potential (5) repeat for number of desired Cu layers. In figure 5-8, the experimental sequence was repeated with Pb only and then with Pb and Cu to observe the differences. With Pb only in the pulse sequence, the decay back to more positive potentials is slow and never reaches equilibrium before the next pulse, indicating a slow oxidation by low concentration oxygen molecules. In contrast, the decay to an equilibrium potential (indicated by a flattening of the potential versus time) in the Pb/Cu system is much more rapid because the Cu concentration facilitates oxidation of Pb much more quickly in the redox replacement events. Also, of note in figure 5-8 is that the OCP measurement in between pulses for the Pb + Cu sequence becomes more consistent at the potential that corresponds to a full Cu UPD layer (~ 0 V vs AgCl in figure 5-7), which is

evidence that the surface is becoming more Cu and the potential is fully pinned by the Cu/Cu^{2+} equilibrium.

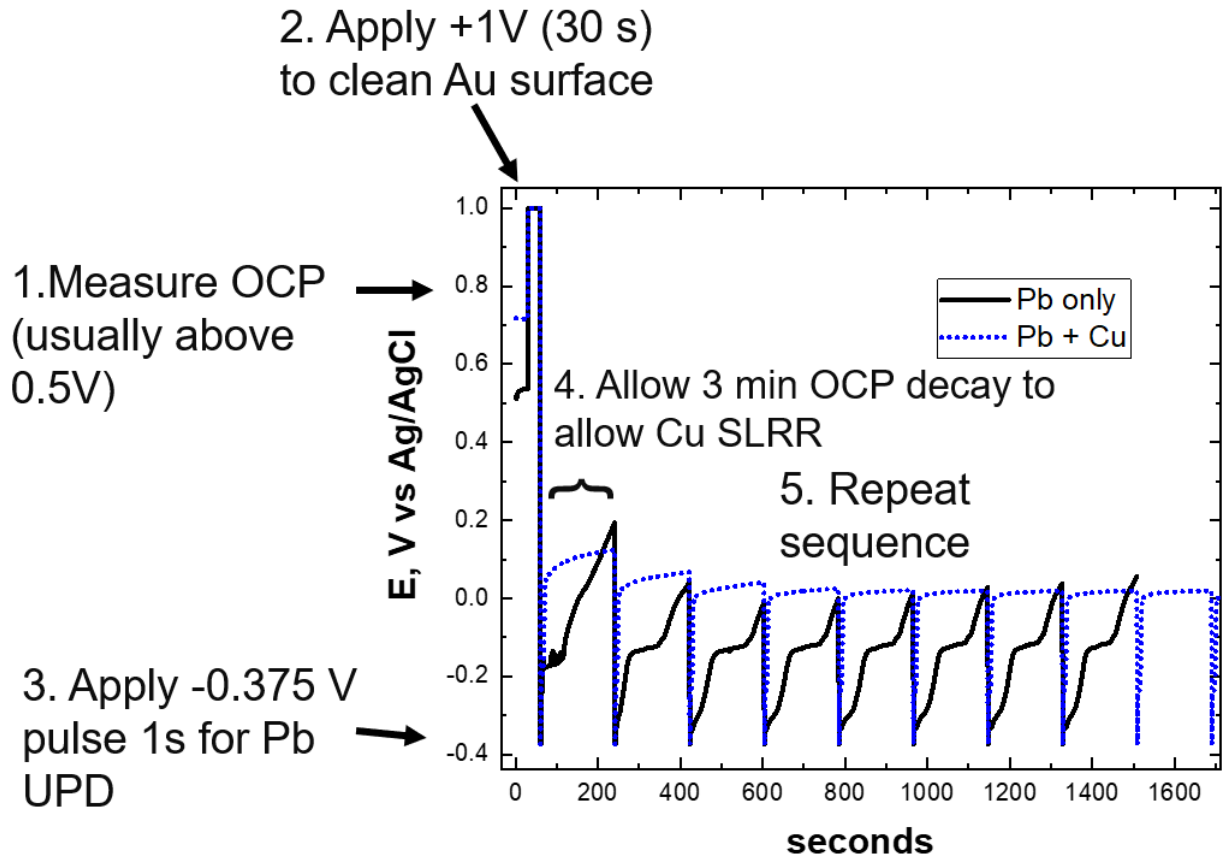

Figure 5-8 Experimental monitoring of potential during SLRR using Pb/Cu system. Blue dotted line are potentials observed for a typical SLRR process for the growth of Cu layers on Au. Black line is the same pulse sequence but with only Pb in solution.

Further experiments using azido-undecanethiol SAM deposition after different SLRR pulse sequences were measured using reductive desorption cyclic voltammetry to see if the desorption peaks for Au disappear as would be expected if the surface was covered in Cu. Figure 5-9 shows the results of the desorption CVs on the right which show that for increased SLRR pulses the reductive desorption peak disappears, as observed on bulk Cu electrodes. The presence of Cu and S was confirmed with XPS, and the azide vibrational modes of the SAM was detected using PM-IRRAS (not shown). (Figure 5-9 from NSF grant application.)[8]

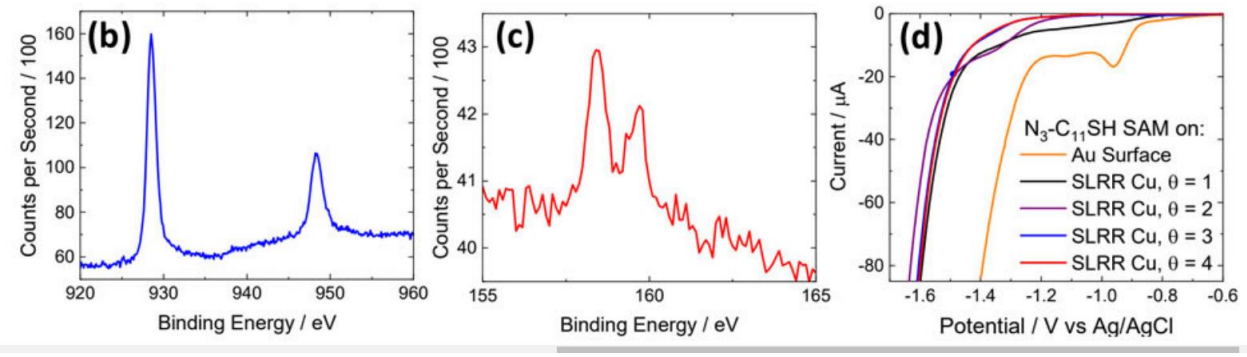

Figure 5-9 Left and Center: Cu and S XPS measurement of azide-SAM deposited on SLRR Au/Cu surface. Right: Redutive desorption linear sweep voltammograms showing desorption peak on Au surface, and attenuation of desorption peak or the disappearance of desorption peak with increasing SLRR pulsed to deposit Cu layers.

While the SLRR technique appear to be a workable strategy for depositing thin Cu layers between the Au and the SAM, ultimately the experiment failed during the beamline measurements for 2 major reasons: (1) the first beamline cell design could not properly control the electrolyte layer attenuating the x-ray signal, and (2) Cu XAS was initially detected briefly before the signal was lost permanently and never recovered, possibly due to oxidation of the Cu surface during shipping and set up time and dissolution into the electrolyte after the initial exposure to x-rays.

5.4 References

(1) Hamelin, A. "Cyclic voltammetry at gold single-crystal surfaces. Part 1. Behaviour at low-index faces," *J. Electroanal. Chem.* **1996**, *407*, 1-11.
(2) Hamelin, A.; Martins, A. M. "Cyclic voltammetry at gold single-crystal surfaces. Part 2. Behaviour of high-index faces," *J. Electroanal. Chem.* **1996**, *407*, 13-21.
(3) Hong, H.-G.; Park, W. "Electrochemical Characteristics of Hydroquinone-Terminated Self-Assembled Monolayers on Gold," *Langmuir* **2001**, *17*, 2485-2492.
(4) Bard, A. J.; Faulkner, L. R.; Leddy, J.; Zoski, C. G. *Electrochemical methods: fundamentals and applications*; wiley New York, 1980; Vol. 2.
(5) Dimitrov, N. "Recent Advances in the Growth of Metals, Alloys, and Multilayers by Surface Limited Redox Replacement (SLRR) Based Approaches," *Electrochim. Acta* **2016**, *209*, 599-622.
(6) Mitchell, C.; Fayette, M.; Dimitrov, N. "Homo- and hetero-epitaxial deposition of Au by surface limited redox replacement of Pb underpotentially deposited layer in one-cell configuration," *Electrochim. Acta* **2012**, *85*, 450-458.
(7) Vasilic, R.; Dimitrov, N. "Epitaxial growth by monolayer-restricted galvanic displacement," *Electrochem. Solid-State Lett.* **2005**, *8*, C173-C176.
(8) McCrory, C. C. L.; Penner-Hahn, J. E.; National Science Foundation: University of Michigan Ann Arbor, 2019; Vol. $598,994.